UNIVERSITY OF CALIFORNIA

Santa Barbara

Examining the Thermochemistry and Trace Element Geochemistry of Magma Mixing and Hybridization using Exploratory Modeling

A Thesis submitted in partial satisfaction of the

requirements for the degree Master of Science

in Geological Sciences

by

Jason S. Schmidt

Committee in charge:

Professor Frank Spera, Chair

Professor Matthew Jackson

Professor John Cottle

June 2015

The thesis of Jason S. Schmidt is approved.

_____

Matthew Jackson

_____

John Cottle

_____

Frank Spera, Committee Chair

June 2015

Examining the Thermochemistry and Trace Element Geochemistry of Magma Mixing and Hybridization using Exploratory Modeling

by

Jason S. Schmidt

Examining the Thermochemistry and Trace Element Geochemistry of Magma Mixing and Hybridization using Exploratory Modeling

Jason S. Schmidt

ABSTRACT

Magma mixing is a common petrogenetic process occurring in mid-oceanic ridge, oceanic island and island arc petrotectonic environments. An exploratory model was developed and used to investigate fundamental principles underlying magma hybridization. Unlike many geochemical models that satisfy mass balance only, the Toy model is a rigorous thermodynamic model which satisfies energy conservation as well as major, minor, trace and isotopic conservation expressions. *Magma hybridization* is defined as two or more disparate magmas, each in internal equilibrium, being mixed thoroughly enough to achieve thermodynamic equilibrium. The phase diagram used in this model is that of an isobaric binary eutectic system with no crystalline solution and zero enthalpy of mixing, similar to the model 'basalt' system $CaMgSi_2O_6$-$CaAl_2Si_2O_8$. There are three possible phases in this system that can coexist in different proportions: α crystals, β crystals or melt. The two components of the system are A and B with α phase pure component A and β phase pure component B. There are five possible phase assemblages in this system: L, α+L, β+L, L_e+α+β or α+β, where L denotes melt and L_e denotes eutectic melt. Eight thermodynamic parameters define the phase diagram including the melting temperature of each pure phase, distinct liquid and solid isobaric heat capacities, the enthalpy of fusion of pure α and β crystals and the eutectic temperature and eutectic composition. Five initial mixing conditions are required to define a magma hybridization outcome involving the mixing of two distinct magmas (**M** and **R**) to form a **Hybrid** magma (**H**): the initial temperatures and bulk compositions of resident

Magma (**M**) and **Recharge** magma (**R**) and the mass fraction (f_o) of **M** in the **M**+**R** mixture. The enthalpy of **H** magma is calculated based upon either an adiabatic or diabatic assumption. The model is also capable of simulating partial melting of a mixture of subsolidus sources through the addition of enthalpy to the subsolidus source. Once the thermodynamic calculations are completed and the phase assemblages pre- and post-hybridization are known, trace element and isotope mass balances are performed. Hence the result of any Recharge hybridization (R-hybridization) or Recharge Fractional Crystallization (RFC-hybridization) process gives complete thermodynamic characterization of the final state consonant with energy and mass conservation. Several applications are presented as examples. In several cases the Magma Chamber Simulator (Bohrson et al, 2013) is used to verify the applicability of the model. A Monte Carlo (MC) method is used to study the statistics of possible outcomes given a range of initial condition values. Statistical analysis of the MC realizations revealed that 44% of the outcomes were three-phase invariant point outcomes, illuminating a thermodynamic invariant point 'attractor' effect that may be relevant to crystallization (and partial melting) in the upper mantle and crust. Ten to twenty per cent of MC realizations exhibited a thermal anomaly such that the final temperature of hybridized magma was *less* than the initial temperature of both **M** and **R** magmas. This thermal anomaly phenomenon was verified using the Magma Chamber Simulator (MCS) and revealed a ~0.8 degree drop in **H** temperature for every percent increase in the crystal content of **M** magma when **R** magma is entirely molten. Investigation of the reaction of sub-solidus or mushy stoped blocks with **M** magma showed that when the mass of **M** is much greater than the mass of stoped blocks (common condition), the final temperature of **H** was more strongly dependent on the stoped block mineral mode than its temperature. Investigations

into phase change systematics revealed that cessation of precipitation of the saturation phase of **M** occurred even when the mixing ratio (mass ratio of **M** to **R**) was large. Extensive trace element experimentation was conducted. Results showed that serial isobaric FC-R-FC hybridization can produce trace element signatures consistent with clinopyroxene crystallization in an equilibrium basalt with only glass + plagioclase phenocrysts present, offering an alternative explanation of the 'pyroxene paradox' of MORB petrogenesis. Some results showed that despite significantly elevated concentrations of trace elements in an incoming **R** melt, **H** melt may exhibit essentially no enrichment outside the range of measurement. Further experimentation resulted in a 'Dilution Effect' where a trace element concentration in the melt phase of **H** was lower than in both initial magmas **M** and **R**. This occurs when the enthalpy of the mixed system is high enough that fusion of pre-existing crystals in **M** and/or **R** creates a sparsely phyric **H** magma. Results showed that under diabatic conditions the trace element concentrations in **H** melt could lie outside the range of values in **M** and **R** melts due to partitioning effects associated with fractional crystallization. Modeling trace element ratios during serial recharge showed that the bulk composition of each **H** fell on a mixing hyperbola defined by **M** and **R**, as expected, but that the melt phase of **H** did not necessarily define a hyperbola from which the original components **M** and **R** could be constrained unless the trace element ratios used to form the ratio-ratio coordinates had equal partition coefficients, always the case when isotope ratio - isotope ratio diagrams are considered. MCS R-hybridization simulation data analyzed in major oxide ratio-ratio space were used to explore the ramifications of fractional crystallization and subsequent crystal separation on two related hybrid magma **H**'s differing only in their **M** to **R** mixing ratio. The results confirm the issue set forth in the 'pyroxene paradox' of MORB

petrogenesis, where sparsely-phyric or aphyric basalts can contain glass that exhibits trace element trends indicative of specific phenocryst crystallization, even though that phenocryst is not present modally in the sampled lavas. Results from serial application of the binary eutectic model illustrate some possible physical and trace element and isotopic geochemical trends arising from the processes associated with a shallow crustal magma chamber undergoing magma mixing *via* recharge, fractional crystallization associated with heat loss to wallrock, assimilation of subsolidus hydrothermally altered mafic wallrock, and periodic eruption (RFCAE). The results show that the most incompatible elements are enriched in the melt of the RFCAE chamber even though the additions to the chamber (recharge and wallrock assimilation) were not particularly enriched relative to the initial magma. This result suggests a possible alternative process for producing enriched eruptive products (e.g., E-MORB) that does not invoke mixing of enriched subsolidus sources coupled to variable extents of partial melting of the mixed source and subsequent unmodified ascent and eruption. Although the Toy model is simple, it is not simplistic: it does provide insight into a variety of petrogenetic mechanisms.

TABLE OF CONTENTS

1. INTRODUCTION

1.1 Background and introduction to magma mixing

Current understanding of magmatic systems including mid-oceanic ridges (MORB), oceanic island hot spots, island arcs, active continental margins, and Large Igneous Provinces (oceanic and continental) indicates that the mixing of magmas and the mixing of magma sources on a variety of spatiotemporal scales is a first order petrogenetic process. In the magmatic context, Recharge, Assimilation and Fractional Crystallization (RAFC) represent the primary mechanisms whereby open system magma bodies undergo geochemical and thermal evolution. Magma mixing *via* the Recharge process is a pillar of the RAFC trinity deeply connected to many phenomena including (1) growth of continental and oceanic crust, (e.g., Marshall and Sparks, 1984; Perugini and Poli, 2012; Lee & Bachmann, 2014), (2) trigger mechanisms for explosive and effusive volcanic eruptions (e.g., Dvorak and Dzurisin, 1997; Eichelberger and Izbekov, 2000; Snyder, 2000; Fowler and Spera, 2008; Turner et al, 2008; Ferlito et al, 2012), (3) economic grade mineral deposits in layered intrusions (e.g., Maier et al, 2000; Kovalenko et al, 2009), and (4) the longevity of continental geothermal resources (e.g. Wolff and Ramos, 2013; Chamberlain et al, 2013).

The main focus of the research presented as my Master's thesis is to understand the process of magma mixing, specifically the end member magma mixing process termed magma hybridization. *Hybrid magma forms when two (or more) initially distinct magmas are brought together and attain thermodynamic equilibrium.* The thermodynamics of this process, including the connection between the thermochemistry, energetics and the behavior of trace elements, has long been used to monitor RAFC phenomena. It is hoped that this approach will provide fresh insight into the consequences of magma mixing, in the magma

hybridization limit. Although when magmas are brought together mixing may not be complete, it is nonetheless crucial to understand the limiting process of complete mixing---the process of *magma hybridization*.

It is worth noting that the term *magma*, as it is used throughout this thesis, refers to a heterogeneous suspension of crystals + silicate liquid ± supercritical fluid bubbles; that is, not simply a *liquid* or *melt* (liquid and melt are used synonymously). When two thermally and compositionally distinct magmas mix there are a variety of possible outcomes depending on the properties and amounts of the initial mixing 'components' and physiochemical conditions. Such details, quantified later, include the initial bulk composition (including major and trace elements and isotopic ratios), temperature, and phase proportions in each of the starting magmas as well as the relative proportions of the magmas being mixed (the mixing ratio) and, very importantly, the time available for mixing. *Magma* mixing is very different than *melt* (*liquid*) mixing. When two melts mix to form a single homogeneous (i.e., blended) melt, the temperature and composition of the resultant melt is simply the mass-weighted average of the temperature and composition of the mixing liquids. This case is trivial to calculate and not very important because superheated liquids are rare in nature (Carmichael et al, 1974). In contrast, the fluid dynamics of *magma* mixing is complex due to the influence of boundary and initial conditions and the relevant multi-level scales of heat, momentum and material transport. Steady state conditions are not necessarily always achieved. However, there are many cases reported where magma mixing *has* gone to completion or nearly so. In these cases, the machinery of equilibrium thermodynamics can be usefully applied. This is the limit of magma hybridization. As shown in this work, even within this thermodynamic limit, some unexpected outcomes can occur.

In general terms, magma mixing occurs across a binary spectrum: *hybridization* and *mingling*. *Magma mingling* produces a heterogeneous mixture containing discrete portions of the two magma types because blending remains incomplete or partial. In this case, the final product comprises spatially discrete portions of each magma (or lithic) type and is spatially heterogeneous with a spectrum of 'blob' sizes. Study of magma mingling focuses on the fluid dynamics and attendant transport processes at work during mixing, specifically the time and space correlations between the two mixing magmas (e.g., Sparks and Marshall, 1985; Oldenburg and Spera, 1989; Perugini et al, 2005). *Magma hybridization*, in contrast, is the end-member form of magma mixing where the dynamics have evolved via mixing a single hybridized magma.

Throughout this discussion I will use **M** to represent a resident **Magma** and **R** to represent a **Recharge** magma; these are the mixing 'components'. The final product, a **Hybrid** magma denoted **H**, is a multiphase mixture of homogeneous melt + crystals. Coexisting phases in **H** are in thermodynamic equilibrium. In physical terms, a hybrid magma is one in which the mean blob size has been reduced, roughly, to less than a diffusive scale length $\delta \approx \sqrt{Dt}$ where t is the duration of contact. Based on a tracer diffusivity of oxygen in a silicate melt of 10^{-12} m^2/s at 1500 K (Spera et al, 2011), diffusive boundary layer thicknesses are 0.8 mm, 1.6 mm, 5.6 mm, 1.8 cm, 5.6 cm, and 0.18 m for durations of a week, month, year, decade, century, and millennium, respectively. Where a given magma mixing scenario falls within the mingling-hybridization spectrum depends on many factors including magma thermodynamic and transport properties, boundary and initial conditions, the geometry of magma interaction and the duration of mixing before thermal arrest by solidification *via* the viscosity 'catastrophe' (e.g., Spera, 2000; Slezin, 2003).

There are two thermal limits that can occur when magmas **M** and **R** mix and hybridize. The simplest case is the adiabatic case, where no loss of heat to subsolidus country rock occurs during the hybridization process. In other words, the specific enthalpy of the hybrid magma (**H**) is the mass weighted sum of the initial enthalpies of **M** and **R** (see next section and APPENDIX I for details). In this case **H** is the result of the intrusion and intimate mixing and equilibration of recharge magma with resident magma, and it is termed *R-hybridization*. If, however, significant enthalpy is lost from the magma system to its surroundings, the final enthalpy of **H** will be less than the initial combined **M**+**R** enthalpy. Hybridization associated with such a loss of thermal energy is a diabatic or diathermal process and produces additional precipitation of crystals, above and beyond what occurs strictly due to adiabatic mixing. So in the diabatic case $h^H < (h^M+h^R)$ (see Table A1-1 for nomenclature), both recharge and fractional crystallization occur, resulting in what is termed *RFC-hybridization*. An additional level of complexity occurs when a magma body emplaced within country rock is either hot enough or long lived enough, or both, to partially melt some of the surrounding rocks. If the chemical and fluid dynamics are such that partial melts (anatectic melts) of country rock are incorporated into the magma body, then assimilation is said to occur. In the most complex cases of magma chamber evolution it is possible to have all of these processes – recharge, assimilation and fractional crystallization – occurring concurrently, each contributing towards the creation of hybrid magma. Such a process is termed *RAFC-hybridization* provided sufficient mixing has reduced the scale of chemical heterogeneity to the diffusive scale length or smaller.

1.2 Modelling approaches

To foster a solid foundation upon which to base interpretations and hypotheses, quantitative models, along with experiments and observations, have an important role to play. The model developed as part of this thesis, colloquially referred to as a 'toy' model, is an equilibrium thermodynamic model based upon an isobaric binary eutectic system with ideal mixing of liquids and no solid solution (Figure 1). Because the toy implements equilibrium thermodynamics, a realization generated by the model is, by definition, a *hybrid magma*. While more realistic multicomponent-multiphase models exist to model RAFC phenomena (e.g., Bohrson, et al, 2013), the complexity of such models can obfuscate the interdependent nature of the underlying thermodynamics and geochemistry. Contrastingly, the thermodynamics and trace element geochemistry of the toy model are transparent and hence the sensitivity of hybridization outcome on the composition, phase state, trace element distributions, temperature and mixing proportions of the mixing magmas (**M** and **R**) is easy to grasp. I have shown in previous work with collaborators (e.g., Spera et al, 2015) that phenomena first identified by toy model realizations can, in fact, be observed in the multiphase-multicomponent treatment of Bohrson et al (2013).

Because of ever increasing computing power it is now possible to create computer models to replicate (to the best of our physical and mathematical understanding) complex natural systems. The Magma Chamber Simulator of Bohrson et al (2013) which models RAFC processes, is one example, as is the pMELTS model of Ghiroso et al (2002). While such detailed modelling is useful, particularly in understanding and/or replicating very specific scenarios, it has been recognized by researchers in multiple disciplines that such

levels of complexity may fail to illuminate underlying fundamental principles (e.g., Larsen et al, 2014). This can be counter-productive if the scientific goal is to understand general causality. The toy model seeks to augment the understanding gleaned from more complex models by taking a minimalist approach. The choice of an isobaric binary eutectic system as a basis for modelling the thermodynamic equilibrium end-member of magma mixing reduces a highly complex problem down to its simplest possible terms by stripping away extraneous features. The simplicity of the toy model enables rapid development of an intuitive understanding of the basic principles underlying magma hybridization in natural systems. The fundamental nature of the insights gleaned from the toy are hypothesized to be of general applicability adaptable to any natural magma system, and thus are expected to be relevant to a wide variety of petrotectonic problems. One of the principal goals of this study is to test this hypothesis.

2. TOY MODEL DESCRIPTION

2.1 Major element thermochemistry

Following is an overview of the specifics underlying construction of a toy model realization. Table A1-1 summarizes all variable definitions used. More detailed information including the specific enthalpy equations and thermodynamic parameter values used for this study are provided in APPENDIX I.

The phase diagram of the model (Figure 1) is that of an isobaric binary eutectic system with no crystalline solution and zero enthalpy of mixing, not unlike the classic 'basalt' system $CaMgSi_2O_6$ - $CaAl_2Si_2O_8$ (Bowen, 1928). There are three possible phases in this system that can coexist in different proportions: crystals of phase α, crystals of phase β or

melt. The two components of the system are A and B with α phase pure component A and β phase pure component B. In terms of this model 'basalt' system, X is the mass fraction of B component (i.e., the mass fraction of $CaAl_2Si_2O_8$). Eight thermodynamic parameters define the topology of the system: the eutectic composition, X_e, where X is the mass fraction of component B, the eutectic temperature, T_e, the melting temperature of pure α and β crystals ($T^{\alpha}_{m.p.}$ and $T^{\beta}_{m.p.}$), the specific (per unit mass) enthalpy of fusion of α and β (Δh^{α} and Δh^{β}), and the isobaric specific heats of α and β (approximated as identical and denoted C_S) and of melt, C_L. In what follows, these eight parameters have been chosen to model the $CaMgSi_2O_6$ - $CaAl_2Si_2O_8$ 'basalt' system, although by changing thermodynamic parameter values systems with different thermodynamic properties and phase relations can be modeled.

In order to define a magma hybridization outcome involving the mixing of two distinct magmas **M** and **R**, each in internal equilibrium, to form hybrid magma **H**, five initial mixing conditions are needed. These include the initial temperatures $\left(T^M_o, T^R_o\right)$ and bulk compositions $\left(X^M_o, X^R_o\right)$ of **M** and **R** and the mass fraction of **M** magma (f_o) in the **M**+**R** mixture. Because the process of magma mixing is modeled as closed with respect to mass exchange with the environment, the final bulk composition (X^H) of hybrid magma **H** is known once X^M_o and X^R_o are specified. The model allows the enthalpy of hybridized magma to be calculated based upon either an adiabatic ($h^H = h^M + h^R$) or diabatic [$h^H = \Phi(h^M + h^R)$] assumption, where h^H is the specific enthalpy of the hybrid magma **H**, h^M is the specific enthalpy of the resident magma **M**, h^R is the specific enthalpy of the recharge magma **R** and Φ, the diabatic parameter, represents the fraction of total initial combined enthalpy retained after hybridization and subsequent heat dissipation ($0 < \Phi < 1$). Thus, adiabatic hybridization, also known as *R-hybridization*, pertains when $\Phi = 1$. In contrast, if in addition to the physical

mixing and hybridization of **M** and **R** heat transfer from magma to subsolidus country rock occurs, the hybridized magma **H** has an enthalpy that is fraction Φ of the initial combined **M**+**R** enthalpy and the process is termed diabatic, or *RFC-hybridization*, because in addition to recharge mixing, fractional crystallization occurs due to heat extraction. In either R- or RFC-hybridization, the temperature, bulk composition and phase assemblage (proportions and composition of all stable coexisting phases) of hybridized magma **H** are computed. Note that because mass exchange between the magma chamber and the environment is not allowed in the model (other than addition of recharge) it does not directly address the energetics of country rock partial melting. It does, however, illuminate some aspects of assimilation such as stoping blocks (see section 4.3). A schematic example of initial and final states is depicted in Figure 2. Partial melting can also be studied using the toy model by setting $\Phi > 1$ and T_o^M and T_o^R less than T_e.

There are five possible phase assemblages in this system: L, α+L, β+L, L_e+α+β or the crystalline assemblage α+β, where L_e denotes melt of eutectic composition ($X_\ell = X_e$). The phase diagram and thermochemistry are defined by specification of the system's previously discussed thermodynamic property variables X_e, T_e, Δh^α, Δh^β, $T^\alpha_{m.p.}$, $T^\beta_{m.p.}$, C_S and C_L. The liquidii of the toy model are linearized in T-X space. This approximation makes little difference to any of the basic insights gained by study of the toy model regarding magma hybridization. The characteristic concave-down shape of liquidii could be captured using fusion entropies and calculating the entropy, volume and enthalpy of mixing (i.e., non-ideality) as in a standard liquidus curve calculation, however the algebra becomes more cumbersome and nothing new is gained conceptually. Hence the two branches of the liquidii in T-X space are linearized such that for $X < X_e$,

$$T_{liquidus} = \left(\frac{T_e - T^{\alpha}_{m.p.}}{X_e} \right) X + T^{\alpha}_{m.p.} \qquad (1)$$

whereas for $X > X_e$,

$$T_{liquidus} = \left(\frac{T_e - T^{\beta}_{m.p.}}{Y} \right) Y + T^{\beta}_{m.p.} \qquad (2)$$

Given bulk compositions and initial temperatures for **M** and **R**, phase assemblages in each can be determined from the phase diagram using the lever rule and liquidii T-X relations. Once the phase assemblage and liquid compositions (if applicable) for **M** and **R** are known the specific enthalpy of each can be computed and, by appropriate weighting, the specific enthalpy of the mixture (**H**) can be determined. If one wants to model R-hybridization they must use $\Phi = 1$. RFC-hybridization utilizes $0 < \Phi < 1$, where the balance of thermal energy $(1 - \Phi)$ has been dissipated *via* conduction into surrounding subsolidus country rock. The starting phase assemblage of **M** and **R** depend on their bulk composition and initial temperature and hence expressions for the specific enthalpy must take into account phase state and proportions. The relevant expressions are collected in Table A1-3, which give the contributions that **M** and **R** make to the specific enthalpy of the mixture.

2.2 Enthalpy calculation example

As an example, consider R-hybridization of an initial **M** magma of bulk composition $X^M_o < X_e$ that is just at its liquidus (~100% melt + trace α crystals) and an **R** magma of composition $X^R_o > X_e$ that lies at a temperature between the β-saturated liquidus and the eutectic temperature T_e. In this case, **R** is a two-phase assemblage of β + L whereas **M** is essentially a crystal-free liquid denoted by the subscript Lα in Table A1-3. In this case, the

initial specific enthalpy of the hybrid magma **H** is given by $h_o^H = h_{L\alpha}^M + h_{\beta+L}^R$ which from Table A1-3 is explicitly expressed as:

$$h_o^H = f_o\left[C_s T_o^M + \Delta h^\alpha + X_o^M\left(\Delta h^\beta - \Delta h^\alpha\right) + \Delta C\left(X_o^M\left(T_{m.p.}^\alpha - T_{m.p.}^\beta\right)\right) + \left(T_o^M - T_{m.p.}^\alpha\right)\right]$$

$$+(1-f_o)\left[C_s T_o^R + \left(\frac{Y_o^R}{Y_o^{R\ell}}\right)\Delta h^\beta + Y_o^R\left(\Delta h^\alpha - \Delta h^\beta\right) + \Delta C\left(Y_o^R\left(T_{m.p.}^\beta - T_{m.p.}^\alpha\right) + \left(\frac{Y_o^R}{Y_o^{R\ell}}\right)\left(T_o^R - T_{m.p.}^\beta\right)\right)\right] \quad (3)$$

The resulting enthalpy value for **H** obtained from Equation (3), in conjunction with the new bulk composition X^H, is compared against the ranges given in Table A1-4 to discover which of the five possible phase assemblage outcomes is relevant. The final phase assemblage of hybrid magma **H** is then calculated according to the expressions of Table A1-5, A1-6 or A1-7, as appropriate (see detailed discussion in APPENDIX I). It is worth noting here that even in the "simplified" case of a toy model magma mixing scenario the calculations required are non-trivial, as examination of Equation (3) reveals. Any combination of states of **M** and **R** can be constructed using appropriate pairs from Table A1-3. The composition of the melt along the liquidus in Equation (3) is found from Equation (2) by setting $T_{liquidus}$ equal to T_o^R and solving for $Y_o^{R\ell}$, the composition of melt along the β-saturated liquidus.

Because the toy model calculates equilibrium phase assemblages, it is an ideal platform for the calculation of trace element and isotope mass balances. Once the thermodynamic calculations are completed and the phase assemblages pre- and post-hybridization are known, trace element mass balance calculations can be performed to determine the concentration of trace elements in each coexisting phase. The trace element derivation is outlined in the following section.

3. TRACE ELEMENTS AND ISOTOPES IN THE TOY MODEL

3.1 Background

The toy model is capable of incorporating an arbitrary number of trace elements and isotope ratios once the trace element bulk composition of **M** and **R** are specified and partition coefficients (assumed constant) for each trace element in phase α and β are defined. Significantly, as shown below, magma recharge can give a unique, sometimes surprising, signature to hybridized melts. The coupling between phase equilibria and trace element abundances is a natural consequence of the energetics of magma hybridization.

The trace element modelling works by first distributing a trace element between coexisting phases in **M** and **R** using partition coefficients treated as constants and the bulk concentrations in **M** and **R** magmas. It is possible to allow the partition coefficient (K) to vary with temperature (T) and composition (X) but this is not implemented here because our interests are more in general relations and not in modeling any specific system. Following initialization of **M** and **R**, the hybrid **H** magma state is computed self-consistently using thermodynamics to obtain the temperature and phase assemblage details of **H** magma. Since the toy model system is closed (no exchange of mass with surroundings, although heat exchange is permitted) the trace element bulk composition of **H** is the mass weighted average of the trace element bulk compositions of **M**+**R**. After the phase state of **H** is computed based upon the thermodynamics (as outlined above), the trace element is distributed amongst the coexisting phases in **H** using equilibrium crystal partitioning (e.g., Spera et al, 2007). Because isotopes are not fractionated in the toy model, the isotopic mass balance is

straightforward; the isotope ratio in **H** is simply the concentration-averaged sum of ratios in **M** and **R** (see below).

3.2 Trace element concentrations and isotope ratios in M, R and H magmas

A simple trace element material balance is used to compute the concentration of a trace element in **M, R** and **H** melts and coexisting crystals. Concentrations depend on phase identities, abundances and the crystal/melt Nernst partition coefficients, which are treated as constants. Expressions for the concentration of a trace element in the melts and crystals of **M**, **R** and **H** are given explicitly in APPENDIX II. All variables used are defined in Table A1-1. The expressions in Table A2-1 are written for a single trace element; any number of trace elements can be simultaneously computed by simply using the appropriate partition coefficient defined for the i^{th} trace element as $K_{s\ell,\,i} = \frac{C_{s,\,i}}{C_{\ell,\,i}}$ where s represents solid crystal phase α or β. The subscript i, denoting a particular trace element, is dropped in Table A2-1 for the sake of brevity.

Prior to mixing, each starting magma **M** and **R** is in one of four possible phase assemblage states: L, L + α (if X_o^M or $X_o^R < X_e$), L+ β (if X_o^M or $X_o^R > X_e$) or all solid (α + β). The model does not permit **M** or **R** to be exactly eutectic composition although when mixed the final **H** magma can be any composition in the range $0 < X^H < 1$ including the eutectic composition. The model does not lose any generality since both X_o^M and X_o^R can be arbitrarily close to X_e. The outcome of hybridization gives rise to the hybrid **H** magma in one of five possible assemblage states: L, L + α (if $X^H < X_e$), L + β (if $X^H > X_e$), the unique invariant point assemblage L_e+ α +β, or the sub-solidus assemblage α +β.

Once the phase assemblages and proportions are calculated, trace element mass balances are determined using the partition coefficient (as defined above), the initial bulk concentration of the element in **M** and **R** and the magma mixing ratio defined by f_o. Trace element concentrations are calculated and assigned to all existing phases, for all three magmas (**M**, **R** and **H**), so that one can readily observe partitioning behavior prior-and-subsequent-to mixing.

Isotope ratios are easy to handle. Since no isotopic fractionation is allowed, all phases in **M**, **R** or **H** magma possess the same isotope ratio. For example, if **M** is initially a mixture of melt + α then the bulk isotopic ratio of, for example, Sr in **M**, defined as $r^M_{Sr} = \frac{C^M_{87_{Sr}}}{C^M_{86_{Sr}}}$, gives identical values in melt, $r^M_{Sr,\ell} = \frac{C^M_{87_{Sr}}}{C^M_{86_{Sr}}}$ and coexisting α crystals, $r^M_{Sr,\,\alpha} = \frac{C^M_{87_{Sr}}}{C^M_{86_{Sr}}}$. When **M** and **R** are hybridized to form **H** magma, the isotopic ratio in melt and coexisting crystals in **H** is identical to the bulk isotopic ratio of **H** magma; $r^H_{Sr} = \frac{C^H_{87_{Sr}}}{C^H_{86_{Sr}}}$. A simple mass balance determines the isotopic ratio in **H** magma and depends on the fraction of **M** magma in the mixture, the bulk concentration of the trace element in both **M** and **R** and the isotopic ratio in both **M** and **R**. The expression, illustrated again here explicitly for Sr but easily generalized to any isotopic ratio is:

$$r^H_{Sr} = \frac{f\left(C^M_{Sr} r^M_{Sr}\right) + (1-f)\left(C^R_{Sr} r^R_{Sr}\right)}{f C^M_{Sr} + (1-f) C^R_{Sr}} \qquad (4)$$

To continue the example from section 2.2, trace element concentrations in all coexisting phases in **M** and **R** prior to hybridization would be calculated by employing the

expressions found in Table A2-1, where **M** is all melt (L) and **R** is L+β. While a trace amount of α crystals may be present in **M** there are not enough present to substantially fractionate a trace element *via* a partition coefficient, thus the concentration of any trace element in the melt of **M** *must be* the bulk concentration of that element in **M**, or symbolically $C_i^{M\ell} = C_{i_o}^{M}$. Contrastingly, in this example, **R** is a mixture of melt and β crystals, so the partition coefficient of a given trace element in β, in conjunction with the relative proportions of melt and β crystals in **R** (a function of enthalpy) must be taken into account. This requires two calculations; one to determine the concentration of the trace element i in the melt phase of **R** ($C_i^{R\ell}$), and a second using this calculated $C_i^{R\ell}$ to determine the concentration of the trace element in coexisting β crystals of **R**:

$$C_l^R = \frac{C_o^R}{\left(w_\beta^R\left(K_i^{\beta\ell} - 1\right) + 1\right)} \tag{5a}$$

$$C_\beta^R = C_l^R K_i^{\beta\ell} \tag{5b}$$

where C's represent concentrations of a trace element, w represents a mass fraction (in this case of β crystals) and K represents a partition coefficient (see Table A1-1 for explicit definitions). For reference and use in a later section, note that the trace element ratio for two elements (say Sr and Eu) is easily found by applying Equation (5a):

$$\frac{C_{Sr}^{R\ell}}{C_{Eu}^{R\ell}} = \frac{C_{Sr_o}^{R\ell}}{C_{Eu_o}^{R\ell}} \frac{\left(w_\beta^R\left(K_{Eu}^{\beta\ell} - 1\right) + 1\right)}{\left(w_\beta^R\left(K_{Sr}^{\beta\ell} - 1\right) + 1\right)} \tag{6}$$

From Equation (6) it is noted that when the partition coefficients are identical, then the concentration ratio on the left hand side of Equation (6) is equal to the bulk concentration

ratio, the first term on the right hand side of Equation (6). However, if the partition coefficients are not equal, and in general they are not, then the ratio depends explicitly on the mass fraction of the solid phase, in this case w_b because **R** magma is saturated in β phase, as well as the (unequal) values of the partition coefficients of the two distinct elements used to form the ratio.

The trace element concentrations for any combination of coexisting phases permitted in the toy model can be calculated using the expressions in Table A2-1. Once the final phase assemblage has been determined in hybrid magma **H** following the procedure outlined in section 2.2 above (see APPENDIX I for more detail), the trace element concentrations in any coexisting phases in **H** are determined analogously to those outlined for **M** and **R** using the expressions collected in Table A2-1. Isotope ratios in **H** are found using Equation (4) defined above.

3.3 Summary and implications of the toy model

In summary, the toy model couples energetics to phase, trace element and isotope ratio mass balance self-consistently. There are many issues that can be addressed using the toy as an exploratory model. For example, if a particular trace element is incompatible in phase α but compatible in phase β, or *vice versa*, how do concentrations change in melts prior to and after hybridization? Is it possible to mix melt from **M** and melt from **R**, and form a hybrid **H** melt with a trace element concentration *not in the range* of either **M** or **R** given reasonable bulk compositions and partition coefficients? When **M** and **R** have hybridized can the temperature of **H** be less than either the **M** or **R** initial temperatures? How can the systematics of mixing hyperbolas (e.g., Steiger and Wasserburg, 1966; Vollmer, 1976;

Langmuir et al, 1978) be applied to the mixing of magmas (bulk compositions), subsolidus sources and multiphase equilibrium mixtures? What are the effects of varying thermodynamic parameters such as fusion enthalpies and heat capacities on hybridization outcomes? How does the relative amount of crystallinity of an initial magma affect hybridization outcome? These and other questions can be pursued using the toy model. A complete solution to a toy hybridization scenario is virtually instantaneous, taking a few seconds (at most) of computer time. Hence many solutions can be obtained in a matter of hours and many variables can be efficiently studied. In contrast, the Magma Chamber Simulator (MCS) model of Bohrson et al (2013) or the pMELTS model of Ghiroso et al (2002) can require 20 to 30 minutes of uninterrupted computing time for a single solution, sometimes without successful completion and always with a tyranny of numbers that can obfuscate simple interpretations.

4. APPLICATIONS

A basic proposition of this thesis is that the toy model used to investigate the multifaceted landscape of magma evolution in open systems characterized by magma mixing (recharge), fractional crystallization (FC) and assimilation of stoped blocks of wallrock (A) is relevant to natural systems. Open system magma evolution behavior is the norm not the exception. Therefore we can expect the model to illuminate significant petrogenetic questions. In the remainder of this study, several applications are considered. These applications are not exhaustive but rather a thought provoking introduction to the potential of the toy as an exploratory model.

4.1 Monte Carlo analysis of preferred states

One of the first questions I sought to answer with the toy model was: given a fixed set of thermodynamic properties, what is the probability distribution of **H** magma phase assemblage outcomes given a reasonable span for each of the five initial condition (IC) parameters X_o^M, X_o^R, T_o^M, T_o^R, and f_o? In other words, are any of the possible phase assemblages of H magma more probable than any others? An efficient approach is to apply a Monte Carlo (MC) method to study the statistics of the five possible outcomes (as outlined previously in section 2.1) given a realistic range of possible values for each of the five IC parameters. The thermodynamic properties were held fixed using values representing the classic 'basalt' system $CaMgSi_2O_6$ - $CaAl_2Si_2O_8$. The IC value ranges chosen for the Monte Carlo approach are given in Table A1-2. Note that by choosing a temperature range, an enthalpy range was implicitly defined. This implicitly defined enthalpy range, termed "global", marks the maximum and minimum enthalpy (H_{Gmax}, H_{Gmin}) for a given set of IC parameter values (see Figure 3). Over 5 million Monte Carlo realizations were generated by application of the toy model using the values outlined above and in Table A1-2. Statistical analyses (binning) of the MC realizations yielded the following outcomes: L = 6.5%, L+α = 8%, L+β = 18.5%, L_e+α+β = 44%, and α+β = 23%. A disproportionate fraction (44%) of the outcomes were three-phase invariant point outcomes in which eutectic liquid (L_e) stably coexists with α and β crystals (Figure 4). This was a striking and, initially, unexpected result. An example is presented in Figure 4. **M** magma (87% melt + 12% α crystals) at T^M = 1580 K is mixed with **R** magma (75% melt + 25% β crystals) initially at T^R = 1620 K. The fraction of **M** in the mixture is f_o = 0.7. Hybridized **H** magma is invariant point magma with 98% melt of eutectic composition, 1.1% α and 0.9% β crystals by mass. Upon reflection, this result can

be understood by reference to the constraints imposed by enthalpic considerations. The probability of a particular **H** magma phase assemblage outcome should be proportional to the fraction of **H** system enthalpies that fall within a given phase assemblage enthalpy increment as illustrated in Figure 3. Specifically, if we define $\Delta H = H_{Gmax} - H_{Gmin}$ we can make the following predictions based on Figure 3 for the probability distribution:

1. L fraction = $(H_{Gmax} - h_{max}) / \Delta H$
2. Σ [(L + α) + (L + β)] fractions = $(h_{max} - h_{mid}) / \Delta H$
3. L_e+ α + β fraction = $(h_{mid} - h_{min}) / \Delta H$
4. α + β fraction = $(h_{min} - H_{Gmin}) / \Delta H$

In fact, the *a priori* computed fractions defined above are indeed in strong agreement with the results of the Monte Carlo simulations: the fraction of phase assemblage outcomes for **H** magma can be predicted *a priori* simply on the basis of enthalpic considerations. Because of the large range of system enthalpies in the three-phase region, a large fraction of end states lies at the eutectic point in the toy model (see APPENDIX I for further discussion of Figure 3 implications).

The application of such a 'thermodynamic attractor' phenomenon to natural systems requires further evaluation using more complex modeling tools. The variance in natural systems is higher, in general, than in the toy model and that could complicate matters. At the same time, two natural systems spring to mind where invariant points arguably control melt compositions. First are the prototypical ternary eutectic mantle systems Mg_2SiO_4 - $CaMgSi_2O_6$ - $CaAl_2Si_2O_8$ and Mg_2SiO_4 - $CaMgSi_2O_6$ - $Ca_3Al_2Si_3O_{12}$ involving the assemblages L+olivine+clinopyroxene+plagioclase (for shallow mantle) and

L+olivine+clinopyroxene+garnet (for deeper mantle). A second is the granite ternary system of quartz+alkali feldspar+plagioclase where the ternary minimum is a pseudo-invariant point. The fact that these two systems are relevant to partial melting of mantle peridotite to form basaltic liquids and the petrogenesis of granite (*sensu lato*) suggests that a petrologic 'attractor', or energy well associated with an invariant point, may be relevant in mantle and crustal magmatism. Some further exploration of this phenomenon is given in section 4.9.

4.2 Anomalous thermal effect

A reasonable but naive expectation is that when magmas mix, the temperature of the hybrid product will lie between the temperatures of the starting magmas, **M** and **R**. That is $T^H \in [T^M, T^R]$ in the notation of the toy model. Although this is true when two compositionally distinct *melts* mix to form a hybrid *melt*, this is not necessarily true when magmas mix. Analyses of the MC realizations showed that 10-20% of all cases exhibited an anomalous thermal effect wherein the temperature of **H** magma was less than *both* starting temperatures of **M** and **R** magmas. An example is illustrated in Figure 5a. **R** magma (80% melt + 20% β crystals) at initial temperature T^R = 1750 K is mixed into **M** magma (79% melt + 21% α crystals) at T^M = 1612 K and hybridized. Hybrid magma is sparsely phyric (96% melt + 4% α crystals). The temperature of hybrid magma T^H of 1579 K is 171 degrees less than T^R and 33 degrees less than T^M. Again, this is at first an unexpected result until one realizes that temperature and specific enthalpy do not bear a one-to-one relationship in an equilibrium mixture of crystals plus melt. It is the *enthalpy* that is constant during the mixing process; the temperature of hybridized magma is the result of enthalpy balance that includes sensible and latent heat effects. In this example, the fraction of melt in **H** is greater than the corresponding melt fractions in **M** and **R** yet the temperature of **H** is lower because, relative

to solid, silicate liquid has a higher specific enthalpy and specific heat capacity. In Figure 5b, an example is presented where **M** lies on its liquidus at 1636 K where it is just saturated in α and **R** is 46% β crystals + 54% melt at T^R of 1650 K. The resultant hybrid magma is crystal-free at 1593 K which, again, is less than both T^M and T^R. Additional toy model solutions (not shown) enable one to explicitly correlate the magnitude of the anomalous thermal effect with the crystal content of **M** and **R**. The magnitude of the thermal effect can be up to ~100 degrees for reasonable choices of initial conditions – this does not appear to be an insignificant effect.

The possibility of mixing hot recharge **R** into resident magma **M** of similar high temperature (or *vice versa*) and ending up with hybridized magma significantly *cooler* than either has not been widely appreciated. To investigate this phenomenon further, I used the Magma Chamber Simulator (MCS) software to evaluate if this unusual thermal effect continues to be quantitatively significant in multicomponent-multiphase scenarios of isenthalpic R-hybridization. In the MCS, the thermodynamic simplifications of the toy model are not invoked. Hence one may determine if the anomalous thermal effect applies to more realistic multicomponent-multiphase systems characterized by non-ideality in the melt and crystalline solutions, temperature and pressure dependent properties and the incorporation of H_2O and oxygen fugacity buffers. These effects, of course, are missing from the toy model by design. The question is: does this anomalous thermal effect pertain to complex systems or is it an artifact of the simplicity of the exploratory toy model?

Details of a relevant example to examine the reality of the anomalous thermal effect are given in Table 1. This example was performed using the Magma Chamber Simulator of Bohrson et al (2013), a high variance multiphase, multicomponent magma mixing model.

Crystal-rich resident magma **M** of crystallinity ~43% (clinopyroxene ~17%, plagioclase ~10%, spinel ~9% and olivine ~7% by mass) and basaltic melt (51.2 wt. % silica, 7.2 wt. % MgO, 0.6 wt. % H_2O, see Table 1) at 1180 °C is mixed with basaltic melt **R** that is more magnesian and somewhat wetter (7.7 wt.% MgO, 2.6 wt. % H_2O, see Table 1) also at ~1180 °C. **R** magma is at its liquidus temperature and olivine is the liquidus phase. The mixing ratio is 1.11 (approximately equivalent to a toy $f_o = 0.53$); i.e. roughly sub-equal amounts of **M** and **R** were mixed in this example. The resulting **H** magma (post R-hybridization) has a crystal content of ~13 wt. % (olivine ~6%, spinel ~5 % and clinopyroxene ~2 % by mass) and a temperature of 1152 °C. That is, T^H is ~28 °C less than the initial temperatures of both **M** and **R** of 1180 °C. Interesting effects are also noted for the composition of hybrid melt which is more aluminous and calcic yet poorer in FeO compared to melt in **M** and **R**. All plagioclase from **M** has been resorbed; no plagioclase is present in **H** magma. Several additional MCS calculations were done to quantify the relationship between the initial crystal content of **M** and the magnitude of the anomalous thermal effect. The results indicate that there is ~0.8 degree drop in hybrid magma temperature for every percent increase in the total crystal content of **M** magma when **R** magma is entirely molten. The conclusion is that the anomalous cooling effect is *not* an artifact of the simplified toy model. The basis of the effect is in the enthalpy buffering capacity of crystals. Phases with high specific (per unit mass) fusion enthalpies will be more effective in producing anomalous cooling effects. The practical importance of the anomalous thermal effect with respect to geothermometry in magmatic systems remains to be more fully explored. It does not appear, for example, that this thermal effect would be large enough in a natural system to affect wallrock assimilation potential. The magnitude could, however, be enough to affect

temperature sensitive phase compositions (e.g., Fa-Fo in olivine). The main point is that this might be a somewhat common effect when crystal-bearing magmas are mixed and allowed to hybridize, and such an effect may leave cryptic evidence of mixing events.

4.3 Reaction of stoped blocks with Resident M magma

Daly (1903) defined magmatic stoping as magma emplacement due to the detachment of blocks of magma-chamber roof and/or wall rocks and their incorporation into the magma body. Stoping itself involves a number of interrelated processes, including fracturing aided by preexisting foliation, bedding or fissility and thermal expansion, partial melting, and possible explosive exfoliation if stoped blocks include hydrous phases that become unstable upon heating to magmatic temperatures. Here a few simple R-hybridization scenarios showing the effects of composition and temperature of stoped blocks on the state of hybrid magma for a fixed **M** magma state are illustrated. Many examples exist in the literature where geochemical and petrological evidence of digestive assimilation is strong. Although these complex multicomponent systems cannot be explicitly described using the toy model, the fundamental principles of digestive assimilative hybridization can be explored and carried over to more complex systems.

Figures 6a and 6b illustrate the effects of cold stoped block composition on the final state of **H** magma. In example 6a, initial **M** magma is 87% melt and 13% α crystals by mass. The bulk and melt composition of **M** magma can be determined from Figure 6a where the fraction of **M** magma is $f_o = 0.9$ in the **M**+**R** mixture. In Figure 6a the stoped block is well below the solidus with a mode of 86% β and 14% α. Hybridized magma **H** is ~28 degrees cooler than **M** and is 81% melt and 19% α crystals. **H** melt is richer in component B relative

to **M** melt ($X^{H\ell}$ = 0.26 vs. $X^{M\ell}$ = 0.16) reflecting the β-rich mode of the stoped block. Note that although the stoped block is β-rich, the resulting hybridized magma remains under saturated in β phase. In Figure 6b, all values are identical to Figure 6a except that now the stoped block mode is 86% α and 14% β crystals, the modal opposite of Figure 6a. In this case, the hybridized magma temperature is only 11 degrees cooler than T^M but, at the same time, considerably more crystal rich (26% α crystals). Note that the initial T of the stoped block (T_o^R) is identical in these cases; differences in the **H** magma are simply related to the change from β-rich (Figure 6a) to α-rich (Figure 6b) blocks being assimilated and digested. The smaller degree of cooling for the case illustrated in Figure 6b is mostly due to the smaller heat of fusion of β crystals relative to α crystals, showing directly how thermodynamic properties can influence hybridization and post-mixing magma temperature.

The effect of the temperature of stoped blocks on the state of **H** magma is shown in Figure 7. All parameters are identical to the case of Figure 6b except that the pre-mixing stoped block temperature is reduced by a factor of two (from 1300 K to 650 K). Hybrid magma cools to 1601 K (cf. 1611 K in Figure 6b) and the mode of **H** magma is 37% α crystals vs. 26% α crystals in Figure 6b.This result shows that when the mixing ratio is large (i.e. the stoped block size is fairly small relative to the size of the magma body), the final temperature of the hybridized magma is only a weak function of the temperature of the stoped block, whereas the mode of the stoped block can have a fairly significant influence on the final temperature of **H** due to differences in fusion enthalpy between different phases. This implies the possibility that in natural systems not all stoped blocks behave the same. The thermodynamics illustrated above suggest that a magma body assimilating a detached chunk

of peridotite from its root may evolve differently than that same magma body assimilating a detached chunk of granitoid from its roof (assuming, as always, adequate time and mixing to achieve thermodynamic equilibrium and the hybridization limit).

4.4 Diabatic hybridization

All of the examples presented above have been for adiabatic cases, or R-hybridization. Recall that this is an isenthalpic process in which the total enthalpy is conserved between the initial (**M**+**R**) and final (**H**) states. Earlier the diabatic parameter Φ was introduced. Φ is the ratio of hybrid magma enthalpy to the sum of enthalpies of **M** and **R**; $\Phi \equiv \left[\frac{h^H}{(h^M+h^R)}\right]$. Conceptually, for Φ < 1, one may consider that a net heat loss occurs during the mixing process so that the hybrid magma state reflects both the process of adiabatic recharge plus the effects of heat extraction. An example of RFC-hybridization is portrayed in Figure 8. The initial conditions are identical to those of Figure 9 (described in detail below) except that in Figure 8 Φ = 0.8. It is noted that the hybrid state is subsolidus with mass fractions of α and β of 0.55 and 0.44, respectively. The loss of heat in this example of diabatic recharge is sufficient to induce complete crystallization in the mixed product. This is a very different outcome compared to the one illustrated in Figure 9 for which the hybrid state was nearly all liquid. Cycles of recharge followed by periods of cooling and fractional crystallization are thought to underlie magmatic evolution in a wide variety of petrotectonic settings (see references cited in introduction for a few examples). In some of these settings, such as at a MOR, the contribution of anatexis to the magma system may be relatively small in many cases. Prevailing models used to explain ophiolite generation rely upon partial melting, recharge and fractional crystallization processes with less emphasis on

assimilation (e.g., Zhang et al, 2014). Partial melting, recharge and crystallization can all be explored transparently using the Φ parameter within the toy model.

4.5 Cessation of phase precipitation

In many cases, cessation of precipitation of the saturation phase of **M** occurs even when the mixing ratio (mass ratio of **M** to **R**) is > 1 (i.e. $f_o > 0.5$). That is, even when the mixture is dominated by **M** end member, the process of magma mixing acts to suppress the crystallization of a phase that was saturated in **M** before mixing. In Figure 9 an example is shown where **M** magma, saturated in α (79% melt + 21% α crystals), is mixed with **R** magma saturated in β (71% melt + 29% β crystals). The resulting hybrid magma is 98% melt and 2% β. Despite a mixing ratio of 2 ($f_o = 0.67$), phase α is not present in hybrid magma **H**. Resorption upon adiabatic (isenthalpic) mixing of magmas and associated cessation of crystallization of a phase has interesting petrographic implications. A sample with this history would exhibit no evidence of its previous saturation with phase α. How would a petrologist know based on this sparsely β-phyric sample that it formerly contained α crystals? Such a scenario could be part of a possible solution to the classical 'pyroxene paradox' relevant to MORB petrogenesis (e.g., Francis, 1986). This 'paradox' arises from observations of sparsely-phyric MORB's whose melt (now glass) trace element signatures indicate that *pyroxene fractionation has taken place even though no pyroxene phenocrysts are apparent in the sample*. One resolution of the paradox is to presume fractionation (possibly polybaric) of pyroxene took place at depth (high pressure). Then as magma ascends and if pyroxene is no longer saturated in the melt because of the lower pressure, the melt will exhibit trace element

characteristics of pyroxene saturation even though pyroxene is not observed as a phenocryst or microphenocryst (e.g., Bence et al, 1979; Kinzler and Grove, 1992; Dantas et al, 2007).

The toy model may offer an alternative or additional explanation of the 'pyroxene paradox' in which magma mixing as well as fractional crystallization plays a role. In this scenario, consider the toy model phase diagram in terms of analogous geologic components and phases; component A is $CaMgSi_2O_6$ and component B is $CaAl_2Si_2O_8$ (see section 2.1). It follows then that phase α is pure diopside (clinopyroxene) and phase β is pure anorthite (plagioclase). A $CaMgSi_2O_6$ component-rich basaltic magma **M** at its liquidus (i.e., saturated with monoclinic pyroxene) with N-MORB bulk concentrations (ppm) of Cr, Ni, Sr, and Eu is emplaced in the shallow crust. This initial **M** cools and undergoes fractional crystallization of clinopyroxene. The clinopyroxene depletes coexisting melt in Cr and Ni but enriches the melt in Sr and Eu. These crystals are physically separated and form a cumulate pile (taking their Cr and Ni with them) that is no longer in equilibrium with overlying melt. After crystal removal, the remaining melt hybridizes with a pulse of recharge magma **R**. The composition of **R** differs from **M** in terms of major elements, it is anorthite-rich, but it has a bulk trace element composition identical to the original magma **M**. The mixing of **R** with the remaining post-crystal separation **M** melt creates a hybrid magma **H**. Once again some heat is lost to surrounding wallrock resulting in some degree of fractional crystallization of **H**. Shortly after fractional crystallization **H** is erupted as an equilibrium, phyric basaltic lava. So what are the trace element signatures going to look like? In the opening case of resorption upon isenthalpic mixing of magmas any trace elements housed within previously formed but resorbed crystals would simply be released back into the system. But in this slightly more complex but very plausible shallow crustal scenario the early precipitating clinopyroxene

was not resorbed, it was physically separated from the melt. Will such a scenario leave a fingerprint of those early clinopyroxene crystals that can survive recharge, hybridization and subsequent additional FC processes?

This was modeled as a serial FC–R-Hybridization–FC scenario (abbreviated as FC-R-FC).The relevent values are depicted in Table 2 and 3. An initially aphyric **M** undergoes fractional crystallization, crystallizing ~24% clinopyroxene (Table 2) resulting in a new magma denoted $\mathbf{M}^{*}$. Trace element partitioning during FC utilizes GERM database values for all trace elements (Table 4). For the second step *melt* of $\mathbf{M}^{*}$, denoted ($M^{*\ell}$) hybridizes with **R** and happens, in this instance to form an aphyric hybrid magma **H**. The incoming **R** is identical to the initial **M** in terms of trace element concentrations, but it contains ~24% by mass of anorthite so its melt has a depleted Sr/Eu signal relative to **M** (though its trace element *bulk composition* is identical to that of **M**). Finally a second episode of fractional crystallization occurs, partially crystallizing **H** magma, resulting in a new phase assemblage of $\mathbf{H}^{*}$ (Table 2). During this second round of FC, plagioclase crystallizes, affecting the Sr/Eu value of the $\mathbf{H}^{*}$ melt but not its Cr/Ni ratio value becasue while Sr and Eu are compatible in plagioclase Cr and Ni are both highly incompatible (Table 3). The results are plotted in ratio-ratio space in Figure 10.

The key point to consider is this: What is the geochemist to make of the composition of $\mathbf{H}^{*}$, a lava one might find in the field? Descriptively, it is a sparsely-phyric basalt containing ~5% plagioclase phenocrysts. The relevent bulk composition points in the plot are highlighted in Figure 10. The **H*** sample displays trace element trends that *cannot* be explained by simple FC with the phases present (glass + plagioclase) as a simple comparison of the **H** points against the N-MORB composition **M** and **R** points in Figure 10 reveals. If a

petrologist were to do a whole rock analysis they would discover that the bulk composition of this lava exhibits a depletion in Cr/Ni and an enrichment in Sr/Eu relative to its expected N-MORB origin (the concurrent points of C^M and C^R in Figure 10). This geochemical pattern is *not consistent with plagioclase fractionation*. So there could be a few explanations worth consideration. The first is to invoke a partial melt of a mantle source which has unique Cr/Ni and Sr/Eu ratios. In this case the trends observed in $\mathbf{H}^*$ would simply be representative of this unique pod of mantle material which is similar to but not precisely the same as average DMM. A second explanation could be polybaric fractionation of clinopyroxene. Such an explanation suggests clinopyroxene precipitating at depth, imparting a distinct trace element signature on the rising melt and leaving behind the clinopyroxene crystals themselves (e.g., Bence et al, 1979; Kinzler and Grove, 1992; Dantas et al, 2007). As the melt reaches shallower depths, however, clinopyroxene is no longer a liquidus phase – but plagioclase is. Thus $\mathbf{H}^*$ exhibits the trace element signature of clinopyroxene crystallization but those crystals were left behind at greater depths as the melt migrated upwards. By the time $\mathbf{H}^*$ erupted it was simply a sparsely-phyric basalt with plagioclase as its liquidus phase. This is a broadly accepted resolution to the 'pyroxene paradox'. However in the case presented here, we *know* that neither of those explanations is correct. The actual explanation, in this case, is a simple case of isobaric FC-R-FC consistent with shallow crustal processes. The FC-R-FC scenario invokes a similar mechanism to the polybaric pyroxene fractionation hypothesis (early clinopyroxene crystallization and separation), however the FC-R-FC model does not require the polybaric crystallization to explain the resulting trace element signature. Thus *isobaric* FC-R-FC processes can impart a geochemical signature similar to those predicted by other contemporary hypotheses invoked to explain the 'pyroxene paradox'. This is not a new

revelation, however. In fact, magma mixing was proposed almost forty years ago as an explanation of the pyroxene paradox (e.g., Rhodes et al, 1979; Walker et al, 1979). This proposal is consistent with results of the toy model, specifically during FC-R-FC hybridization under isobaric conditions.

4.6 Anomalous trace element concentration effect

The following section explores several examples of trace element behavior exploring various mixing scenarios.

4.6.1 R-Hybridization in Toy using Two Trace Elements

When two *melts* hybridize, the concentration of trace elements in hybridized melt is simply the mass-fraction weighted average of the concentrations in **M** and **R**; that is, $C_o^H=\left(f_o C_o^M\right)+\left[\left(1-f_o\right)C_o^R\right]$ since the bulk composition of **M** and **R (**C_o^M and C_o^R, respectively) magmas are identical to the compositions of **M** and **R** liquids (C_ℓ^M and C_ℓ^R, respectively). When two *magmas* mix and hybridize, however, the concentration of trace elements in **M** and **R** liquids bears no simple relationship to C_o^H. Instead, the concentrations in **M** and **R** liquids must be determined by simultaneous solution of enthalpy and trace element conservation expressions, as described in section 3. An example is illustrated in Table 5. Hybrid (**H**) magma was formed by the mixing and thermodynamic equilibration of α-saturated **M** magma $\left(w_\ell^M = 0.75,\ w_\alpha^M = 0.25\right)$ with β-saturated **R** magma ($w_\ell^R = 0.53,\ w_\beta^R = 0.47$). The mass fraction of **M** in the mixture (f_o) was 0.85. The trace elements Y and V are modeled using concentrations and partition coefficients from Table A2-2. Values are realistic for a model basalt system where phase α corresponds to

clinopyroxene and phase β to plagioclase. Before mixing, the concentration of Y and V in **M** and **R** melts are 24 and 200 ppm and 56 and 457 ppm, respectively. Hybridized magma (w_{ℓ}^{H} = 0.8, w_{α}^{H} = 0.2) contains melt concentrations of Y and V of 25 and 209 ppm, respectively. The point is that *despite the significantly elevated concentrations of Y and V in the incoming magma **R** melt, the hybridized melt shows essentially no enrichment in Y and V allowing for analytical uncertainties*. It would be very difficult if not impossible to reliably estimate the mixing ratio and to establish the end-member mixing components using the concentrations of Y and V in **H** melt in this example. In fact, based on these trace element concentrations one might conclude that magma recharge had *not* occurred, clearly an incorrect conclusion! This example shows that a thermodynamic solution that self-consistently defines the phase proportions and compositions from first principles is required to accurately model an evolving open magmatic system. If one used phase proportions observed in a sample, and if there has been any physical separation of phases, for example by gravitative mechanisms, then simply performing a trace element balance based on the *observed* assemblage in order to estimate source compositions or constrain end-member mixing magmas would be inaccurate if not impossible.

4.6.2 RFC-Hybridization in Toy using Two Trace Elements

As a second example, consider RFC-hybridization. Relevant parameters are given in Table 6. In this example, **M** and **R** magmas are first mixed (R process) and then the resulting **H** magma undergoes additional crystallization (FC process). The diabatic parameter is Φ = 0.94 which means that in the final state, hybridized magma **H** possessed 94% of the total enthalpy of the mixing 'components' **M** and **R** weighted according to their respective mass

fractions. The temperature and phase state of **M** and **R** magmas were 1630 K, $w_{\ell}^{M} = 0.8$, $w_{\alpha}^{M} = 0.2$ and 1640 K, $w_{\ell}^{R} = 0.77$, $w_{\beta}^{R} = 0.23$, respectively. The fraction of **M** magma in the mixture was $f_o = 0.66$. The **H** magma state after RFC-hybridization was $T^{H} = 1552$ K, $w_{\ell}^{H} = 0.75$, $w_{\alpha}^{H} = 0.25$. The trace elements Sr and Ni were modeled using concentrations and partition coefficients from Table A2-2. Values are realistic for a model basalt system where phase α corresponds to clinopyroxene and phase β to plagioclase. Before mixing the concentrations of Sr and Ni in **M** and **R** melts were 124 and 84 ppm and 81 and 129 ppm, respectively. It is noted that melt in hybridized magma **H** contained concentrations of Sr and Ni of 132 and 80 ppm, respectively. *The important point is that the concentrations of Sr and Ni in hybridized melt lie outside the range of values in **M** and **R***. That is, the concentration of Sr in **H** melt was *higher* than the concentration of Sr in both **M** and **R** melts. Likewise, the concentration of Ni in **H** was *lower* than that in both **M** and **R** melts.

4.6.3 The Dilution Effect in Toy using Four Trace Elements

A third example is summarized in Table 7 and is also presented graphically in Figure 11a. This example describes the 'Dilution Effect' which can occur when the enthalpy of the mixed system is high enough that fusion of pre-existing crystals in **M** and/or **R** creates a sparsely phyric **H** magma. If the crystals that melted during hybridization were depleted in a particular trace element, then melt of the hybrid **H** magma will be similarly depleted in that element relative to the initial **M** and **R** melts. In this case the concentration of Eu in the melt phase of **H** ($C_{Eu}^{H\ell}$) was ~15% lower than its concentration in *both* starting magma melts **M** and **R** ($C_{Eu}^{M\ell}$ and $C_{Eu}^{R\ell}$, respectively), which had similar initial Eu concentrations at 36 ppm and 37 ppm, respectively. The general expectation, incorrect in this case, is that upon

hybridization new magma would have a concentration of each element somewhere between the two initial magmas. While this is true of the magma bulk composition, it clearly does not have to be true of the phases that make up the magma (i.e., in the solids and melt of the magma).

The data for this example can be observed in a variety of plot types. Figure 11a plotted one element against another in a traditional element-element Harker variation diagram (Harker, 1909). Another type of plot used to test mixing hypotheses more succinctly is a ratio-ratio plot involving four different trace elements or major element oxides. A mixture will be hyperbolic in ratio-ratio space (see APPENDIX III), with the end members of mixing bracketing the hybrid product(s). In our terms, there are two types of hyperbola that can be plotted. The first is the standard mixture hyperbola, dictated by the mixing of initial magmas **M** and **R** based upon their bulk compositions to produce a hybrid magmas **H**. These are termed bulk composition mixing hyperbolas and are the ones commonly used by geochemists. A second type of mixing plot uses the *phases* in each distinct magma **M**, **R** and **H.** These are called phase mixture hyperbolas and are generally distinct from their associated bulk composition hyperbolas, sometimes remarkably so. If an element is not fractionated between phases, such as in the case of isotopes or if a ratio is chosen using elements that have identical partition coefficients, each of the phase hyperbolas collapse to one point – that of each magma's bulk composition (see APPENDIX III for a detailed discussion of mixing hyperbolas). In such a 'degenerate' case, however, the bulk composition hyperbola involving **M**, **R** and **H** persists as a distinct mixing curve. The amount of spread between the phases in ratio-ratio space is determined by the element ratio chosen and the phase mass fractions as defined in Equation (6). Ratios composed of elements with very similar geochemical

behavior will result in less separation along the phase mixing hyperbola than ratios constructed of elements with different partition coefficients. In the isotopic case, there is no appreciable fractionation between, say, ^{87}Sr and ^{86}Sr because the partition coefficients for ^{87}Sr and ^{86}Sr are virtually identical. Consequently, isotope ratio-isotope ratio plots can be used to define bulk compositions (see Equation (6) and let the K's for ^{86}Sr and ^{87}Sr be identical). It follows that the farther the ratio of partition coefficients is from unity, the more separation will be observed between phases in ratio-ratio space provided the mass fractions of coexisting phases (e.g., w_β in Equation (6)) is fixed. The mass fractions of coexisting phases also enters into the expression that determines the location of a phase on the ratio-ratio plot. This again shows why a self-consistent phase equilibration solution is needed in order to render trace element mass balances meaningful.

To illustrate this, Figure 11b includes not only the magma mixing hyperbola **M**+**R** = **H**, but also phase mixture hyperbolas for each distinct magma **M**, **R** and **H**. Figure 11b illustrates the expansion of phase hyperbolas when the trace element ratio is such that the ratio of their partition coefficients is not unity. In this space the ratios were constructed such that C1=Eu, C2=Sr, C3=Y and C4=V (see APPENDIX III for ratio-ratio plot conventions). The data is the same used to generate Figure 11a. Because Sr and Eu have similar geochemical behavior (i.e. similar partition coefficients for the solid phases α and β), and likewise V and Y behave similarly to each other (but opposite that of Sr and Eu), constructing ratios of like-behaving elements decreases the spread of the data between phases. The precise location in ratio-ratio space of a phase depends on the partition coefficients as well as phase abundances as given in Equation (6).

An aid in evaluation of hyperbolic trends is to linearize the hyperbolas; a perfectly linear trend is easy to identify and offers strong evidence for mixing. 'Companion plots' are constructed for this purpose. Figures 11c and 11d are the companion plots for the data used to generate Figure 11b. Note that in each companion plot, each of Figure 11b's four hyperbolas (**M** phase, **R** phase, **H** phase and the mixture hyperbola) are linear, creating an easy visual aid to check for mixing. This is particularly useful when testing a mixing hypothesis using samples thought to be products of mixing (in this context using two or more **H**'s to constrain **M** and **R**).

4.7 Evolution of melt during serial recharge

An example of application of the mixing hyperbola plot to results generated by serial recharge of **R** magma into resident magma **M** is presented in Figure 12. The experimental design was to start with initial resident magma **M0** and serially inject a small mass of compositionally distinct recharge magma **R** (specifically, $f_o = 0.95$, or the **R** increment being 5% of the total mass of the **M**+**R** system). So, to be clear, an initial magma body of 0.95 mass units had 0.05 mass units of **R** added to it for a total of 1.0 mass unit. The resultant hybrid magma **H1** then became the basis of the new resident magma **M1** for the next iteration. Because $f_o = 0.95$ was held fixed at each iteration throughout the experiment, **M1** (**M1** = **H1** in terms of composition, temperature and phase assemblage and proportions) constituted 0.95 mass units of the new magma chamber to which an additional 0.05 mass units of **R** (fixed in composition and temperature) was added. This experimental design creates a waxing (growing) magma chamber as increments of **R** are added to **M** and hybridized. This process was repeated for 90 iterations, (i.e. a 0.95 mass unit aliquot of **M** was always mixed with a 0.05 mass unit aliquot of **R**). Conceptually, the magma chamber

inflates due to serial recharge. The result was that **M** evolved from starting magma **M0** to **M1**, **M2**, ⋯, **M90**. **M** evolved in ratio/ratio space as depicted in Figure 12. For each iteration, the trace element concentrations were monitored for both the bulk composition (orange triangles) and melt phase (green circles) of each successive **H**. Evolution of the bulk composition of **H** (in this discussion bulk compositions are denoted by the naught subscript; e.g., $\mathbf{H_o}$) can be observed in the orange triangles in Figure 12, with the very first $\mathbf{H_o}$ represented by the largest triangle, close to the bulk composition of **M0**. Evolution of the melt of each **H** (melts are denoted by the script ℓ subscript; e.g., $\mathbf{H_\ell}$) can be observed in the green circles, with the very first $\mathbf{H_\ell}$ represented by the largest green circle located in the β-saturated field. Note that the bulk composition of each iterative $\mathbf{H_o}$ falls perfectly on the mixing hyperbola defined by the original **M** and **R**, as expected from previous discussions and APPENDIX III. As one might intuitively guess, the evolution of the bulk composition of **H** begins very close to the bulk composition of **M0** (because the first **H** was a product of mixing 95% **M** + 5% **R**), and then with each iteration **H** follows the mixing curve towards the opposite end-member component **R**.

What is less intuitive is the evolution of the melt phase $\mathbf{H_\ell}$. Note that **H** liquids generated early in the experiment plot in the β-saturated field, neither on a bulk composition hyperbola defined by initial $\mathbf{M0_o}$ and $\mathbf{R_o}$ (blue curve), nor on a melt composition curve defined by initial $\mathbf{M0_\ell}$ and $\mathbf{R_\ell}$ melt compositions (red curve). As iterative recharge events evolve the system toward an all liquid state, the melt composition trend of $\mathbf{H_\ell}$ approaches the bulk composition curve until, when **H** has no crystals left in it (i.e. it is 100% melt), **H**'s fall perfectly on top of the bulk composition curve. This makes sense because when there are no solid phases present, the concentration of any trace element in the melt is equal to its bulk

concentration, obviously (see section 3). As soon as crystals start to precipitate again (at this point in the magmatic evolution of this example, α crystals), the trace element ratio trend of **H** melt once again leaves the bulk composition curve. Given enough recharge events, the melt of **H** evolves toward the composition of the melt phase of **R** ($C^{R\ell}$) while concurrently the bulk composition of **H** similarly evolves toward that of $\mathbf{R_o}$ (C^R). The key point is to recognize that if any physical separation has occurred after the generation of a phyric hybrid sample (e.g., filter pressing, crystal settling, crystal accumulation by floatation, melt extrusion) such that eruptive samples are no longer representative of bulk composition, they may not define a mixing hyperbola from which the original mixing components **M** and **R** can be reasonably constrained. However, if samples that *are* representative of bulk compositions are also analyzed and used to generate a "correct" mixing hyperbola, where the non-bulk composition **H**'s fall in relation to the bulk composition curve may yield valuable information about what phases were precipitating in equilibrium with that **H** melt, even if no phenocrysts are observed in the sample. Such an analysis may offer renewed insights into problems such as the pyroxene paradox described and cited previously in section 4.5.

Ratio-ratio plots are a common method geochemists use to analyze recharge and without recognition of the limitations expressed above, errors in interpretation can occur. It is noted that because heavy isotopes do not fractionate appreciably during phase change, ratio-ratio plots generated using isotopic data from crystals and/or liquids should accurately define bulk composition mixing hyperbolas from which end members of mixing (**M** and **R**) might be constrained. So for example $^{87}Sr/^{86}Sr$ vs $^{143}Nd/^{144}Nd$ of a series of mixing related lavas can be used to constrain (but not uniquely define, unfortunately) possible end member isotope ratios in the source. It is important to note, however that one can never be sure that

basalts truly sample two explicit end members. And even if they do, those end members cannot be uniquely defined by a mixing hyperbola, only constrained to fall *somewhere* on the mixing hyperbola and bracket the mixture products. In any case the distinction between liquid and bulk compositions and use of trace element ratios vs isotope ratios must be kept in mind when doing mixing calculations. In the next section these ideas are explored further using the high variance multiphase-multicomponent Magma Chamber Simulator of Bohrson et al (2013).

4.8 Magma Chamber Simulator (MCS) Exploration of the Effects of Fractional Crystallization on Major Oxide Ratio-Ratio Plots

It is useful to consider the systematics and limitations of ratio-ratio mixing hyperbolas in the context of magma hybridization in high variance multicomponent-multiphase systems. This is done here using results from two R-hybridization simulations conducted using the MCS. In these examples ratio-ratio plots are constructed using major element oxide compositions. Similar examples using radiogenic isotopic ratios and trace element ratios from toy model calculations are presented in the following section (4.9).

As previously discussed, a compact way to illustrate binary mixing is by use of ratio-ratio plots. Four composition variables, such as the mass fraction of an oxide or trace element (denoted C), are used to generate two independent compositional ratios such as C_2/C_1 and C_4/C_3. If the assumptions of magma mixing are valid, then the bulk composition of the fully mixed (hybridized) magma (**H**) will plot on a hyperbola defined by the bulk compositions of **M** and **R** magmas**.** Alternatively, any two hybrid magmas (**H1** and **H2**), related to each other in terms of the **M** to **R** mass mixing ratio $\mathfrak{R}_1=\frac{f_1}{1-f_1}$ and, $\mathfrak{R}_2=\frac{f_2}{1-f_2}$ where f_i is the mass

fraction of **M** magma contributing to **Hi** magma, can be used to define the hyperbola uniquely. To reiterate an important point from the preceding section, the locations of end member mixing components **M** and **R** on the mixture hyperbola cannot be uniquely determined from products (**H**'s); the constraint is only that both **M** and **R** must lie *somewhere* along the hyperbola and must bracket the mixture products. Although it is easy to define the ordinate and abscissa ratio asymptotes, these limits may not be particularly close to the actual mixing end-members **M** and **R**. A plot of C_2/C_1 vs. C_4/C_3 yields a hyperbola with a curvature that depends on a ratio formed from the two compositions used to define the mixing hyperbola $\left(\frac{C_1^M C_3^R}{C_1^R C_3^M} \text{ or } \frac{C_1^{H1} C_3^{H2}}{C_1^{H2} C_3^{H1}}\right)$. There are two companion plots related to the master C_2/C_1 vs. C_4/C_3 hyperbola: (1) C_2/C_1 vs. C_3/C_1 and (2) C_4/C_3 vs. C_1/C_3. Although companion plots provide no new information beyond that displayed in the mixing hyperbola, they are useful because mixing always results in linear trends on companion plots and therefore the validity of mixing can be easily visually evaluated in companion plot compositional coordinates.

R-hybridization results from MCS calculations are summarized in tables 8a and 8b and portrayed in Figure 13a in the ratio-ratio coordinates SiO_2/ Al_2O_3 *vs* MgO/FeO. The end-member magmas **M** and **R** are identical for hybrid magmas **H1** and **H2**, which differ solely by their respective mixing ratios ($\mathfrak{R}^{H1}$ = 1.11 and $\mathfrak{R}^{H2}$ = 1.86). The bulk compositions of **R, H1, H2** and **M** must, by definition, lie along the mixing hyperbola (in figures 13a and 14a the mixing hyperbola is the solid blue line while the bulk compositions are denoted C^R, C^{H1}, C^{H2}, and C^M, respectively). **H2** magma lies closer to **M** because of the larger fraction of **M** in it compared to **H1**. Three additional mixing hyperbolas defined by phase equilibria are also

depicted on Figure 13a (red dashed line for **M**, green dotted line for **H1**, green dash-dot line for **H2**; **R** has no phase hyperbola as it is 100% melt). Each one connects the phases in equilibrium in a particular magma, as discussed in section 4.6.3 Whereas the locations of (bulk) **H1** and **H2** along the **M-R** mixing curve depends on the mixing ratio $\Re$, the locations of coexisting solid and melt in **H1** and **H2** are controlled by thermodynamics. For example, for **H1** the following identity is valid for the compositional ratio C_2/C_1 in **H1** bulk magma:

$$\frac{C_2^{H1}}{C_1^{H1}} = \frac{f_1 C_2^M + (1-f_1)C_2^R}{f_1 C_1^M + (1-f_1)C_1^R} = \frac{w_s^{H1} C_{2,s}^{H1} + (1-w_s^{H1})C_{2,\ell}^{H1}}{w_s^{H1} C_{1,s}^{H1} + (1-w_s^{H1})C_{1,\ell}^{H1}} \qquad (7)$$

This relationship explicitly incorporates the magma hybridization duality between mass balance in terms of the mixing end-members **M** and **R** and the requirements imposed by phase equilibria energetics on the resulting hybridized magma **H**. One of two possible companion plots to Figure 13a is shown in Figure 13b. The coordinate space for Figure 13b is Al_2O_3/FeO *vs* MgO/ FeO. This shows clearly the linear trends expected for mixing of **M** and **R** to give two hybrids (**H1** and **H2**). Note that all curves are linear. The mixing curve (denoted with a solid black line) and each phase curve where a given magma is composed of multiple phases are straight lines. Now consider that some crystal removal has taken place; figure 14a shows the effects of crystal removal. As noted from Table 8b, the equilibrium phases of **H2** magma are olivine (5.5%), clinopyroxene (7.1%) and spinel (6.5%). Figure 14a is identical to Figure 13a except that all of the clinopyroxene that was present in **H2** has been removed. As a result, the phase hyperbola connecting the glass and bulk solids in **H2** (green dot-dash curve) no longer passes through the known bulk composition of **H2** on the mixing hyperbola (solid blue curve). Figure 14b is once again one of two possible companion plots for figure 14a, again giving a linear relationship for easy visual comprehension. Note that in

this case, the phase equilibria line between the bulk solids and liquid for **H2** magma (C^{H2s} and $C^{H2\ell}$, respectively) do not cross through the bulk composition point for **H2**. In other words, for the case of Figures 14a and 14b, the bulk composition of **H2** lava disagrees with the apparent equilibrium mixing hyperbola for the bulk solids and glass present in the **H2** sample, thereby alerting one that this sample exhibits the effects of crystal-liquid separation. Inferences made from a sample such as this may not, therefore, be entirely reliable. The mixing hyperbolas have identified an apparent disequilibrium resulting from (in this case) missing monoclinic pyroxene. Of course, when a sample is collected in the field, there is no certain knowledge that crystal-liquid separation has or has not occurred, in general.

4.9 Mechanisms explaining the Geochemical Variability of Mid Ocean Ridge Basalts: the RFCAE model

4.9.1 Background

A central problem in petrogenesis is trying to explain the geochemical trends of eruptive and intrusive rocks in terms of petrogenetic processes, the most important of which include magma mixing, fractional crystallization, magma contamination *via* assimilation of country rock, partial melting and volatile exsolution. The most voluminous magma type on Earth is MORB associated with the formation of oceanic crust. The rate of MORB eruption/emplacement for the Earth is about 25 km^3 per year (White et al, 2006). This rate has not varied by more than 10-20 % throughout the last 200 million years (e.g., Coltice et al, 2013). MORB's are notable because they are relatively monotonous in major element composition but display trace element and isotopic signatures that can be variable, such as N-MORB vs. E-MORB (e.g., Varne et al, 2000; Workman and Hart, 2005; Waters et al, 2011).

In the 70's, two major hypotheses gained traction as potential explanations of observed trace element systematics in MORB. One hypothesis was that MORB's represent *primary magmas* – unmodified partial melts of the underlying heterogeneous mantle. The assumed primary nature of these melts implied the possibility to invert geochemical data and use MORB compositions to constrain the trace element composition of the (inaccessible) mantle. If the trace element and isotopic signature of the MORB was derived directly from the mantle source, the diversity of trends in MORB would be representative of the heterogeneity and degree of partial melting of the parental mantle source and hence shed light on the dynamics of subsolidus mantle mixing as viewed through the prism of recycled heterogeneous oceanic lithosphere comprising depleted mantle, altered oceanic crust and possible minor subducted sediments and sedimentary rocks. This hypothesis has received enormous attention in the past half century. A second less popular hypothesis posited that MORB's were the end product of shallow crustal processes including recharge, fractional crystallization (possibly polybaric), and assimilation of hydrothermally-altered gabbroic and hypabyssal volcanic rocks. This hypothesis was articulated especially by O'Hara and co-workers (e.g. O'Hara, 1967, 1972, 1977; O'Hara and Mathews, 1981, Niu and O'Hara, 2006, 2008) who acknowledged that while partial melts may be derived from mixed (heterogeneous) mantle subsolidus sources (such as eclogitic pods in a sea of peridotite), the partial melts may mix and accumulate in the shallow subsurface to form a magma body that may undergo further Recharge, Fractional Crystallization and Assimilation (contamination by stoping) before eruption on the sea floor or intrusion to form new oceanic crust (i.e., RFCA evolution). Hence, in this view MORB, rather than being a primary mantle melt, is a composition resulting from varying degrees of modification via crustal processes (i.e. mixing

of primary magmas, fractional crystallization and/or assimilation, and subsequent eruption - processes given the acronym RFCAE (Spera and Bohrson, 2004). Even cursory reflection reveals that both hypotheses allow for variations in the trace element and isotopic composition of MORB's. The significant issue then is the quantification of each hypothesis and comparison of predicted results with observations. It should be noted that these hypotheses are not mutually exclusive. The issue is: to what extent do shallow-level RFCAE processes obfuscate the signal from the deeper mantle region where partial melting occurs? Can one reliably 'invert' basalt compositions to infer heterogeneity of the subsolidus upper mantle?

Fortunately, both hypotheses can be explored by rigorous thermodynamic-based numerical experiments. In this section the second scenario is examined in detail using the binary eutectic toy model as an example. An exploratory RFCAE model for MORB petrogenesis was first articulated by M.J. O'Hara and published in the Journal of the Geological Society of London as *'[a model for the] geochemical evolution of an advancing, periodically replenished, periodically tapped, continuously fractionated magma chamber'* (O'Hara and Mathews, 1981). O'Hara's model was a composite analytical-empirical model that is mathematically complicated and difficult to use in practice. It is, in essence, a magma evolution model that includes recharge (magma mixing), isobaric fractional crystallization, assimilation of hydrothermally-altered mafic rocks and, finally, eruption of a portion of the melt (i.e. an RFCAE petrogenetic model). Unlike the O'Hara model that employed some heuristics and approximations from phase equilibria studies, the toy model, although simple, maintains full thermodynamic rigor. *In addition, and most significantly, the O'Hara model does not self-consistently handle the energetics of magma mixing, crystallization and*

assimilation. Hence it must be seen as an incomplete model that while pointing in the right direction is at best semi-quantitative. At any rate, the early pioneering steps taken by O'Hara must be recognized and acknowledged.

In order to assess the feasibility of using the toy model to explore the RFCAE petrogenetic MORB model, consider the latter in terms of a quadruplet of distinct magmatic process events:

1. Periodically replenished'
    - Mixing of magmas via recharge (*R*)
        - A primary recharge magma intrudes a preexisting resident magma (recharge **R** intrudes resident magma **M**) and the two mix thoroughly to create a hybrid magma **H.** Hybrid magma is the result of the thermodynamic equilibration of **M** and **R**.
2. 'Continuously fractionated'
    - Fractional crystallization occurs due to loss of heat to surrounding subsolidus wallrock (*FC*) - O'Hara compares and contrasts hypothesized geochemical consequences between equilibrium crystallization (EC) vs true FC, but uses EC in his computations.
        - Loss of heat stimulating magma crystallization is modeled using the Toy's Φ parameter. Recall from previous discussions that Φ is the fraction of total initial combined enthalpy that remains in **H** after hybridization. That is, $\Phi \equiv \left[\frac{h^H}{(h^M+h^R)}\right]$, where h^H is the specific enthalpy of hybrid magma **H**, h^M is the specific enthalpy of magma **M**, and h^R is the specific enthalpy of magma **R**. In order to simulate FC, the value

range of Φ used is $0 < \Phi < 1$. The amount of heat lost from the magma system is $(1- \Phi)$. In serial application of the Toy model, fractional crystallization is simulated although in any single step equilibrium crystallization is implemented since the phase diagram is based on a binary eutectic system for which equilibrium and fractional crystallization are identical (Bowen, 1928).

3. 'Advancing'

- Assimilation of wall rock into a resident magma chamber (*A*). This serves to affect the evolution of major, minor and trace elements as well as isotopic ratios because hydrothermally-altered wallrock is enriched in ^{87}Sr relative to ^{86}Sr due to reaction of fresh MORB with sea water. O'Hara used the term 'advancing' to describe the growth of a magma chamber, and specifically inferred the 'digestion' of wall rock. However, a magma body can be waning in volume even if assimilation occurs if heat loss is sufficiently large. Because stoped blocks of roof and wall rock are colder than resident magma (i.e., smaller specific enthalpy), the energetics of phase change, something that O'Hara did not explicitly include in his model, needs to be considered. Trace element mass balance solutions are not, in isolation, sufficient to rigorously test petrogenetic explanations. The toy model, being a rigorous thermodynamic model *does* self-consistently consider the energetics. Because O'Hara is modeling MORB, wallrock is considered to be previously erupted lavas, dikes, gabbros and other mafic rocks that have been hydrothermally-altered. The enthalpic load these cold altered rocks put on resident magma is

taken into account in the toy model used in this study but ignored in O'Hara's model. O'Hara uses the term 'digestion' to refer to the melting of hydrothermally-altered stoped block. This is misleading. Stoped blocks *react* with resident magma and, via hybridization, a new magma in internal equilibrium forms (**H** magma). Stoped blocks do not necessarily melt *per se*. Instead, thermodynamics dictates that a new equilibrium assemblage of melt plus crystal(s) is created consistent with the constraints of a new bulk composition and new system enthalpy. This procedure provides a self-consistent new temperature (a result of the computation, not artificially imposed by the 'hand of God' and a new assemblage of phases.

- In toy terms assimilation is addressed using stoped blocks, which are added to resident magma and allowed to come to complete thermodynamic equilibrium. Note that unlike the O'Hara model, where added blocks are completely digested by 'fiat', in the toy model no such assumption is made. Instead, thermodynamics dictates the fate of stoped blocks.

4. 'Periodically tapped'

- Eruption occurs (*E*)
    - In toy terms, a portion of the melt in the **M** reservoir (which is all liquid after removal of crystals in steps 1, 2 and 3 above) is removed, changing the mass of the **M** reservoir but not is composition, temperature or phase state.

The iterative approach of using the toy engine to model MORB evolution *via* magma mixing, fractional crystallization and assimilation (RFCA) followed by eruption (E) of a small increment of resident basaltic melt is depicted in Figure 15. Multiple iterations of the serial R-FC-A-E four-tuple are carried out, allowing one to track the temperature, enthalpy, mass and composition of all phases, trace elements and isotopes through an arbitrary number of RFCAE cycles. Although not relevant here, parenthetically it is thought that time intervals between recharge events along fast spreading ridge segments like the East Pacific rise are measured in months to years whereas along slow spreading ridges, such as the southeast Indian ridge (SEIR) time intervals may be years to decades (e.g., Sinton et al, 1991; Lin and Phipps Morgan, 1992; Carbotte and Macdonald, 1994).

A main conclusion of O'Hara is that a shallow mixed magma system consistent with crustal RFCAE can create similar geochemical patterns to those resulting from mixing of subsolidus sources coupled to variable extents of partial melting of the mixed sources and subsequent ascent and eruption. In other words, the ‘direct mantle melting’ and RFCAE scenarios for generating MORB cannot be differentiated based upon the eruptive products. O’Hara argued that a 'steady state' actively mixing magma chamber, that is, one with replenishment approximately balanced by eruption, can develop trace element signatures very similar to primary mantle partial melts formed by variable degrees of partial melting of a heterogeneous (variously enriched) source. Because in the case of MORB both the parental magma and the assimilated wallrock are broadly similar in major element composition provided metasomatism is not too severe, the eruptive products show relatively little variation in major element composition. The trace elements and isotopes, however, can be significantly different. In particular, the more incompatible a trace element is the more

exaggerated its pattern can become. Once again, it is important to note that the very idea of trace element compatibility or incompatibility cannot be unambiguously determined unless one has knowledge of the phase assemblage associated with phase changes. Geochemical mass balance models that neglect the energetic constraints supplied by a thermodynamic model are inchoate and may be quite misleading (e.g., Bohrson and Spera, 2001; Spera and Bohrson 2004; Fowler et al, 2004; Spera et al, 2007; Bohrson and Spera, 2007). Surprisingly, the literature is replete with trace element studies in which phase equilibria is assumed *a priori*.

MORB, relative to a truly primitive melt, should be much less enriched in the most incompatible elements because it is a partial melt of an already depleted source (DMM). So when a MORB is observed with higher than average LREE concentrations, does that indicate it was the product of partial melting of an enriched mantle source? If the RFCAE case is valid the eruptive products could have been considerably modified from the original parental magma, from which it follows that they were also modified from the original mantle source. Could the steady state RFCAE magma chamber be, in effect, a distillation chamber for incompatible elements? Could this then be an underlying mechanism of LREE enrichment, rather than invoking an enriched mantle source as explanation? Are there geochemical signals that are transparent to crustal processes and therefore give truly unique information on mantle sources regardless of which petrogenetic model (RFCAE vs primitive mantle melts) one invokes? Unfortunately, complete resolution of these questions awaits further study. An initial step is taken here, however.

4.9.2 Modeling the RFCAE Magma Chamber using the Toy

As outlined above, I modeled the RFCAE magma chamber using an iterative approach (Figure 15). My goal was to follow in detail the thermal and geochemical evolution of the melt, specifically, since most MORB's are sparsely-phyric or aphyric. To this end, at the completion of each modeling step (where each individual process in the R-FC-A-E petrogenetic model is accomplished as a distinct 'modeling step'), I subtracted any crystals (α and/or β) that had formed so that the *melt only* (mass, composition, temperature) was carried forward into the next step. This consistent removal of crystals is noted symbolically by a growing cumulate pile in Figure 15. The experiment began with an initial resident magma **M** of reasonable but arbitrarily defined composition (major element, trace element, isotopic ratio), temperature and mass. This initial **M** (which I will denote $\mathbf{M_o}$ to indicate the starting **M** prior to any modification) was sparsely-phyric, with ~1% β crystals and 99% melt. In the terms of the O'Hara model, $\mathbf{M_o}$ represents a pre-existing resident magma with an unknown history prior to initiation of the experiment – it is simply a starting point. $\mathbf{M_o}$ is then mixed and thermodynamically equilibrated with a completely aphyric (100% melt) recharge magma **R** of fixed mass, composition and temperature. In general **R** was not of the same composition as **M**, although it could be. I allowed **R** to be slightly more mafic than **M** for the sake of chemical contrast. Any resultant solids that formed due to magma mixing treated as an isenthalpic (adiabatic) process were subtracted and the remaining liquid was carried forward into the second step (FC) of the quad-tuple of R-FC-A-E. Fractional crystallization is simulated using the toy's Φ functionality (see section 2.1 for a discussion of the Φ parameter). Recall that $\Phi \equiv \frac{h^H}{(h^M + h^R)}$ so when $(0 < \Phi < 1)$ a portion (1– Φ) of the total enthalpy of the hybrid magma **H** has been lost to the surrounding subsolidus wallrock. Any

solids precipitating during this FC-step were subtracted and the remaining melt was carried forward into the third step (A) which modeled addition of a stoped block of wallrock of fixed mass, composition and subsolidus temperature. Any resultant crystals were removed and the melt, having now been modified by the R-FC-A processes, was carried forward into the final step of the four-tuple cycle which calculated the remaining mass of melt after removal of a fixed mass due to eruption. What remains after a complete R-FC-A-E cycle is a *melt* (a completely aphyric magma) of some mass, composition and temperature. This evolved melt then becomes the new starting **M** composition which enters the next RFCAE cycle. During each cycle a fixed **R** and **A** in terms of mass, composition and temperature were used. Ten cycles were performed and analyses were conducted on resultant melts at the end of each cycle. Because crystals were being continuously removed from the system (analogous to formation of cumulate piles) the melt evolves in the fashion of an open system undergoing concurrent magma mixing (recharge), fractional crystallization, and assimilation.

Three types of RFCAE magma chambers were created: waxing, waning and quasi-steady-state. Each of these starts out with an identical mass, enthalpy and composition symbolized by $\mathbf{M_o}$. The **R** used was identical in composition and temperature (specific enthalpy) among all scenarios, but the mass of **R** added to the resident magma was varied in order to simulate net growth, contraction or a constant mass magma body. The amount of enthalpy removed for the FC step (Φ) and the **A** used (mass, composition and temperature) were both identical in all three scenarios. The amount of mass removed for eruption (**E**) was varied between the chamber types. So essentially, because $\mathbf{M_o}$, Φ and **A** were constant , the type of RFCAE chamber created was a function of the balance between input from **R** and **A** vs output from removal of crystals to the cumulate reservoir and the mass of melt erupted **E**.

The amount of mass removed for eruption was controlled using a parameter $\gamma_E \equiv \left[\frac{m^E}{m^E + m^*}\right]$ where m^E is the mass erupted (removed) and m^* is the mass of melt remaining after the R, FC and A steps have been completed. Table 9 shows the initial conditions of **M**, **R** and **A** (consistent amongst all simulations) and Table 10 shows the conditions used to generate each of the three scenarios (input and output parameter values).

The metrics used to assess differences between the evolutionary paths of each chamber type were the changes in mass, temperature and bulk (major element) compositions through the course of multiple RFCAE cycles and the concentrations of four trace elements and the isotopic composition of Sr. It turns out that the process order (e.g., RFCAE vs AFCRE vs RAFCE, etc.) can have an quantifiable effect on the numeric results. I performed several cycles using different process orders and concluded that the maximum difference between respective results was small, on the order of 2-4%. I chose to use RFCAE because it produced numeric results that were an average between the most extreme results I could produce using different process orders.

Mass, temperature and bulk composition were non-dimensionalized by the initial mass, temperature and composition of the starting resident magma $\mathbf{M_o}$. The non-dimensionalized size of the chamber was defined by m^ℓ/m_o^M, where m^ℓ was the mass of melt remaining at the end of a complete RFCAE cycle and m_o^M was the mass of the initial unmodified resident magma $\mathbf{M_o}$. Specifically, temperature and major element composition were non-dimensionalized using $\overline{T} = \left[\frac{T - T_e}{T_o^M - T_e}\right]$ and $\overline{X} = \left[\frac{X - X_e}{X_o^M - X_e}\right]$ where T_e and X_e are the eutectic temperature and composition, respectively, as defined by the thermodynamics of the system (in this case the classic basalt system $CaMgSi_2O_6$ - $CaAl_2Si_2O_8$), and T_o^M and X_o^M are

the initial temperature and composition of $\mathbf{M_o}$, respectively (See Table A1-1 for a complete list of variable definitions).

One of the key ideas postulated by O'Hara is that the RFCAE process could produce trace element signatures similar to those produced by partial melts of a heterogeneous variously-enriched mantle source. As a first step towards evaluation of this hypothesis, I carefully tracked the trace element signature of the melt through each RFCAE cycle. I used unique but reasonable initial concentrations (ppm) in each mixing source (**M**, **R**, **A**) for each of four trace elements – Sr, Rb, V and Yb (see Table A2-2 and Table 9) – and modeled each as essentially N-MORB. The incoming **R** was modeled to be slightly more primitive than $\mathbf{M_o}$ in terms of bulk composition (i.e. more Mg rich with $X_o^R = 0.1$ *vs* $X_o^M = 0.605$). **R** was also modeled with a slight enrichment in Rb relative to $\mathbf{M_o}$, but is still well within the range of average N-MORB in Rb concentration (Gale et al, 2013). The wallrock was considered to be older lavas and cumulates, a collective product of previous RFCAE cycles that have been isotopically enriched in ^{87}Sr due to reaction with sea water but are otherwise again within the average range for N-MORB trace element concentrations (Gale et al, 2013). To augment the modeling of isotopic variation, I made $\mathbf{M_o}$ and **R** very similar in their $^{87}Sr/^{86}Sr$ ratio, as both in O'Hara's terminology are relatively unmodified parental magmas. However, I chose to make the wallrock (**A**) higher in its $^{87}Sr/^{86}Sr$ to simulate hydrothermally-altered gabbroic and hypabyssal volcanic rocks. Trace element and isotopic ratio evolution was tracked through each RFCAE cycle in all chamber scenarios.

4.9.3 RFCAE Modeling Results

Each chamber type was followed through 10 complete RFCAE cycles. The physical evolution of each chamber type is depicted in Figure 16 by plotting the RFCAE cycle number (1-10) against the non-dimensional chamber mass. The waxing chamber continuously inflated to ~1.65 m_o^M, the waning chamber continuously shrunk to ~0.4 m_o^M, and the steady state chamber, while varying slightly, maintained a mass of melt ≈ m_o^M throughout its 10 cycle history.

The non-dimensional temperature ($\overline{T}$) evolution of the three scenarios is depicted in Figure 17a, which plots the RFCAE cycle number against $\overline{T}$. Similarly, Figure 17b displays the non-dimensional major element composition ($\overline{X}$)evolution of the three scenarios. Note that while both the steady-state and waning chambers get stuck at the invariant point ($\overline{T}$ = 0, $\overline{X}$= 0 in Figures 17a and 17b, respectively) the waxing chamber rests at the invariant point at the end of cycle 2, but then moves off of the invariant point for subsequent cycles. The temperature for the waxing chamber steadily increases yielding a $\overline{T} > 0$ after cycle 2 while the composition evolves to be less than the eutectic composition X_e, resulting in $\overline{X} < 0$ after cycle 2. This was a result of the waxing chamber being achieved, in part, by large intrusions of **R** ($m^R = 0.25m_o^M$) relative to the other two chamber types ($m^R = 0.05m_o^M$ for the waning chamber and $m^R = 0.11m_o^M$ in the steady-state chamber). This translated into more mass of **R** being brought into the waxing magma chamber to help pull the composition towards that of **R** ($X_o^R < X_e < X_o^M$). It also translated into more enthalpy being brought into the magma chamber ($T_o^R > T_o^M > T_e$) which is needed to escape the energy well associated with the invariant point (see section 4.1 for a discussion on the eutectic point as a 'thermodynamic attractor'). This last point is worth careful consideration. The 'thermodynamic attractor'

might play an important role in MORB petrogenesis and the evolution of MORB magma chambers because it stalls the thermal and major element evolution of the hybrid magma **H** unless/until one of two things happens; either a large enough enthalpy is added to the system to elevate **H** off of the invariant point in to the liquid-only field (this requires enough enthalpy to completely melt any solid phases present), or a large enough foreign mass (i.e. **R** or **A**) hybridizes with the eutectic condition **H** to change the bulk composition sufficiently that the new **H** falls into one of the 2-phase fields (α+L or β+L). The only other option, in terms of the binary eutectic system, is that the magma remains trapped at the invariant point until the chamber has completely frozen (i.e. the last drop of eutectic melt, L_e, crystallizes). This could be one contributing reason for the monotony of MORB major element compositions, another being that invariant point partial melting of an olivine-orthopyroxene-clinopyroxene-garnet peridotite or a clinopyroxene-garnet eclogite or a mixture of these sources is invariant point (or nearly so) melting and hence generates a melt of fixed composition.

The geochemical evolution of all three chambers, as viewed in trace element ratio-ratio space, is depicted in Figure 18. The trends have been labeled with a '1' to indicate the first RFCAE cycle and a '10' to indicate the final cycle of the simulation. The trends for all three chamber types show consistent melt enrichment in Rb, the most incompatible element modeled (see Table 9 for partition coefficient assignments). This result is not unexpected as Rb is highly incompatible in all solid phases, and so will tend to remain in the melt throughout any processes resulting in fractional crystallization. Thus virtually all the Rb entering the magma chamber *via* **R** and **A** stays in the **M** melt, concentrating over the course of multiple RFCAE cycles. Yb, a less incompatible element, shows initial melt depletion

early in the evolution of the waning and steady-state chambers followed by a consistent melt enrichment trend from cycles 4-10. This 'hooked' Yb trend is not present in the waxing chamber, however. My interpretation of this result is that dilution effects associated with a waxing chamber don't become measurably apparent for a few cycles, as evidenced by the $^{87}Sr/^{86}Sr$ being comparable among all 3 chamber types through the first 3 RFCAE cycles (see Figure 19). However the large intrusion of **R**, which is 'depleted' in Yb in terms of ppm but has a large mass being added in the waxing chamber systematics, in conjunction with the small mass but highly Yb enriched stoped block of **A**, combine to be enough to mitigate the Yb 'hook' into a steadily enriching trend. Sr and V are compatible in one solid phase and incompatible in the other, with opposing geochemical behavior, so their melt concentrations can vary considerably depending on which solid phase (if any) is precipitating, which is why they were chosen as the ratio denominators and not the numerators. While the elements chosen for the numerators (Rb and Yb) have different degrees of incompatibility, they are equally incompatible in both solid phases, and as such their trends were relatively indifferent to solid phases coming and going during the system's evolution.

The isotopic evolution of the three RFCAE chamber types is shown in Figure 19. Although $\mathbf{M_o}$ and **R** were modeled as very similar isotopically, all three chamber types showed a steady climb in the $^{87}Sr/^{86}Sr$ of the melt. This is primarily a result of the highly enriched assimilated wallrock contaminating the parental magmas. Even though the contaminating mass is equally small ($m^A = 0.02m_o^M$) for all three scenarios, that small amount of material has such an elevated $^{87}Sr/^{86}Sr$ relative to the magma chamber that it dramatically pulls the hybridizing magmas well above either parental magma's initial isotopic ratio. The

isotopic composition points of $\mathbf{M_o}$, **R** and **A** are labeled on the plot for reference. This plot demonstrates a classic case of 'a little goes a long way'.

5. CONCLUSIONS

The overarching conclusion of this thesis is that the toy exploratory model does indeed offer many valuable insights into the fundamental mechanics underlying magma hybridization. The coupling of energetics to phase equilibria and trace element mass balances provides a self-consistent snap-shot of many causal mechanisms active during hybridization. Toy solutions offer confirmation of well accepted hypotheses as well as thought provoking examples of counter-intuitive behaviors. As such, the toy model is useful both as a teaching and research tool. Some examples of phenomena first recognized in toy model realizations have been corroborated using the complex multiphase-multicomponent model the Magma Chamber Simulator (MCS) of Bohrson et al (2013).

Specifically, experiments using the toy model have identified several phenomena associated with magma hybridization heretofore under-appreciated in the literature. The first is the idea of an energy well or 'thermodynamic attractor' associated with an invariant point. As discussed in section 4.1, 4.2 and 4.9, there are several geologic settings where eutectic point energetics could be playing an important role in petrogenesis such as L+olivine+clinopyroxene+plagioclase (for shallow mantle), L+olivine+clinopyroxene+garnet (for deeper mantle) and the granite ternary system of quartz+alkali feldspar+plagioclase where the ternary minimum is a pseudo-invariant point. The initial findings in this report based upon the thermodynamics of a simple isobaric binary

eutectic system have implications that extend beyond this report and suggest fertile ground for further research. Another exciting phenomenon identified by toy model research is the anomalous thermal effect. This is a quantifiable consequence when phyric magmas hybridize that offers testable hypotheses for cryptic evidence of magma mixing. This thermal effect has been verified using high variance modeling (MCS) and appears to be a very real and measureable effect that is a direct consequence of thermodynamics. An additional quantified idea explored by toy modeling is an *isobaric* mechanism explaining the 'pyroxene paradox' in MORB petrogenesis *via* FC-R-FC processes as discussed in section 4.5. The trace element and isotopic calculation functionality (described in section 3), combined with the variable enthalpy control built into the toy (explicated in section 2) to stimulate partial melting ($\Phi > 1$) or fractional crystallization ($\Phi < 1$) offer one a truly powerful tool for studying trace element partitioning systematics as demonstrated repeatedly in sections 4.5-4.9. The toy model can be a particularly powerful tool when used in an iterative or serial fashion. Contrary to its simple exterior it is capable of rigorous hypothesis testing, as demonstrated in sections 4.5, 4.7 and 4.9. In particular, example 4.9 demonstrates that a shallow mixed magma system consistent with crustal RFCAE can create enriched geochemical patterns in MORB (i.e., E-MORB) without invoking mixing of enriched subsolidus mantle sources.

I see the current version of the toy model as merely a seed from which more advanced variants can be developed. Solid solution, peritectic and ternary 'toys' are feasible and based upon the results using the binary eutectic toy I believe there is considerable potential for petrologic exploration. Additionally, the power of the iterative toy approach has been demonstrated not only in hypothesis testing, as employed in sections 4.7 and 4.9, but in exploration of systematics as discussed in section 4.1. As such, an automating shell using the

toy as an engine could be an extremely powerful tool for exploring magmatic systems requiring a serial or iterative approach to simulate. It could be very informative, for example, to undertake a Monte Carlo approach to the RFCAE magma chamber systematics.

Taken in conjunction with the multicomponent-multiphase models I believe the toy model (or suite of models if other versions are pursued) could be used to genuinely advance our understanding of magmatic processes. As such the toy model presented here, magmatically simple though it may be, has gone well beyond 'proof of concept' and proven itself to be a valuable tool in its own right.

6. REFERENCES

Albarede, F. (1995). Introduction to Geochemical Modeling. Cambridge University Press, New York.

Bence, A.E., Baylis, D., Bender, J.F. and Grove, T.L. (1979). Controls on the major and minor element chemistry of mid-ocean ridge basalts and glasses. *Implications of Deep Drilling Results in the North Atlantic, 2nd Ewing Syrup.*, pp. 331-341.

Bowen, N.L., *The Evolution of the Igneous Rocks.* New Jersey: Princeton University Press,1928.

Bohrson, W.A., and Spera, F.J. (2001). Energy-Constrained Open-System Magmatic Processes II: Application of Energy-Constrained Assimilation-Fractional Crystallization (EC-AFC) Model to Magmatic Systems. *Journal of Petrology, 42*, pp. 1019-1041.

Bohrson, W.A., and Spera, F.J. (2007), Energy-Constrained echarge, Assimilation, and Fractional Crystallization (EC-RA/É'/FC): A Visual Basic computer code for calculating trace element and isotope variations of open-system magmatic systems, Geochem. Geophys. Geosyst., 8.

Bohrson, W.A., Spera, F.J., Ghiorso, M.S., and Creamer, J. (2013). A tool for exploring the impact of crustal contamination; the magma chamber simulator. *Mineralogical Magazine, 77(5)*, 728.

Carbotte, S.M., and Macdonald, K.C. (1994). Comparison of seafloor tectonic fabric at intermediate, fast, and super fast spreading ridges; influence of spreading rate, plate motions, and ridge segmentation on fault patterns. *Journal of Geophysical Research, 99*, 13-13,631.

Carmichael, I.S.E., Turner, F.J., and Turner, J., *Igneous Petrology.* New York: McGraw-Hill, 1974.

Coltice, N., Seton, M., Rolf, T., Muller, R.D., and Tackley, P.J. (2013). Convergence of tectonic reconstructions and mantle convection models for significant fluctuations in seafloor spreading. *Earth and Planetary Science Letters, 383*, pp. 92-100.

Chamberlain, K.J., Wilson, C.J.N., Wooden, J.L., Charlier, B.L.A., and Ireland, T.R. (2013). New perspectives on the Bishop Tuff from zircon textures, ages and trace elements. *Journal of Petrology*.

Daly, R.A. (1903). The mechanics of igneous intrusion. *American Journal of Science, 15*, pp. 269- 298.

Dantas, C., Ceuleneer, G., Gregoire, M., Python, M., Freydier, R., Warren J., and Dick, H.J.B. (2007). Pyroxenites from the Southwest Indian Ridge, 9-16°E: Cumulates from incremental melt fractions produced at the top of a cold melting regime. *Journal of Petrology, 48(4),* pp. 647-660.

Dvorak, J.J., and Dzurisin, D. (1997). Volcano geodesy; the search for magma reservoirs and the formation of eruptive vents. *Reviews of Geophysics, 35(3),* pp. 343-384.

Eichelberger, J.C., and Izbekov, P.E. (2000). Eruption of andesite triggered by dyke injection; contrasting cases at Karymsky volcano, Kamchatka and Mt Katmai, Alaska. *Philosophical Transactions - Royal Society of Mathematical, Physical and Engineering Sciences, 358,* pp. 1465-1485.

Faure, G., and Mensing, T.M. (2005). Isotopes. *Principles and Applications*, pp. 897.

Ferlito, C., Viccaro, M., Nicotra, E., and Cristofolini, R. (2012). Regimes of magma recharge and their control on the eruptive behaviour during the period 2001-2005 at Mt. Etna volcano. *Bulletin of Volcanology, 74(2),* pp. 533-543.

Fowler, S.J., & Spera, F.J. (2008). Phase equilibria trigger for explosive volcanic eruptions. *Geophysical Research Letters, 35*(8).

Fowler, S., Bohrson,W., and Spera, F.J. (2004) Magmatic Evolution of the Skye Igneous Centre, Western Scotland: Modelling of Assimilation, Recharge and Fractional Crystallization. *Journal of Petrology,45(12),* pp. 2481-2505.

Francis, D. (1986). They pyroxene paradox in MORB glasses – a signature of picritic parental magmas? *Letters to Nature, 319*, pp. 586-589.

Gale, A., Dalton, C.A., Langmuir, C.H., Su, Y., and Schilling, J.G. (2013). The mean composition of ocean ridge basalts. *Geochemistry, Geophysics, Geosystems, 14(3),* pp. 489-518.

Ghiorso, M.S., Hirschmann, M.M., Reiners, P.W., and Kress, V.C. III (2002) The pMELTS: A new revision of MELTS aimed at improving calculation of phase relations and major element partitioning involved in partial melting of the mantle at pressures up to 3 GPa. Geochemistry, Geophysics, Geosystems **3**.

Harker, A. (1909). The natural history of igneous rocks. Macmillan, New York.

Kinzler, R.J., and Grove, T.L. (1992). Primary magmas of mid-ocean ridge basalts; 1, experiments and methods. *Journal of Geophysical Research, 97,* pp. 6885-6906.

Kovalenko, V.I., Kozlovsky, A.M., and Yarmolyuk, V.V. (2009) Trace element ratios as indicators of source mixing and magma differentiation of alkali granitoids and basites of the Haldzan-Buregtey massif and the Haldzan-Buregtey rare-metal deposit, Western Mongolia. *Petrologiya, 2009, 17(2),* pp. 175–196.

Juteau, M., Michard, A., and Albarede, F. (1986). The Pb-Sr-Nd isotope geochemistry of some recent circum-Mediterranean granites. *Contributions to Mineralogy and Petrology, 92*(3), pp. 331-340.

Lange, R.A., Cashman, K.V., and Navrotsky, A. (1994). Direct measurements of latent heat during crystallization and melting of a ugandite and an olivine basalt. *Contributions to Mineralogy and Petrology, 118*, pp. 169-181.

Langmuir, C.H., Vocke, R.D., Hanson, G.N., and Hart, S.R. (1978). A general mixing equation with applications to Icelandic basalts. *Earth and Planetary Science Letters, 37,* pp. 380-392.

Larson, L., Thomas, C., Eppinga, M., and Coulthard, T. (2014). Exploratory modelling: Extracting causality from complexity. *Eos, 95(32),* pp. 285-292.

Lee, C.A., and Bachmann, O. (2014). How important is the role of crystal fractionation in making intermediate magmas? Insights from Zr and P systematics. *Earth and Planetary Science Letters, 393,* pp. 266-274.

Lin, J., and Phipps Morgan, J. (1992). The spreading rate dependence of three-dimensional mid-ocean ridge gravity structure. *Geophysical Research Letters, 19*(1), pp. 13-16.

Maier, W.D., Arndt, N.T., and Curl, E.A. (2000). Progressive crustal contamination of the Bushveld Complex; evidence from Nd isotopic analyses of the cumulate rocks. *Contributions to Mineralogy and Petrology, 140(3),* pp. 316-327.

Marshall, L.A. and Sparks, R.S.J. (1984). Origin of some mixed-magma and net-veined ring intrusions. *Journal of the Geological Society, 141,* pp. 171-182.

Niu, Y., and O'Hara, M.J. (2006). MORB chemistry and ridge axial depth; a new interpretation. *Geochimica Et Cosmochimica Acta, 70*(18).

Niu, Y., and O'Hara, M.J. (2008). Global correlations of ocean ridge basalt chemistry with axial depth; a new perspective. *Journal of Petrology, 49*(4), pp. 633-664.

O'Hara, M.J. (1967). Mineral facies in ultrabasic rocks. In: Wyllie, P.J. (Ed.). *Ultramafic and Related Rocks*, pp. 7-18. J. Wiley, New York.

O'Hara, M.J. (1972). Upper mantle melting from the bottom-the source of magmatism and the driving force of global tectonics. *Earth Sciences Leeds, 8*, pp. 219-24.

O'Hara, M.J. (1977). Geochemical evolution during fractional crystallization of a periodically refilled magma chamber. *Nature, London, 266*, pp. 503-07.

O'Hara, M.J. and Mathews, R.E. (1981). Geochemical evolution in an advancing, periodically replenished, periodically tapped, continuously fractionated magma chamber. *Journal of the Geological Society of London, 138*, pp. 237-277.

Oldenburg, C.M., Spera, F.J., Yuen, D.A., and Sewell, G.H. (1989). Dynamic mixing in magma bodies; theory, simulations, and implications. *Journal of Geophysical Research, 94*, pp. 9215-9236.

Perugini, D., Poli, G, and Rocchi, S. (2005). Development of viscous fingering between mafic and felsic magmas: evidence from the Terra Nova Intrusive Complex (Antarctica). *Mineralogy and Petrology, 83*, pp. 151-166.

Perugini, D., and Poli, G. (2012). The mixing of magmas in plutonic and volcanic environments; analogies and differences. *Lithos (Oslo), 153*, pp. 261-277.

Rhodes, J.M., Dungan, M.A., Blanchard, D.P., and Long, P.E. (1979). Magma mixing at mid-ocean ridges: Evidence from basalts drilled near 22° N on the Mid-Atlantic Ridge. *Tectonophysics, 55*, pp. 35-61.

Schneider, J., Schmalzl, J., and Tei, T. (2007) Lagrangian avenues of transport in the Earth's mantle. *Chaos, 17*.

Sinton, J.M., Smaglik, S.M., Mahoney, J.J., and MacDonald, K.C. (1991). Magmatic processes at superfast spreading mid-ocean ridges; glass compositional variations along the east pacific rise 13 degrees -23 degrees S. *Journal of Geophysical Research, 96*, 6133-6155.

Slezin, Y.B. (2003) The mechanism of volcanic eruptions (a steady state approach*). Journal of Volcanology and Geothermal Research, 122*, pp. 7-50.

Snyder, D. (2000) Thermal effects of the intrusion of basaltic magma into a more silicic magma chamber and implications for eruption triggering. *Earth and Planetary Science Letters, 175*, pp. 257-273.

Sparks, R.S.J., and Marshall, L.A. (1985) Thermal and mechanical constraints on mixing between mafic and silicic magmas. *Journal of Volcanology and Geothermal Research, 29*, pp. 99-124.

Spera, F.J., *Encyclopedia of Volcanoes, H. Sigurdsson, Ed*. Academic Press: New York, 2000.

Spera, F.J., and Bohrson,W. (2004). Open-System Magma Chamber Evolution: an Energy-constrained Geochemical Model Incorporating the Effects of Concurrent Eruption, Recharge, Variable Assimilation and Fractional Crystallization . *Journal of Petrology, 45(12),* pp.2459-2480.

Spera, F.J., and Bohrson, W.A., Till, C.B., Ghiorso, M.S., (2007), Partitioning of trace elements among coexisting crystals, melt, and supercritial fluid during isobaric crystallization and melting. *American Mineralogist, 92*, pp.1881-1898.

Spera, F.J. (2011). Book Review: Diffusion in Minerals and Melts. Youxue Zhang and Daniele J. Cherniak, Editors. (2010) Reviews in Mineralogy and Geochemistry, vol. 72, 1038 pages, American Mineralogist, 96, p.1422

Spera, F., Schmidt, J., Bohrson, W. (2015 – accepted, *in press*). Dynamics and thermochemistry of magma mixing and hybridization with simultaneous fractional crystallization: A toy model with insights into natural systems. *American Mineralogist.*

Steiger, R.H. and Wasserburg, G.J. (1966). Systematics in the Pb^{208}-Th^{232}, Pb^{207}-U^{235}, Pb^{206}-U^{238} systems. *Journal of Geophysical Research, 71,* pp. 6065-6090.

Turner, M.B., Cronin, S.J., Smith, I.E., Stewart, R.B., and Neall, V.E. (2008). Eruption episodes and magma recharge events in andesitic systems; Mt. Taranaki, New Zealand. *Journal of Volcanology and Geothermal Research, 177(4),* pp. 1063-1076.

Varne, R., Brown, A.V., and Falloon, T. (2000). Macquarie island; its geology, structural history, and the timing and tectonic setting of its N-MORB to E-MORB magmatism. *Special Paper - Geological Society of America, 349,* pp. 301-320.

Vollmer, R. (1976). Rb-Sr and U-Th-Pb systematics of alkaline rocks: the alkaline rocks from Italy. Geochimica et Cosmochimica Acta, 40, pp. 283-295.

Walker, D., Shibata, T., and DeLong, S. (1979). Abyssal tholeiites from the Oceanographer Fracture Zone. *Contributions to Mineral Petrolology, 70,* pp. 111-125.

Waters, C.L., Sims, K.W.W., Perfit, M R., Blichert-Toft, J., and Blusztajn, J. (2011). Perspective on the genesis of E-MORB from chemical and isotopic heterogeneity at 9-10 degree N east pacific rise. *Journal of Petrology, 52*(3), pp. 565-602.

White, S.M., Crisp, J.A., and Spera, F.J. (2006). Long-Term Volumetric Eruption Rates and Magma Budgets. *Geochemistry, Geophysics, Geosystems, 7*(1).

Wolff, J.A., and Ramos, F.C. (2013) Processes in caldera-forming high-silica rhyolite magma: Rb-Sr and Pb isotope systematics of the Otowi Member of the Bandelier Tuff, Valles Caldera, New Mexico, USA. *Journal of Petrology.*

Workman, R.K. and Hart, S.R. (2005). Major and trace element composition of the depleted MORB mantle (DMM). *Earth and Planetary Science Letters*, *231*, pp. 53-72.

Zhang, C., Juergen, K., Clemens, K., Niko, G., and Behrens, H. (2014). Rapid hydrothermal cooling above the axial melt lens at fast-spreading mid-ocean ridge. *Scientific Reports*, *6342(4)*.

7. FIGURES LEGEND

Figure 1 – Topology of the isobaric binary eutectic system of the toy model based upon the thermodynamic parameter values for $CaMgSi_2O_6$ - $CaAl_2Si_2O_8$ at 1 bar

Figure 2 – A schematic representation of toy model initial conditions and hybrid solution overlain on the binary eutectic phase diagram for $CaMgSi_2O_6$ - $CaAl_2Si_2O_8$ at 1 bar

Figure 3 – Enthalpy vs. temperature in an isobaric system for a fixed composition

Figure 4 – Example of an invariant point outcome, also used as an illustration of the 'Thermodynamic Attractor' phenomenon discussed in section 4.1

Figure 5a – Example of the anomalous thermal effect where the result is a hybrid *magma* whose temperature is less than both the initial temperatures of **M** and **R**

Figure 5b – Example of the anomalous thermal effect where the result is a hybrid *melt* whose temperature is less than both the initial temperatures of **M** and **R**

Figure 6a – Example of hybridization following reaction with a β-rich stoped block

Figure 6b – Example of hybridization following reaction with an α-rich stoped block

Figure 7 – Example of hybridization following reaction with a *cold* α-rich stoped block; stoped block is half the temperature (650K colder) than identical hybridization scenario depicted in Figure 6b

Figure 8 – Example of diabatic (RFC) hybridization resulting in a wholly crystalline final state

Figure 9 – Example of the cessation of crystallization and complete resorption of a previously precipitating phase; in this example the hybridization of α-saturated **M** magma with a β-saturated **R** magma results in an **H** magma that has no α crystals. Also note the strong thermal anomaly in this example

Figure 10 – Serial application following the geochemical evolution of an initially aphyric magma **M** that undergoes fractional crystallization, precipitates clinopyroxene followed by settling of the cpx crystals (physical separation). The residual melt then hybridizes with a recharge magma **R**. The resulting hybrid magma **H** undergoes fractional crystallization, precipitating plagioclase. This 3-part process is referred to as FC-R-FC

Figure 11a – The trace element 'Dilution Effect'. The concentration of Eu in the melt phase of **H** is less than its concentration in both starting magma melts **M** and **R**. In this example the concentration in the hybrid melt ($C^{H\ell}$) for Eu is lower than in both **M** and **R** melts ($C^{M\ell}$ and $C^{R\ell}$, respectively). A dashed green line illustrates the phase mixing line between solid (α crystals) and melt for **H** magma. The red dot-dash line illustrates the phase mixing line between solid (α crystals) and melt for **M** magma. The blue dotted line illustrates the phase mixing line between solid (β crystals) and melt for **R** magma. The solid black line illustrates the bulk composition mixing line **M**+**R** = **H**

Figure 11b – Expansion of phase hyperbolas when the trace element ratio is such that the ratio of their partition coefficients is not unity. In this example C1 = Eu, C2 = Sr, C3 = Y and C4 = V. The data is the same used to generate Figure 11a. A dashed green line illustrates the phase mixing line between solid (α crystals) and melt for **H** magma. The red dot-dash line illustrates the phase mixing line between solid (α crystals) and melt for **M** magma. The blue dotted line illustrates the phase mixing line between solid (β crystals) and melt for **R** magma. The solid black line illustrates the bulk composition mixing line **M**+**R** = **H**

Figure 11c, 11d: Linear companion plots for the data used to generate Figure 11b. A dashed green line illustrates the phase mixing line between solid (α crystals) and melt for **H** magma. The red dot-dash line illustrates the phase mixing line between solid (α crystals) and melt for **M** magma. The blue dotted line illustrates the phase mixing line between solid (β crystals) and melt for **R** magma. The solid black line illustrates the bulk composition mixing line **M**+**R** = **H**

Figure 12 – Trace element ratio-ratio plot depicting the concurrent evolution of bulk and melt compositions across serial recharge events**.** Hybrid magma **H** melt composition depicted by green circles. **H** bulk composition depicted by orange triangles.

Figure 13a – MCS major oxide ratio-ratio plot of two related R-Hybridization events (**H1**, **H2**) resulting from different mixing ratios of identical **M** and **R**. Solid blue line is mixture curve representing bulk composition of **M**+**R** = **H1**, **H2**. Red dashed line is resident magma **M** phase hyperbola. Green dotted line is hybrid magma **H1** phase hyperbola. Green dash-dot line is hybrid magma **H2** phase hyperbola. Recharge magma **R**, denoted by a blue triangle, is 100% melt and therefore has no phase hyperbola.

Figure 13b – Companion plot for Figure 13a. Note that in companion plot space mixing is confirmed by the observation of linear relationships.

Figure 14a – MCS major oxide ratio-ratio plot of two related R-Hybridization events (**H1**, **H2**) resulting from different mixing ratios of identical **M** and **R** similar to Figure 13a except that equilibrium cpx has been removed from **H2** resulting in a phase hyperbola that no longer passes through the bulk composition of **H2** located on the **M**+**R** mixture hyperbola. Red dashed line is resident magma **M** phase hyperbola. Green dotted line is hybrid magma **H1** phase hyperbola. Green dash-dot line is hybrid magma **H2** phase hyperbola. Recharge magma **R**, denoted by blue triangle, is 100% melt and therefore has no phase hyperbola

Figure 14b – Companion plot for Figure 14a. Note that in companion plot space mixing is confirmed by the observation of linear relationships, however in this case a linear trend is not possible for **H2** because the bulk solids, having had cpx removed, no longer agree with the bulk composition of **H2**

Figure 15 – Cartoon illustrating the R-FC-A-E magma chamber experimental design. An aphyric **M** is isenthalpically hybridized with an aphyric **R** and any resultant crystals are removed (*R*). The remaining hybrid **H** melt has enthalpy removed using the Φ parameter (see text) stimulating fractional crystallization (*FC*). FC crystals are removed and the remaining **H** melt is mixed with a subsolidus mass of wallrock and allowed to equilibrate (*A*). Any resultant crystals are removed and the remaining melt is partially erupted (*E*). The remaining melt after eruption becomes the **M** for the next RFCAE cycle

Figure 16 – Relative (non-dimensional) size (mass) comparison of the evolution of waxing, waning, and steady state RFCAE magma chambers

Figure 17a – Relative (non-dimensional) temperature $\overline{T}$ (see text) comparison of the evolution of a waxing, waning, and steady state RFCAE magma chamber**.** Note that the waning and steady state chamber types get stuck at the invariant point ($\overline{T} = 0$)

Figure 17b – Relative (non-dimensional) major element composition $\overline{X}$ (see text) comparison of the evolution of a waxing, waning, and steady state RFCAE magma chamber. Note that the waning and steady state chamber types get stuck at the invariant point ($\overline{X} = 0$)

Figure 18 – Comparison of the trace element geochemical evolution of a waxing, waning, and steady state RFCAE magma chamber viewed in ratio-ratio space. Points represent 10 RFCAE cycles and are labeled 1 for the initial cycle and 10 for the final (most evolved) cycle

Figure 19 – Comparison of the $^{87}Sr/^{86}Sr$ geochemical evolution of a waxing, waning, and steady state RFCAE magma chambers with initial magma $\mathbf{M_o}$, recharge magma **R** and wallrock assimilant **A** plotted for reference of initial values

8. FIGURES

Figure 1 – Binary Eutectic Topology

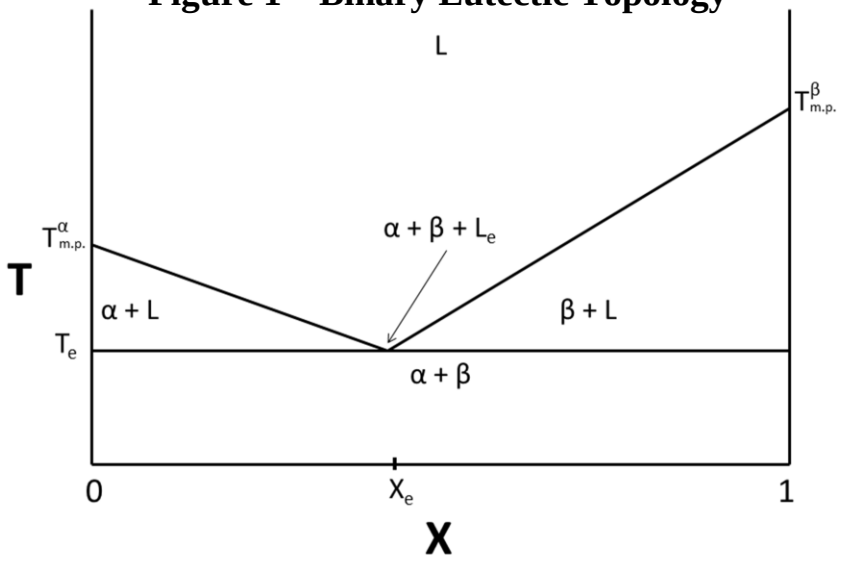

Figure 2 – Schematic Toy Model Initial and Final States

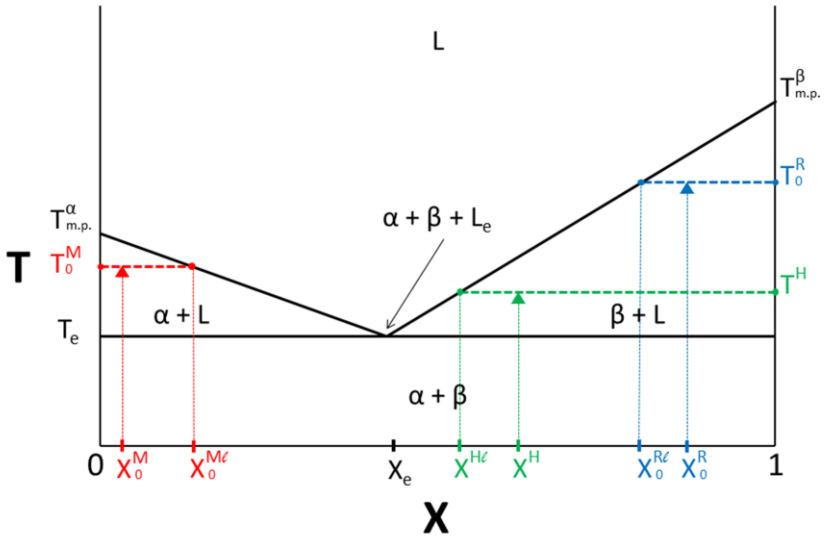

Figure 3 – Isobaric Enthalpy vs Temperature

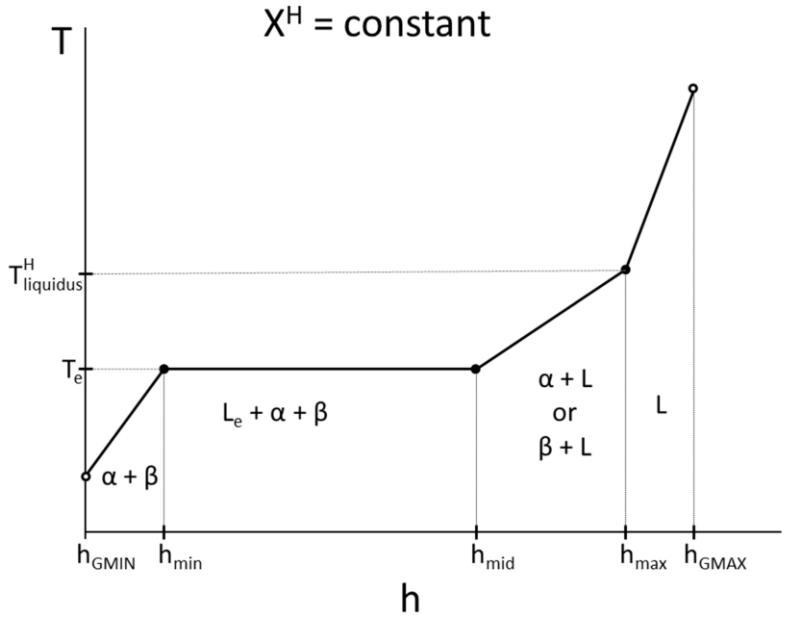

Figure 4 – Example Invariant Point Solution

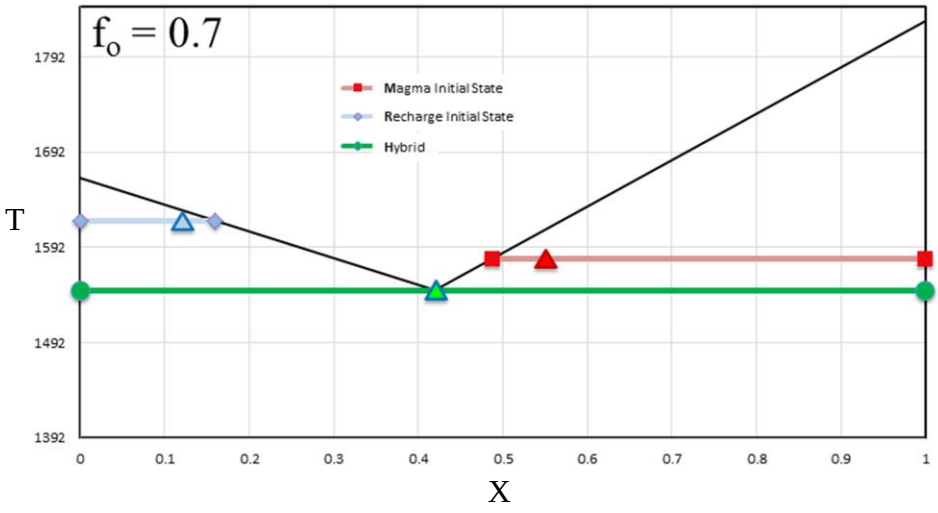

Figure 5a – Anomalous Thermal Effect Example

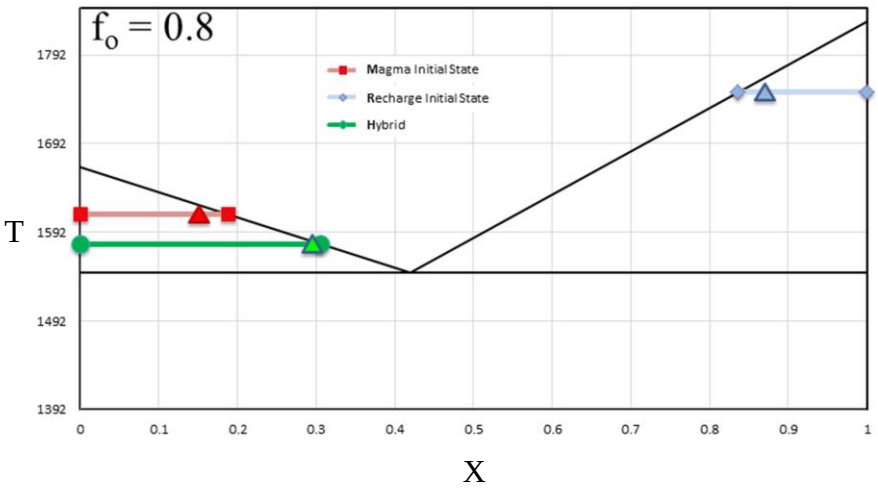

Figure 5b – Anomalous Thermal Effect Example

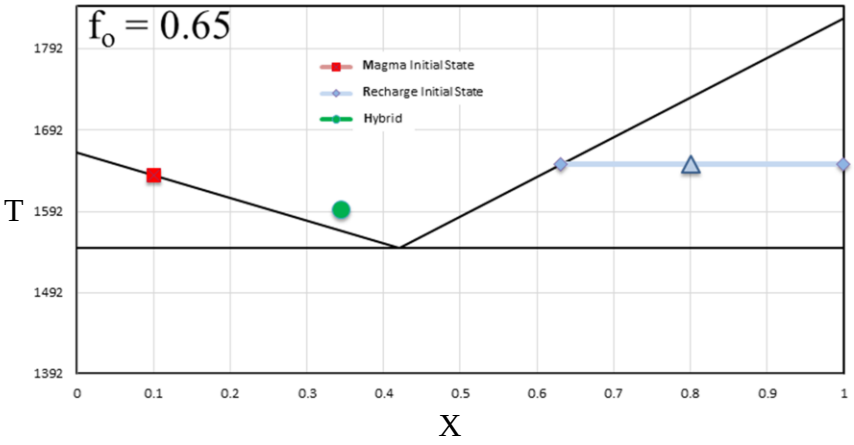

Figure 6a – Digestion of β-rich Stoped Block

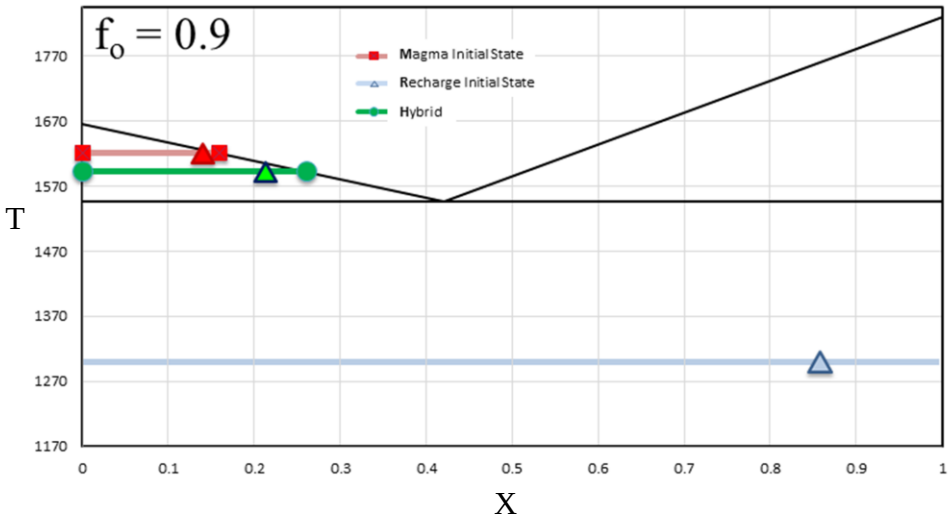

Figure 6b – Digestion of α-rich Stoped Block

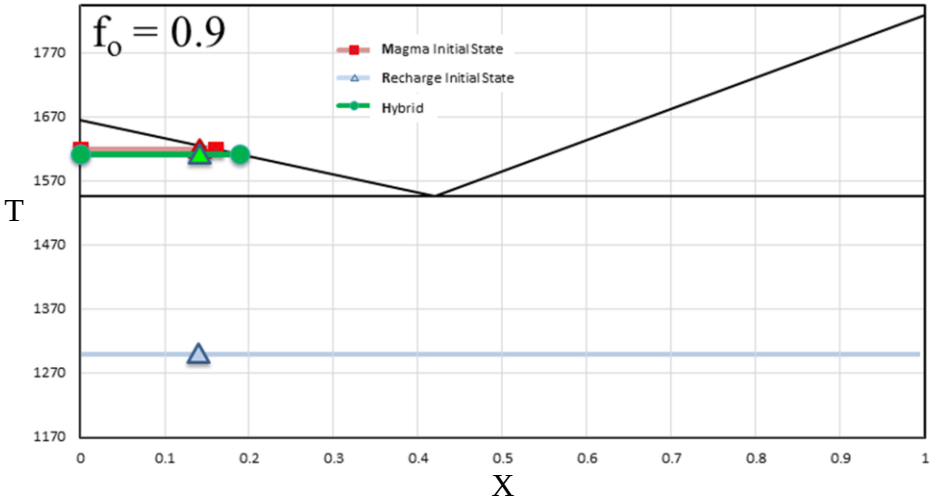

Figure 7 – Digestion of Cold α-rich Stoped Block

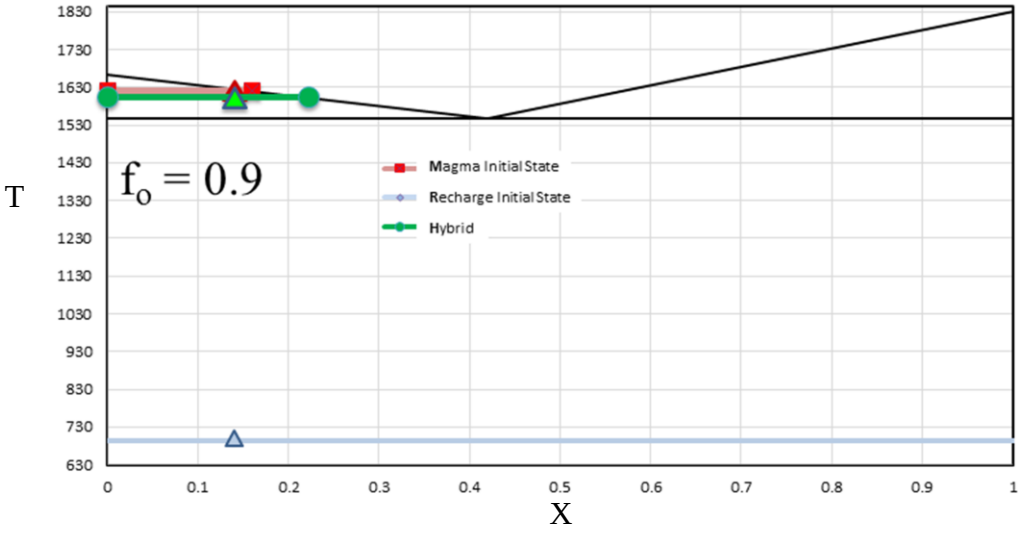

Figure 8 – Diabatic (RFC) Hybridization

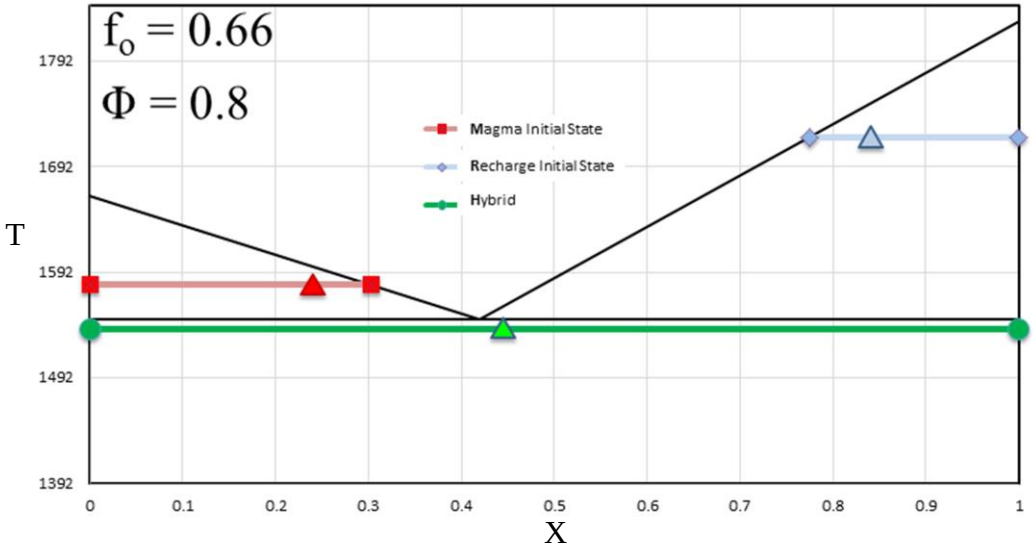

Figure 9 – Cessation of α Crystallization

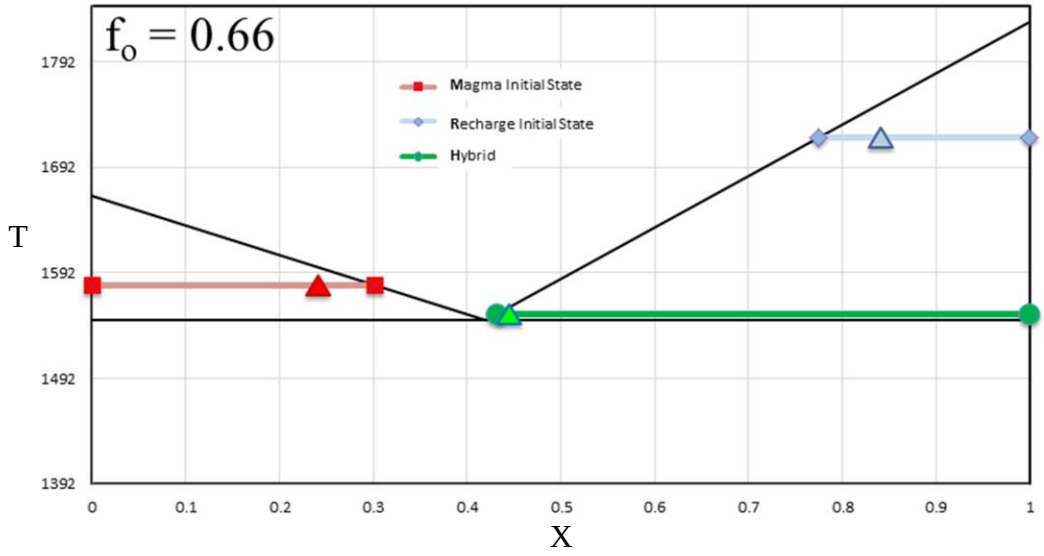

Figure 10 – FC–R-Hybridization–FC

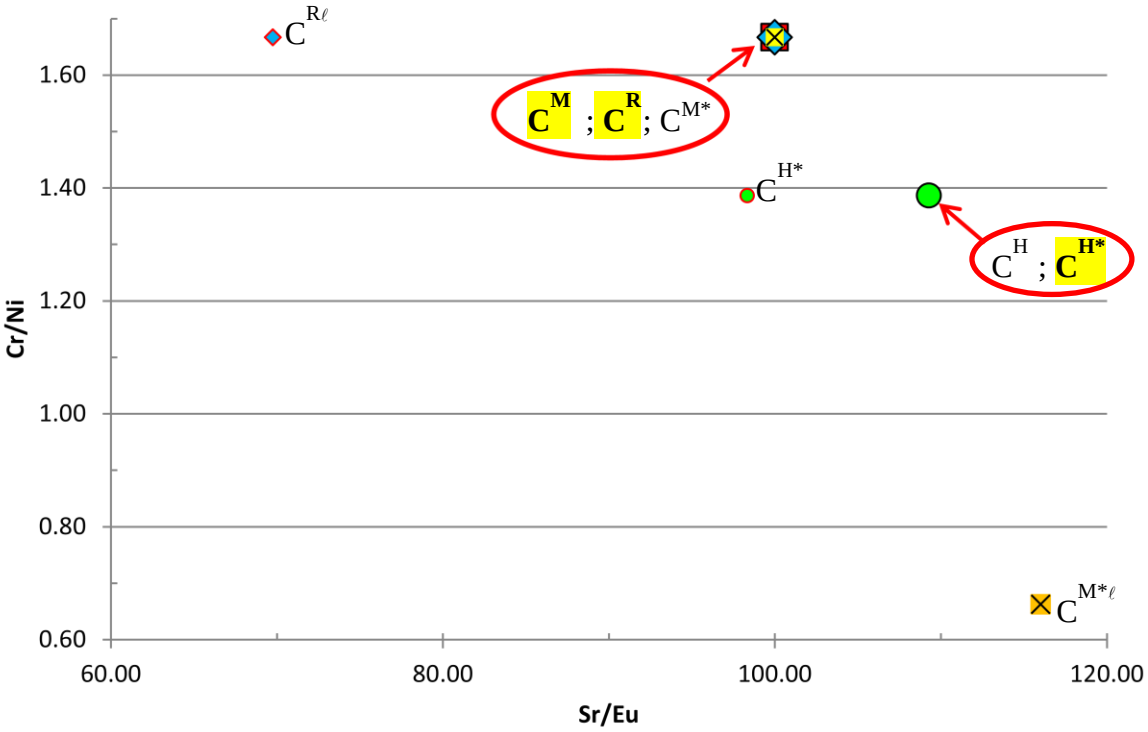

Figure 11a - Dilution of Eu in H Melt after M+R Hybridization

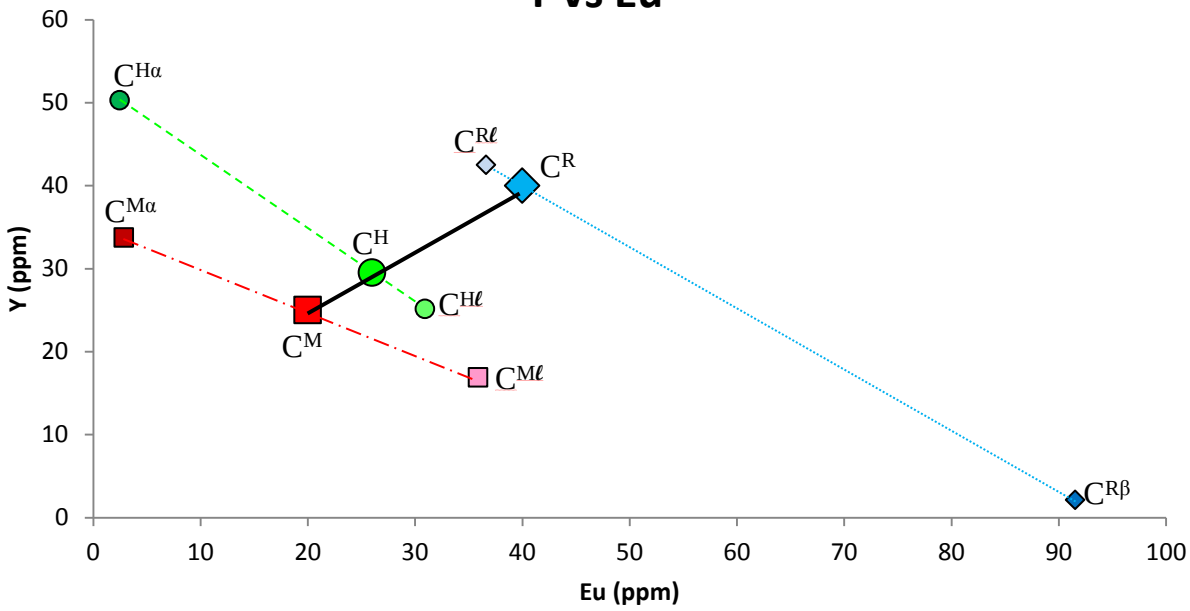

Figure 11b – Mixture and Phase Hyperbolas, K Ratio ≠ 1

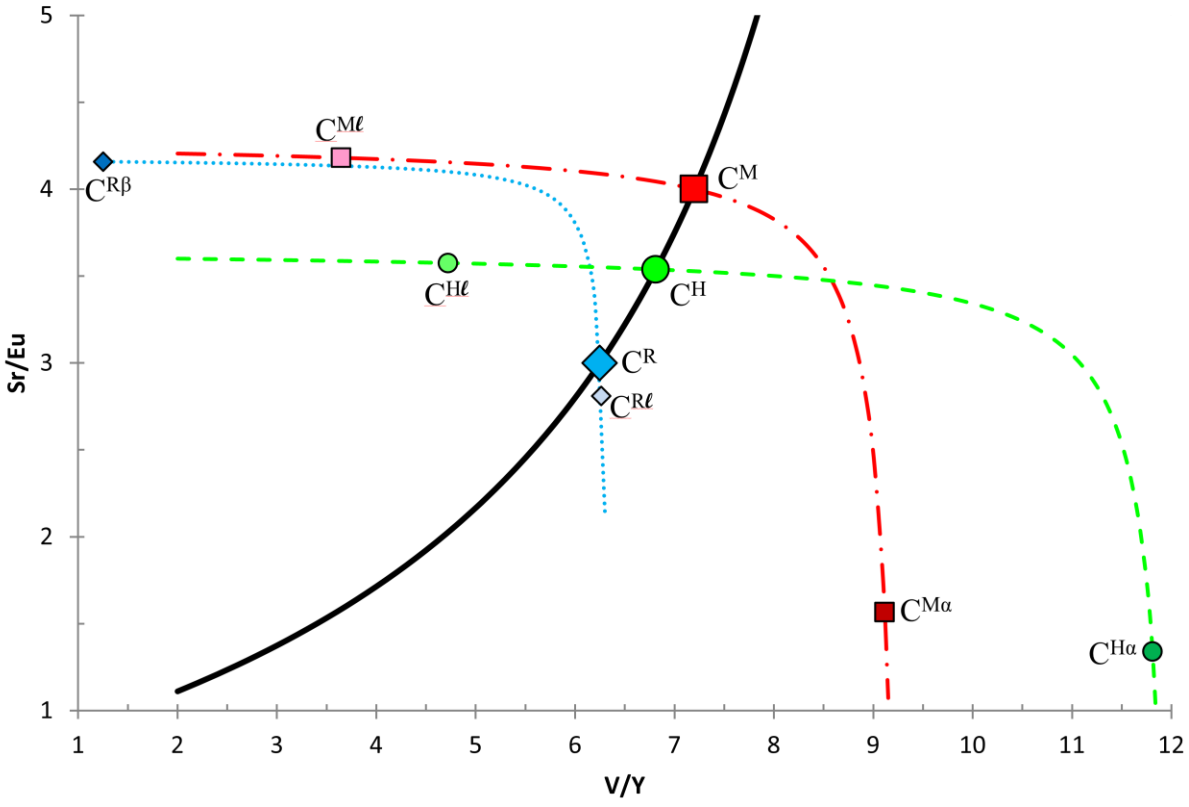

Figure 11c – Companion Plot 1 for Figure 11b

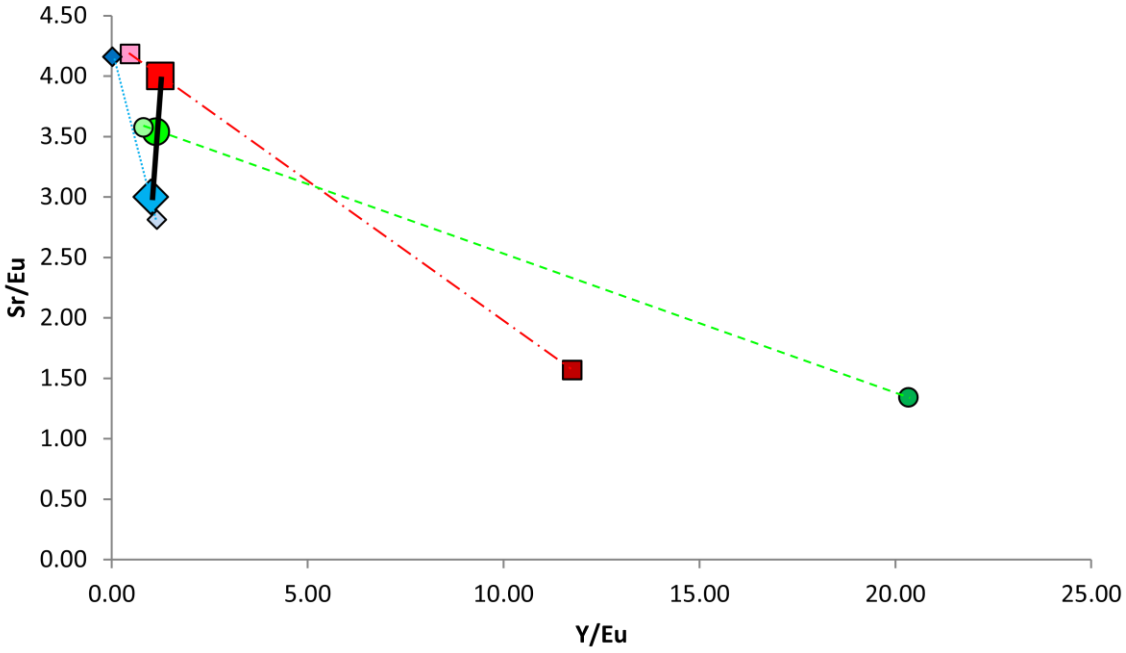

Figure 11d – Companion Plot 2 for Figure 11b

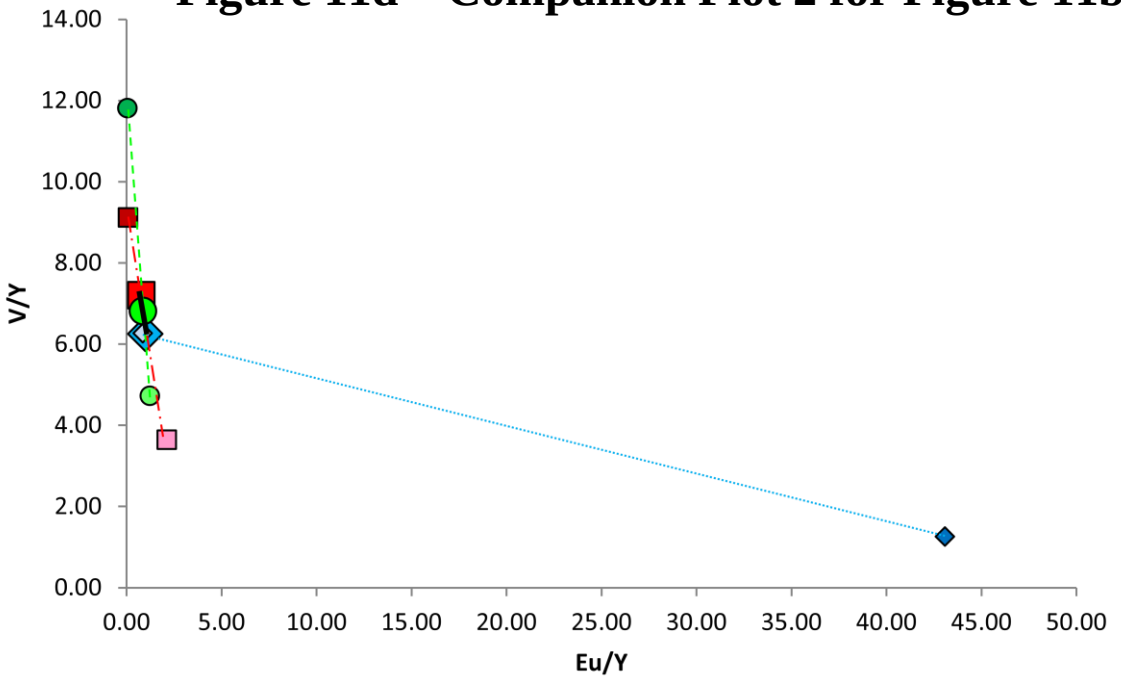

Figure 12 – (V/La) vs (Sr/Y) Evolution of Bulk Composition and Melt Composition

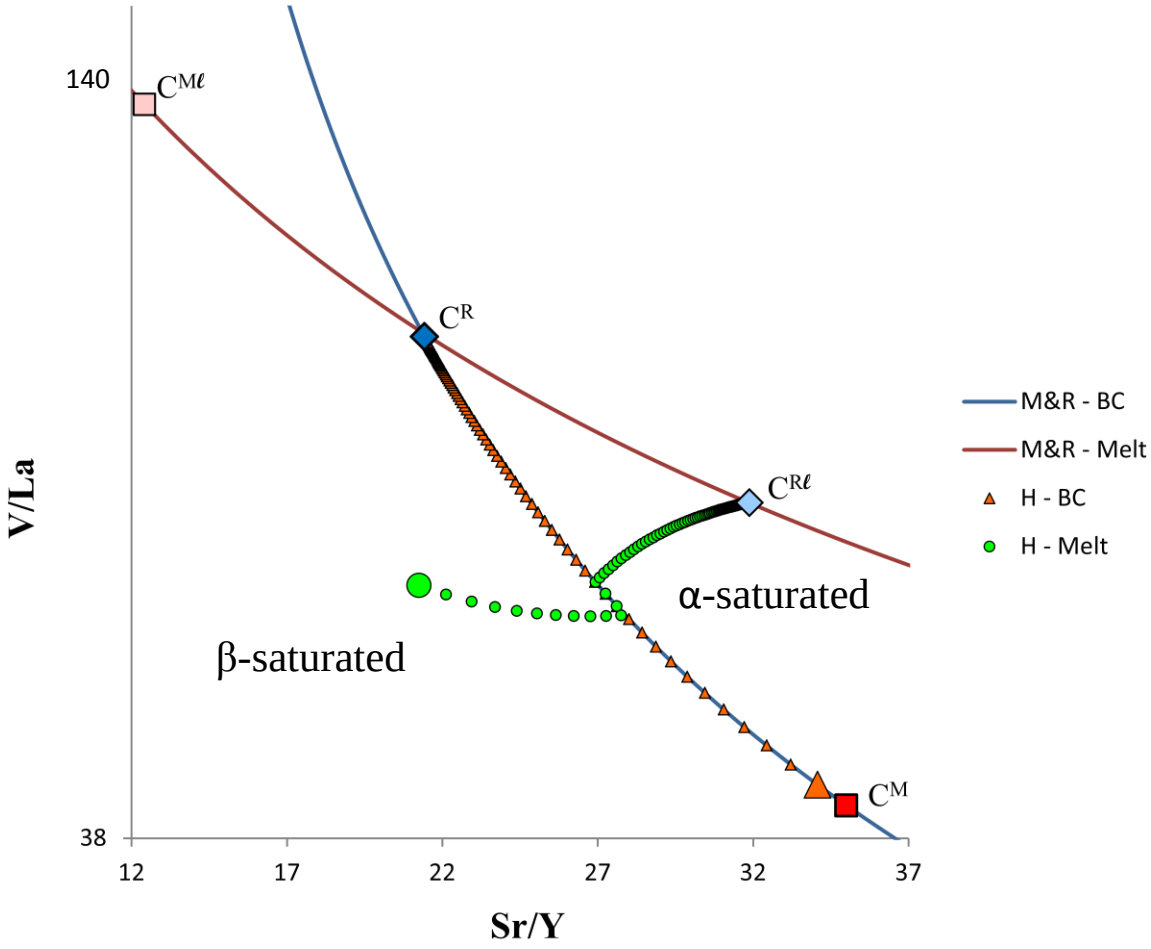

Figure 13a – MCS Major Oxide Mixture and Phase Hyperbolas

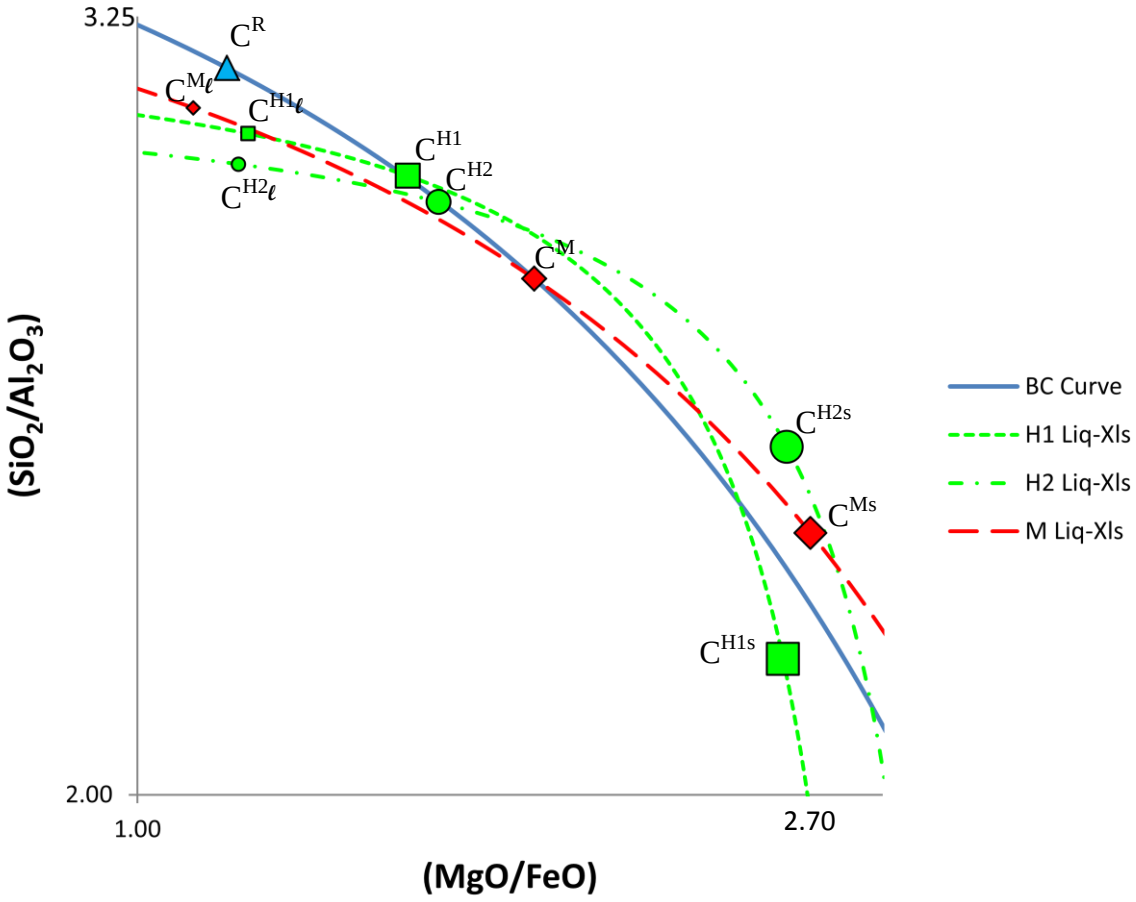

Figure 13b – Companion Plot for Figure 13a

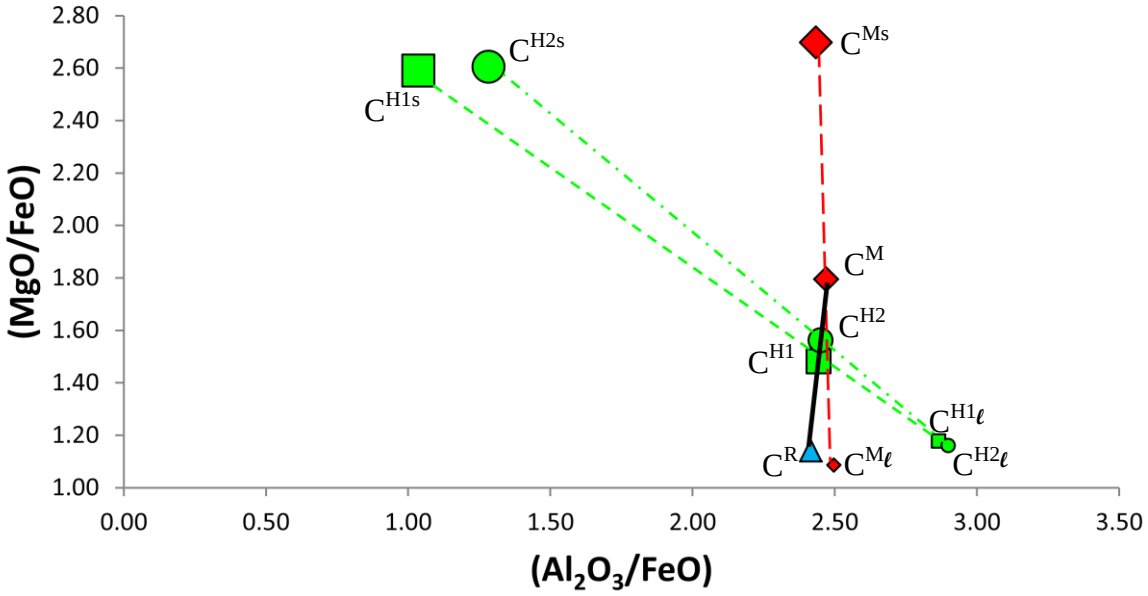

Figure 14a – MCS Major Oxide Mixture and Phase Hyperbolas; H2 Missing cpx

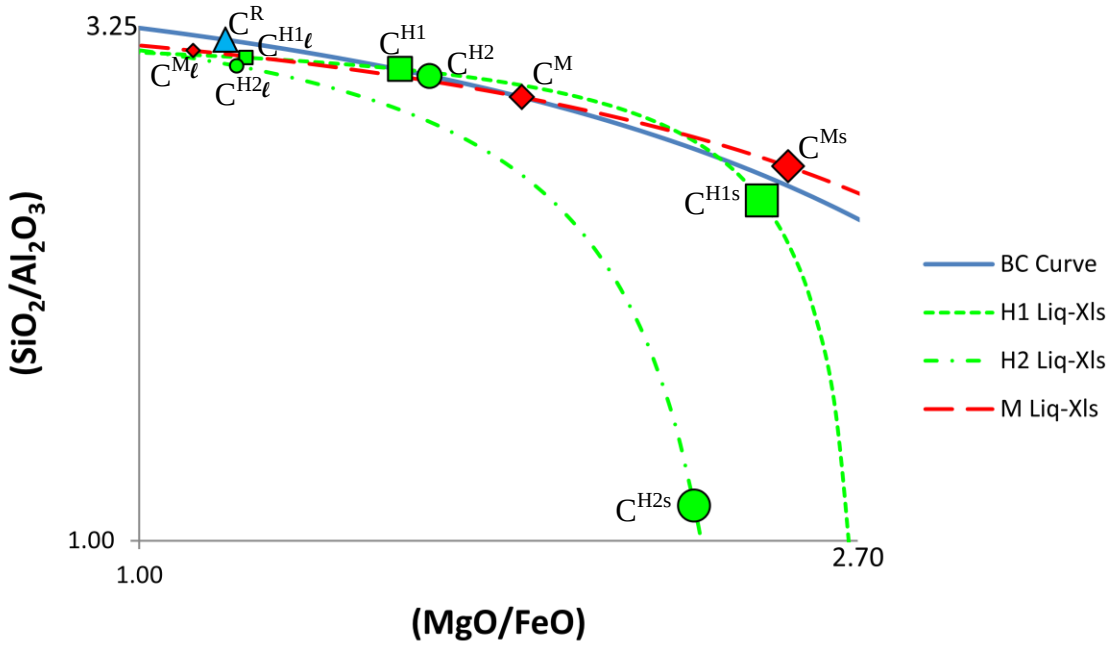

Figure 14b – Companion Plot for Figure 14a

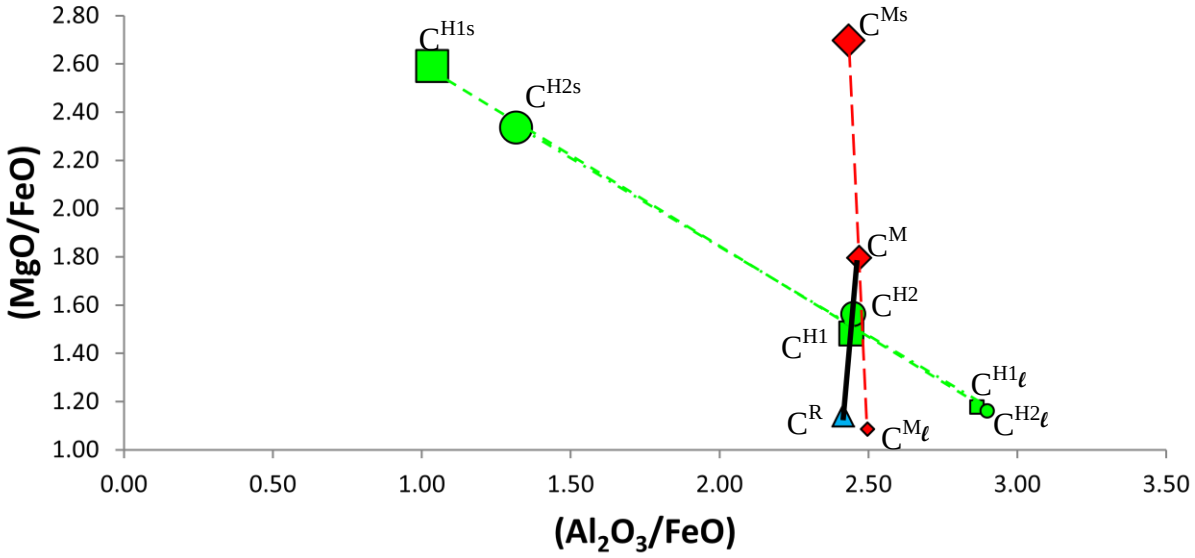

Figure 15 – The RFCAE Cycle

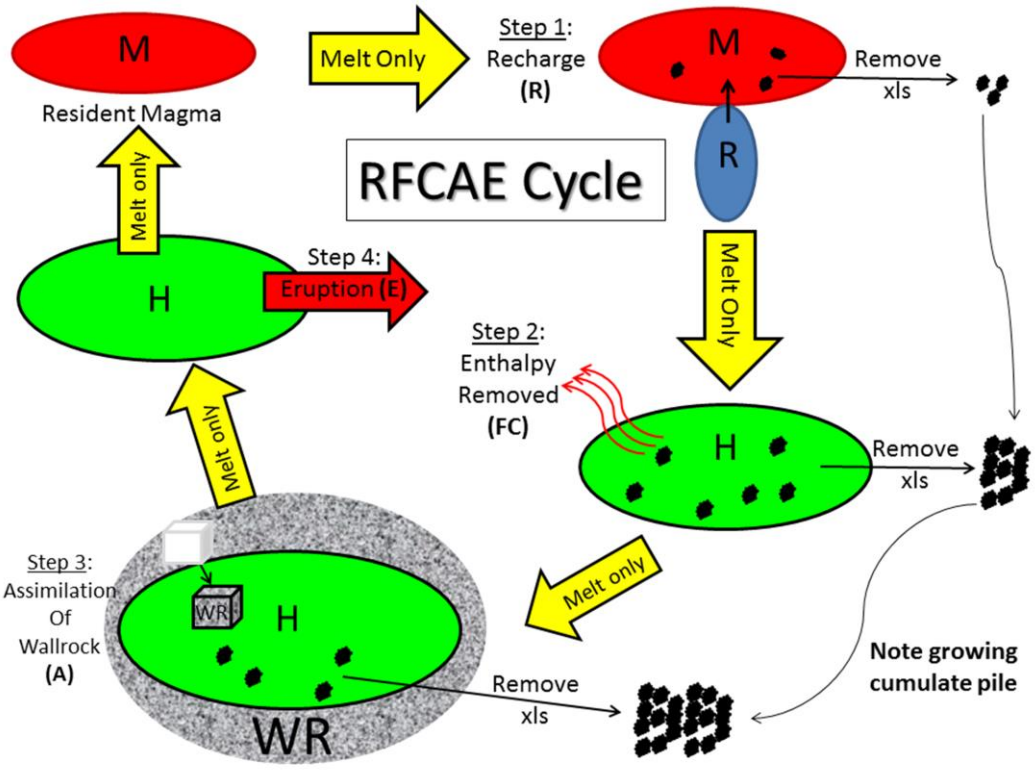

Figure 16 – RFCAE Magma Chamber Relative Size Comparison

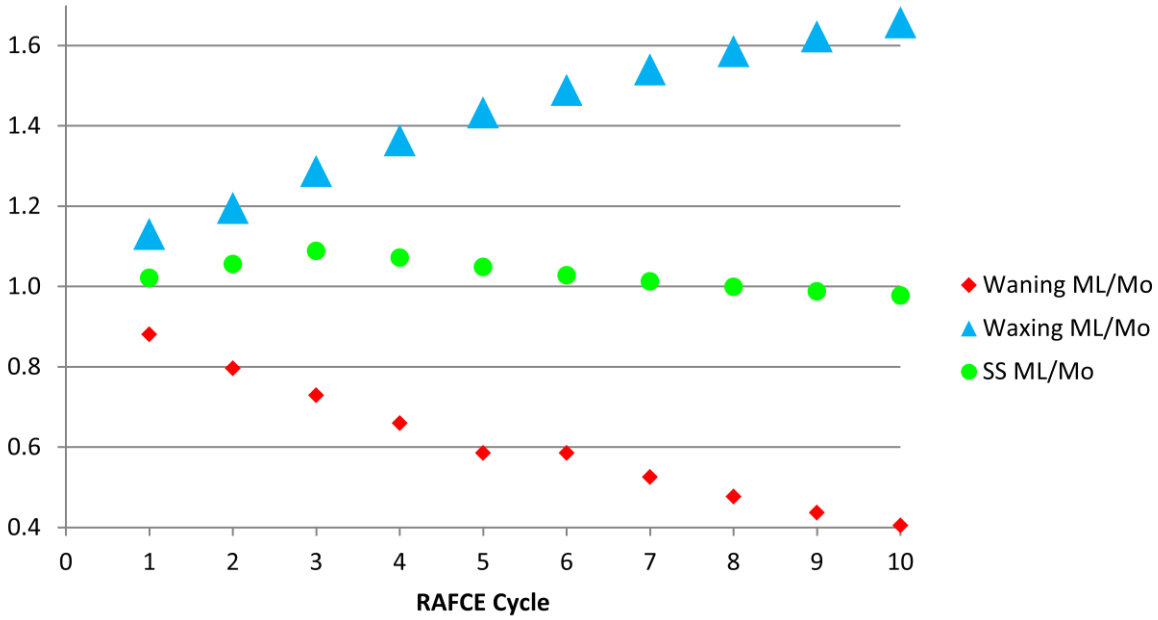

Figure 17a – Temperature Evolution of RFCAE Magma Chambers

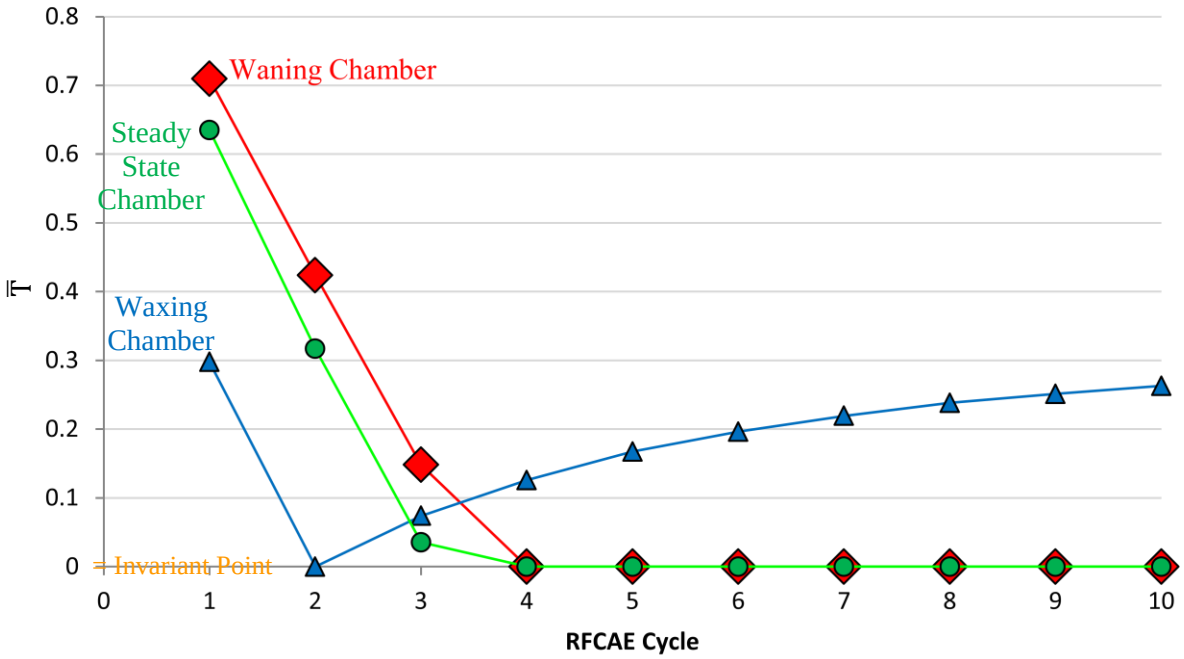

Figure 17b – Major Element Composition Evolution of RFCAE Magma Chambers

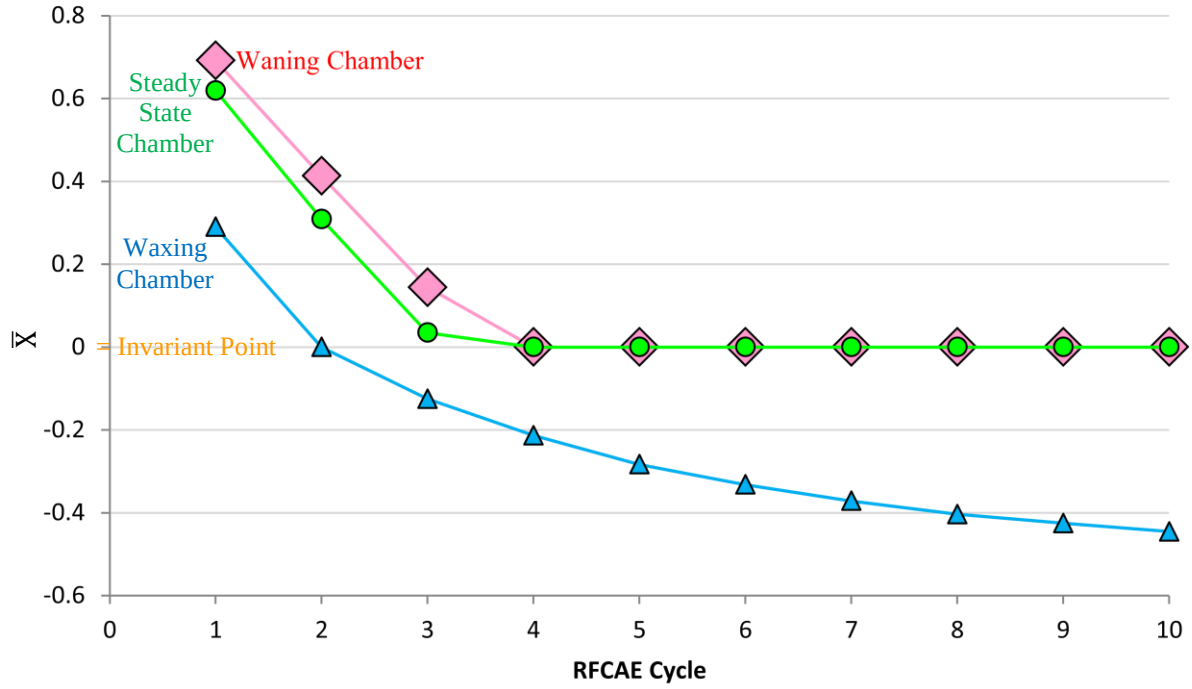

Figure 18 – Geochemical Evolution of RFCAE Magma Chambers

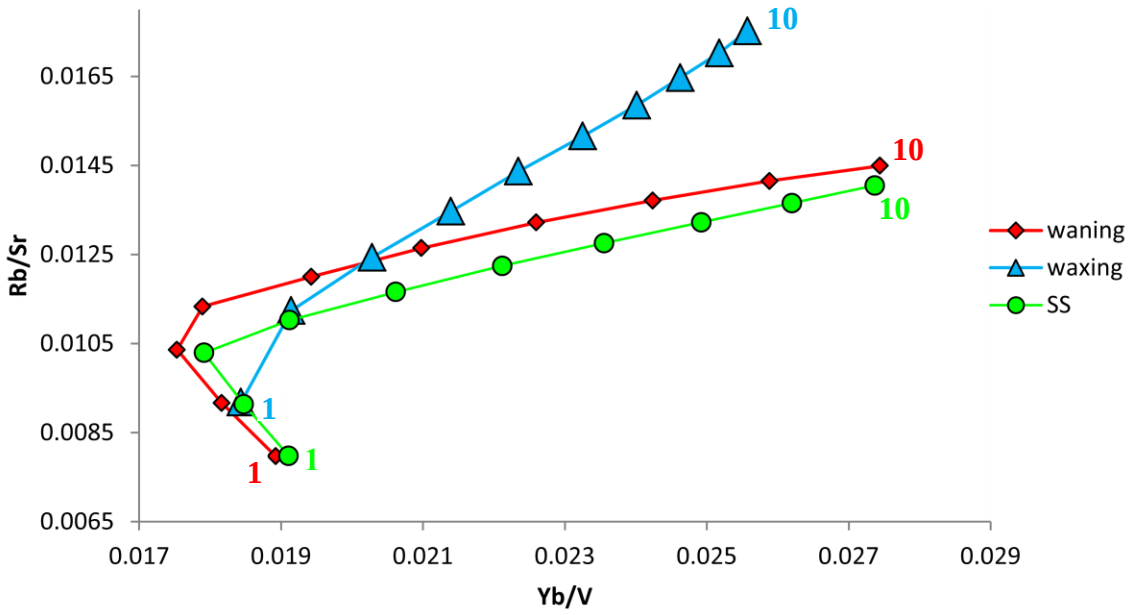

Figure 19 – $^{87}Sr/^{86}Sr$ Evolution of RFCAE Magma Chambers

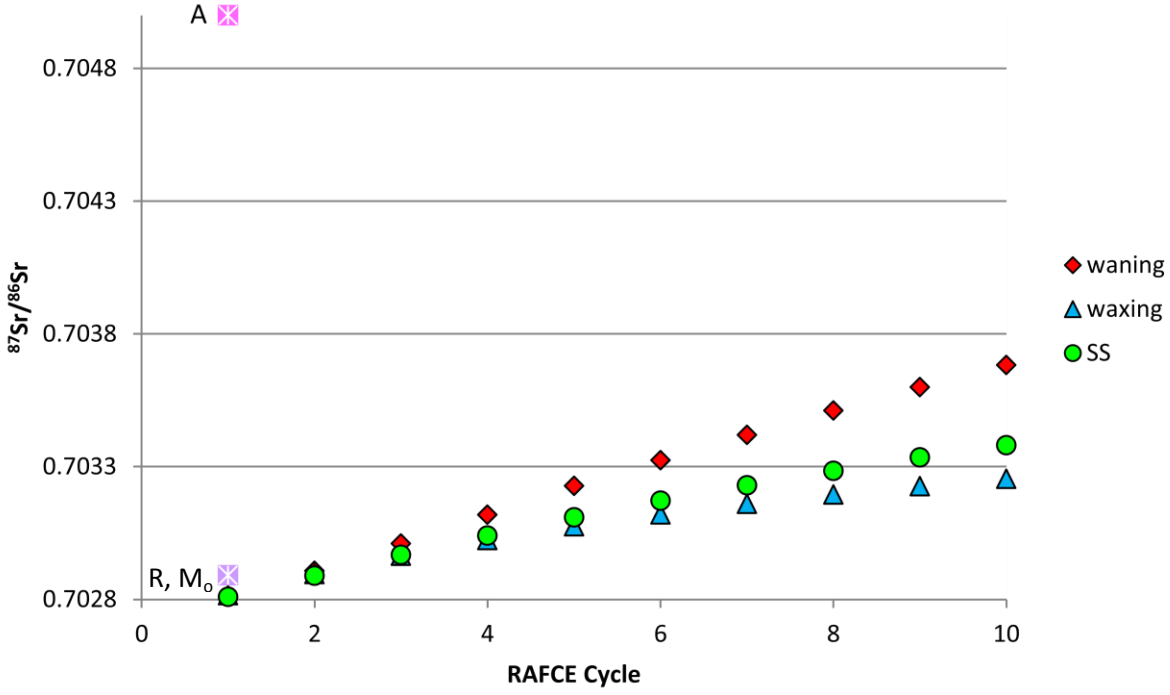

9. TABLES

Table 1 – MCS calculation of R-hybridization with Anomalous Thermal Effect

	M (f_o = 0.53)		**R**	**H**	
Phases (modal %)	melt (55.7), cpx (16.9), plag (10.3), ol (7.5), spl (9.5)		melt + trace ol	melt (87.2), cpx (1.9), ol (6.0), spl (5.0)	
T (°C)	1180		1179.2	1152.5	
Compositions (wt %):	$bulk^M$	$melt^M$	$melt^R$	$bulk^H$	$melt^H$
SiO_2	45.3	51.2	52.0	48.4	51.6
TiO_2	0.9	1.3	0.6	0.8	0.8
Al_2O_3	16.4	16.7	16.5	16.3	17.1
Fe_2O_3	1.3	0.5	1.3	1.3	0.7
Cr_2O_3	2.8	0.05	0	1.5	0.07
FeO	6.6	6.7	6.8	6.7	6.0
MgO	11.9	7.2	7.7	10.0	7.0
CaO	11.6	11.5	9.8	10.7	11.8
Na_2O	2.5	3.9	2.3	2.4	2.7
K_2O	0.1	0.2	0.4	0.2	0.3
P_2O_5	0.1	0.2	0	0.05	0.06
H_2O	0.3	0.6	2.6	1.4	1.6

Table 2 – FC-R-FC Physical and Geochemical Summary

	T (K)	w_ℓ	w_α	w_β	X		Cr		Ni		Sr		Eu	
					BC	Liq	BC	Liq	BC	Liq	BC	Liq	BC	Liq
M	1620	1	0	0	.16	.16	250	250	150	150	100	100	1	1
M^*	1605.9	.76	.24	0	.16	.21	250	31.5	150	47.6	100	131.4	1.0	1.13
$M^{*\ell}$	1606	1	0	0	.21	.21	31.5	31.5	47.6	47.6	131.4	131.4	1.13	1.13
R	1670	.76	0	.24	.75	.672	250	327.9	150	196.7	100	55.3	1.0	.79
H	1605	1	0	0	.453	.453	129.8	129.8	93.7	93.7	117.3	117.3	1.07	1.07
H^*	1548.9	.95	0	.05	.453	.424	129.8	136.8	93.7	98.7	117.3	99.9	1.07	1.03

Table 3 – FC-R-FC Trace Element Ratio Summary

	Cr/Ni		Sr/Eu	
	BC	Liq	BC	Liq
M	1.67	1.67	100	100
M^*	1.67	0.66	100	116.02
$M^{*\ell}$	0.66	0.66	116.02	116.02
R	1.67	1.67	100	69.77
H	1.39	1.39	109.3	109.3
H^*	1.39	1.39	109.3	98.35

Table 4 – Partition Coefficients for FC-R-FC

	Cr	Ni	Sr	Eu
K_{Sr}^{α}	30	10	.0001	.51
K_{Sr}^{β}	.0001	.0001	4.4	2.1

Table 5 – Recharge (R) magma hybridization with Y and V

State of Recharge magma **R**		State of resident Magma **M**		State of Hybrid magma **H**		System Parameters	
Initial Temp (K)	1600	Initial Temp (K)	1620	Temp (K)	1590	mixing ratio f_o	0.85
Initial Bulk Composition **R**	0.75*	Initial Bulk Composition **M**	0.12*	Composition	0.21*	Isenthalpic (R-hybridization)	Φ=1
Mass Frac Melt	0.53	Mass Frac Melt	0.75	Mass Frac Melt	0.80	Partition coefficient: $K_{plg\ (Y)}$	0.01
Mass Frac α (cpx) NOT PRESENT	N/A	Mass Frac α (cpx)	0.25	Mass Frac α (cpx)	0.20	Partition coefficient $K_{cpx\ (Y)}$	2
Mass Frac β (plag)	0.47	Mass Frac β (plag) NOT PRESENT	N/A	Mass Frac β (plag) NOT PRESENT	N/A		
Bulk Y conc (ppm)	30	Bulk Y conc (ppm)	30	Bulk Y conc (ppm)	30		
Y conc in Melt (ppm)	56	Y conc in Melt (ppm)	24	Y conc in Melt (ppm)	25		
Y conc in α (cpx) NOT PRESENT	N/A	Y conc in α (cpx) (ppm)	48	Y conc in α (cpx) (ppm)	52		
Y conc in β (plag) (ppm)	0.6	Y conc in β (plag) NOT PRESENT	N/A	Y conc in β (plag) NOT PRESENT	N/A		
Bulk V conc (ppm)	250	Bulk V conc (ppm)	250	Bulk V conc (ppm)	250		
V conc in Melt (ppm)	467	V conc in Melt (ppm)	200	V conc in Melt (ppm)	209		
V conc in α (cpx) NOT PRESENT	N/A	V conc in α (cpx) (ppm)	400	V conc in α (cpx) (ppm)	418		
V conc in β (plag) (ppm)	4.7	V conc in β (plag) NOT PRESENT	N/A	V conc in β (plag) NOT PRESENT	N/A		

*mass fraction component B ($CaAl_2Si_2O_8$)

Table 6: Behavior of Ni and Sr after RFC-Hybridization

State of Recharge magma **R**		State of resident Magma **M**		State of Hybrid magma **H**		System Parameters	
Initial Temp (K)	1640	Initial Temp (K)	1630	Temp (K)	1551.9	mixing ratio f_o	0.66
Initial Bulk Composition **R**	0.7*	Initial Bulk Composition **M**	0.1*	Composition	0.304*	diabatic mixing (RFC)	Φ = 0.94
Mass Frac Melt	0.77	Mass Frac Melt	0.80	Mass Frac Melt	0.75	Partition coefficient $K_{plg\ (Ni)}$	0.01
Mass Frac β (plag)	0.23	Mass Frac α (cpx)	0.20	Mass Frac α (cpx)	0.25	Partition coefficient $K_{cpx\ (Ni)}$	2
Bulk Ni conc (ppm)	100	Bulk Ni conc (ppm)	100	Bulk Ni conc (ppm)	100	Partition coefficient $K_{plg\ (Sr)}$	2
Bulk Sr conc (ppm)	100	Bulk Sr conc (ppm)	100	Bulk Sr conc (ppm)	100	Partition coefficient $K_{cpx\ (Sr)}$	.01
Ni conc in Melt (ppm)	129.4	Ni conc in Melt (ppm)	83.5	Ni conc in Melt (ppm)	80.3		
Sr conc in Melt (ppm)	81.3	Sr conc in Melt (ppm)	124.3	Sr conc in Melt (ppm)	132.0		
Ni conc in β (plag) (ppm)	1.3	Ni conc in α (cpx) (ppm)	167.0	Ni conc in α (cpx) (ppm)	160.6		
Sr conc in β (plag) (ppm)	162.7	Sr conc in α (cpx) (ppm)	1.24	Sr conc in α (cpx) (ppm)	1.32		

*mass fraction component B ($CaAl_2Si_2O_8$)

Table 7 – Recharge (R) magma hybridization with V, Y, Sr and Eu; Eu 'Dilution Effect'

State of Recharge magma **R**		State of resident Magma **M**		State of Hybrid magma **H**		System Parameters	
Initial Temp (K)	1600	Initial Temp (K)	1700	Temp (K)	1560	mixing ratio f	0.7
Initial Bulk Composition **R**	0.12*	Initial Bulk Composition **M**	.75*	Composition	.309*	Isenthalpic (R-hybridization)	Φ=1
Mass Frac Melt	.52	Mass Frac Melt	.94	Mass Frac Melt	.83	Partition coefficient: $K_{plg\ (V)}$	.01
Mass Frac α (cpx) NOT PRESENT	.48	Mass Frac α (cpx)	0	Mass Frac α (cpx)	.17	Partition coefficient $K_{cpx\ (V)}$	5
Mass Frac β (plag)	0	Mass Frac β (plag)	.06	Mass Frac β (plag)	0	Partition coefficient: $K_{plg\ (Y)}$	.05
Bulk Eu conc (ppm)	20	Bulk Eu conc (ppm)	40	Bulk Eu conc (ppm)	26	Partition coefficient $K_{cpx\ (Y)}$	2
Eu conc in Melt (ppm)	35.9	Eu conc in Melt (ppm)	36.6	Eu conc in Melt (ppm)	30.9	Partition coefficient: $K_{plg\ (Sr)}$	3.7
Eu conc in α (cpx) (ppm)	2.9	Eu conc in α (cpx) (ppm)	N/A	Eu conc in α (cpx) (ppm)	2.5	Partition coefficient $K_{cpx\ (Sr)}$	.03
Eu conc in β (plag) (ppm)	N/A	Eu conc in β (plag) (ppm)	91.5	Eu conc in β (plag) (ppm)	N/A	Partition coefficient: $K_{plg\ (Eu)}$	2.5
Bulk Y conc (ppm)	25	Bulk Y conc (ppm)	40	Bulk Y conc (ppm)	29.5	Partition coefficient $K_{cpx\ (Eu)}$	.08
Y conc in Melt (ppm)	16.9	Y conc in Melt (ppm)	42.5	Y conc in Melt (ppm)	25.2		
Y conc in α (cpx) (ppm)	33.8	Y conc in α (cpx) (ppm)	N/A	Y conc in α (cpx) (ppm)	50.3		
Y conc in β (plag) (ppm)	N/A	Y conc in β (plag) (ppm)	2.1	Y conc in β (plag) (ppm)	N/A		
Bulk Sr conc (ppm)	80	Bulk Sr conc (ppm)	120	Bulk Sr conc (ppm)	92		
Sr conc in Melt (ppm)	150.1	Sr conc in Melt (ppm)	102.9	Sr conc in Melt (ppm)	110.5		

Sr conc in α (cpx) (ppm)	4.5	Sr conc in α (cpx) (ppm)	N/A	Sr conc in α (cpx) (ppm)	3.3
Sr conc in β (plag) (ppm)	N/A	Sr conc in β (plag) (ppm)	380.6	Sr conc in β (plag) (ppm)	N/A
Bulk V conc (ppm)	180	Bulk V conc (ppm)	250	Bulk V conc (ppm)	201
V conc in Melt (ppm)	61.5	V conc in Melt (ppm)	266.3	V conc in Melt (ppm)	118.8
V conc in α (cpx) (ppm)	307.7	V conc in α (cpx) (ppm)	N/A	V conc in α (cpx) (ppm)	594.1
V conc in β (plag) (ppm)	N/A	V conc in β (plag) (ppm)	2.7	V conc in β (plag)	N/A

*mass fraction component B ($CaAl_2Si_2O_8$)

Table 8a: MCS calculation of R-hybridization

Phases (modal %)	**M** (f_o = 0.53)		**R**	**H_1**	
	melt (55.7), cpx (16.9), plag (10.3), ol (7.5), spl (9.5)		melt + trace ol	melt (87.2), cpx (1.9), ol (6.0), spl (5.0)	
T (°C)	1180		1179.2	1152.5	
Compositions (wt %):	$bulk^M$	$melt^M$	$melt^R$	$bulk^H$	$melt^H$
SiO_2	45.3	51.2	52.0	48.4	51.6
TiO_2	0.9	1.3	0.6	0.8	0.8
Al_2O_3	16.4	16.7	16.5	16.5	17.1
Fe_2O_3	1.3	0.5	1.3	1.3	0.7
Cr_2O_3	2.8	0.05	0	1.5	0.07
FeO	6.6	6.7	6.8	6.7	6.0
MgO	11.9	7.2	7.7	9.97	7.0
CaO	11.6	11.5	9.8	10.7	11.8
Na_2O	2.5	3.9	2.3	2.4	2.7
K_2O	0.1	0.2	0.4	0.3	0.3
P_2O_5	0.1	0.2	0	0.05	0.06
H_2O	0.3	0.6	2.6	1.4	1.6

Table 8b: MCS calculation of R-hybridization

Phases (modal %)	**M** (f_o = 0.65)		**R**	**H_2**	
	melt (55.7), cpx (16.9), plag (10.3), ol (7.5), spl (9.5)		melt + trace ol	melt (80.8), cpx (7.1), ol (5.5), spl (6.5)	
T (°C)	1180		1179.2	1155.9	
Compositions (wt %):	$bulk^M$	$melt^M$	$melt^R$	$bulk^H$	$melt^H$
SiO_2	45.3	51.2	52.0	47.6	51.6
TiO_2	0.9	1.3	0.6	0.8	0.9
Al_2O_3	16.4	16.7	16.5	16.4	17.4
Fe_2O_3	1.3	0.5	1.3	1.3	0.6
Cr_2O_3	2.8	0.05	0	1.8	0.06
FeO	6.6	6.7	6.8	6.7	6.0
MgO	11.9	7.2	7.7	10.5	7.0
CaO	11.6	11.5	9.8	10.96	11.7
Na_2O	2.5	3.9	2.3	2.4	2.9
K_2O	0.1	0.2	0.4	0.24	0.3
P_2O_5	0.1	0.2	0	0.06	0.07
H_2O	0.3	0.6	2.6	1.1	1.4

Table 9 – Initial Conditions for RFCAE Modeling

Initial M Composition

Initial Temperature (K)	1635
Initial Melt Composition	0.605
Isotropic Ratio of Sr in bulk Hybrid Magma H	0.70273
Concentration of Sr in liquid (ppm)	90
Concentration of Rb in liquid (ppm)	0.6
Concentration of V in liquid (ppm)	250
Concentration of Yb in liquid (ppm)	5

	K_α	K_β
Sr	0.05	2
Rb	0.03	0.07
V	2	0.001
Yb	0.7	0.7

R Composition

Initial Temperature (K)	1638
Initial Melt Composition	0.1
Isotropic Ratio of Sr in bulk Hybrid Magma H	0.70289
Concentration of Sr in liquid (ppm)	25
Concentration of Rb in liquid (ppm)	0.8
Concentration of V in liquid (ppm)	100
Concentration of Yb in liquid (ppm)	1

A Composition

Initial Temperature (K)	1500
Initial Melt Composition	0.6
Isotropic Ratio of Sr in bulk Hybrid Magma H	0.705
Concentration of Sr in liquid (ppm)	150
Concentration of Rb in liquid (ppm)	0.58
Concentration of V in liquid (ppm)	300
Concentration of Yb in liquid (ppm)	8

Table 10 – System Parameters for RFCAE Chamber Types

	Waxing	Waning	Steady State
m_o^M	1 m_o^M	1 m_o^M	1 m_o^M
γ_E	0.05	0.1	0.05
m^R (kg)	$0.25m_o^M$	$0.05m_o^M$	$0.11m_o^M$
m^A (kg)	$0.02m_o^M$	$0.02m_o^M$	$0.02m_o^M$
Φ	0.98	0.98	0.98

10. APPENDIX I – Enthalpy Expressions and Details

The specific (per unit mass) enthalpy h of the **H** magma is given by:

$$h^H = \Phi(h^M + h^R) \qquad \text{(A1)}$$

The weighted enthalpy contribution of **M** and **R** to the mixture is given in Table A1-4. The parameter Φ defines the type of hybridization. If $\Phi = 1$, the mixing is isenthalpic (adiabatic), also called R-hybridization. If $0 < \Phi < 1$, the mixing is diabatic and termed RFC-hybridization. There are five possible phase state assemblage outcomes when **M** and **R** hybridize. The final hybrid magma can consist of entirely liquid (L), α crystals + liquid (α + L), β crystals + liquid (β + L), eutectic liquid + α crystals + β crystals (L_e + α + β), or crystals of α and β (α + β). The phase identities, liquid composition and temperature are found by comparing the specific enthalpy of **H** magma computed from Eq. (A1) to enthalpy limits defined *a priori* for the five possible outcomes. These phase assemblage limits in h-T space are depicted schematically in Figure 3. Once X^H is determined, the h-T diagram for that composition can be determined using the expressions given in Table A1-4. The five possible final state assemblages each occupy distinct regions on the h-T diagram. There are three special enthalpies on this diagram denoted h_{max}, h_{mid} and h_{min}. These values separate phase assemblages. For example, when the specific enthalpy of hybrid magma h^H of bulk composition X^H exceeds h_{max}, then the final hybridized magma must lie in the L field on the phase diagram. Similarly, if $X^H > X_e$ and $h_{mid} < h^H < h_{max}$, then hybrid magma will consist of β + L, or if $X^H < X_e$, and $h_{mid} < h^H < h_{max}$, the **H** magma assemblage is α + L. When the hybrid magma enthalpy lies in the range $h_{min} < h^H < h_{mid}$, then the assemblage is L_e + α + β and the amount of eutectic liquid is determined by enthalpy balance. In this case, the

temperature is identically equal to T_e, the eutectic temperature. Finally, if $h^H < h_{min}$, the assemblage is a mixture of α and β crystals in proportions dictated by the lever rule and the temperature is less than T_e. In summary, in order to find the final state of the hybrid magma, the value of h^H is compared to the ranges given in Table A1-4 to discover which of the five possible assemblage outcomes is relevant.

Once the phase state or outcome is known by comparing h^H to the limits specified in Table A1-4 (see Figure 3 and Table A1-4), the final state of hybrid magma can be determined. The state depends first on comparison of X^H with X_e and second on the value of h^H. The conditions and final state values are given in Table A1-5 when $X^H < X_e$, in Table A1-6 when $X^H > X_e$ and in Table A1-7 valid when $X^H = X_e$ (exactly). Note that in the latter case, the α + L or β + L fields are not possible.

As a summary example, consider the possibilities when $X^H < X_e$. From the phase diagram, the state of **H** magma can be one of four states (L, L+α, L_e+α+β, α+β). If $h^H > h_{max}$, then **H** is a single phase melt of composition equal to the bulk composition and its temperature is given from the expression in the first row of Table A1-5. If instead $h_{mid} < h^H < h_{max}$ then the **H** magma consists of liquid plus α crystals. Simultaneous solution of the two expressions in row three of Table A1-5 gives T^H and the composition of melt in **H** magma ($X^H = X^{H\ell}$) in the L+α field, thereby defining the appropriate tie line. If $h_{min} < h^H < h_{mid}$, the state is defined by the invariant point assemblage of L_e+α+β. In this case, $T^H = T_e$ and $X^{H\ell} = X_e$. The mass fractions of L_e, α and β crystals are given in row 4 of Table A1-5. Finally, when $h^H < h_{min}$, the assemblage is wholly crystalline (α+β crystals) in proportions given in

the fifth row of Table A1-5. Table A1-6 gives analogous solutions when $X^H > X_e$ and Table A1-7 is appropriate when $X^H = X_e$ exactly.

Table A1-8 summarizes thermodynamic parameter values that approximately model the system $CaMgSi_2O_6$ - $CaAl_2Si_2O_8$ at 10^5 Pa (1-bar).

Table A1-1: Nomenclature and Variable Definitions

Symbol	Definition (units)
X	Mass fraction component B
Y	Mass fraction component A
X_e	Eutectic composition
T_e	Eutectic temperature (K)
$T^{\alpha}_{m.p.}$	Melting point of phase α (K)
$T^{\beta}_{m.p.}$	Melting point of phase β (K)
Δh^{α}	Specific fusion enthalpy of phase α (kJ/kg)
Δh^{β}	Specific fusion enthalpy of phase β (kJ/kg)
C_s	Isobaric specific heat of solid (J/kg·K)
C_L	Isobaric specific heat of liquid (J/kg·K)
ΔC	C_L-C_S (J/kg·K)
X_o^M	Initial mass fraction of component B in **M** magma
$X_o^{M\ell}$	Initial mass fraction of component B in **M** magma melt
X_o^R	Initial mass fraction of component B in **R** magma

$X_o^{R\ell}$	Initial mass fraction of component B in **R** magma melt
T_o^M	Initial T of **M** magma (K)
T_o^R	Initial T of **R** magma (K)
T_ℓ^R	Liquidus T of **R** magma of bulk composition X_o^R (K)
T_ℓ^M	Liquidus T of **M** magma of bulk composition X_o^M (K)
X^H	Mass fraction of component B in **H** magma
$X^{H\ell}$	Mass fraction of component B in **H** magma melt
T^H	T of **H** magma (K)
f_o	Mass fraction of **M** magma in **M**+**R** system
$h_{L\alpha}^M$	Specific enthalpy **M** magma contributes to hybrid magma if **M** magma is single phase liquid of bulk composition $X_o^M < X_e$ (J/kg)
$h_{L\beta}^M$	Specific enthalpy **M** magma contributes to hybrid magma if **M** magma is single phase liquid of bulk composition $X_o^M > X_e$(J/kg)
$h_{\alpha+L}^M$	Specific enthalpy **M** magma contributes to hybrid magma when **M** magma is L + α mixture of bulk composition $X_o^M < X_e$(J/kg)
$h_{\beta+L}^M$	Specific enthalpy **M** magma contributes to hybrid magma when **M** magma is L + β mixture of bulk composition $X_o^M < X_e$(J/kg)
$h_{\alpha+\beta}^M$	Specific enthalpy **M** magma contributes to hybrid magma when **M** magma is α + β crystal mixture (J/kg)
$h_{L\alpha}^R$	Specific enthalpy **R** magma contributes to hybrid magma when **R** magma is single phase liquid of bulk composition $X_o^R < X_e$(J/kg)
$h_{L\beta}^R$	Specific enthalpy **R** magma contributes to hybrid magma when **R** magma is single phase liquid of bulk composition $X_o^R > X_e$(J/kg)

$h^{R}_{\alpha+L}$	Specific enthalpy **R** magma contributes to hybrid magma when **R** magma is L+α mixture of bulk composition $X^{M}_{o} < X_{e}$ (J/kg)
$h^{R}_{\beta+L}$	Specific enthalpy **R** magma contributes to hybrid magma when **R** magma is L+β mixture of bulk composition $X^{M}_{o} > X_{e}$ (J/kg)
$h^{R}_{\alpha+\beta}$	Specific enthalpy **R** magma contributes to hybrid magma when **R** magma is α+β crystal mixture (J/kg)
h_{max}	Specific enthalpy value at boundary between L and α + L or β + L field (J/kg)
h_{mid}	Specific enthalpy value at boundary between α + L or β + L and L_e + α + β (J/kg)
h_{min}	Specific enthalpy value at boundary between L_e + α + β and α + β field (J/kg)
h_{GMAX}	Maximum possible initial specific enthalpy for **M**+**R** in Monte Carlo realizations (J/kg)
h_{GMIN}	Minimum possible initial specific enthalpy for **M**+**R** in Monte Carlo realizations (J/kg)
Φ	Ratio of initial **M**+**R** specific enthalpy (suitably weighted) to the specific enthalpy of the hybrid magma **H:** $h^{H} = \Phi(h^{M} + h^{R})$
$K_i^{\alpha\ell}$	Nernst partition coefficient of trace element *i* in phase α
$K_i^{\beta\ell}$	Nernst partition coefficient of trace element *i* in phase β
w^{M}_{α}	Mass fraction α phase in **M** magma
w^{R}_{α}	Mass fraction α phase in **R** magma
w^{H}_{α}	Mass fraction α phase in **H** magma
w^{M}_{β}	Mass fraction β phase in **M** magma
w^{R}_{β}	Mass fraction β phase in **R** magma
w^{H}_{β}	Mass fraction β phase in **H** magma

w_{ℓ}^{H}	Mass fraction melt in **H** magma
$C_i^{M\ell}$	Concentration of a trace element i in melt phase of **M** magma
$C_i^{R\ell}$	Concentration of a trace element i in melt phase of **R** magma
$C_i^{H\ell}$	Concentration of a trace element i in melt phase of **H** magma
$C_i^{M\alpha}$	Concentration of a trace element i in α phase of **M** magma
$C_i^{R\alpha}$	Concentration of a trace element i in α phase of **R** magma
$C_i^{H\alpha}$	Concentration of a trace element i in α phase of **H** magma
$C_i^{M\beta}$	Concentration of a trace element i in β phase of **M** magma
$C_i^{R\beta}$	Concentration of a trace element i in β phase of **R** magma
$C_i^{H\beta}$	Concentration of a trace element i in β phase of **H** magma
$r_{i_o}^{M}$	Isotopic ratio of element i in bulk composition of **M** magma
$r_{i_o}^{R}$	Isotopic ratio of element i in bulk composition of **R** magma
$r_{i_o}^{H}$	Isotopic ratio of element i in bulk composition of **H** magma
m_o^M	Initial mass of **M** magma
m^R	Mass of **R** magma
m^A	Mass of wallrock assimilated
m^*	Mass of melt remaining after R, FC, A hybridization processes have completed
m^E	Mass of material erupted (removed from system)
γ_E	Mass fraction of erupted material in an RFCAE system

$\overline{T}$	Dimensionless measure of temperature relative to initial temperature
$\overline{X}$	Dimensionless measure of composition relative to initial composition
F	Mass fraction of partial melt extracted from a solid source

Table A1-2: Initial Condition Values for Monte Carlo Simulations

Variable	Mean value	1σ	Absolute minimum value	Absolute maximum value
X_o^M	0.5	0.3	> 0	< 1
X_o^R	0.5	0.3	> 0	< 1
T_o^R	If $X_o^R < X_e$, mean value is average of $T_{m.p}^{\alpha}$ and 0.98 T_e	150	0.98 T_e	$T_{m.p}^{\alpha}$
T_o^R	If $X_o^R > X_e$, mean is average of $T_{m.p}^{\beta}$ and 0.98 T_e	150	0.98 T_e	$T_{m.p}^{\beta}$
T_o^M	If $X_o^M < Xe$, then mean is average of $T_{m.p}^{\alpha}$and 0.98 T_e	150	0.98 T_e	$T_{m.p}^{\alpha}$
T_o^M	If $X_o^M > Xe$, mean is average of $T_{m.p}^{\beta}$ and 0.98 T_e	150	0.98 T_e	$T_{m.p}^{\beta}$
f_o	0.5	0.3	> 0	< 1

Table A1-3: Enthalpy contribution expressions for M and R magmas

$h^{M}_{L\alpha}$	$f_o\left[C_s T_o^M + \Delta h^{\alpha} + X_o^M\left(\Delta h^{\beta} - \Delta h^{\alpha}\right) + \Delta C\left(X_o^M\left(T^{\alpha}_{m.p.} - T^{\beta}_{m.p.}\right) + \left(T_o^M - T^{\alpha}_{m.p.}\right)\right)\right]$
$h^{M}_{L\beta}$	$f_o\left[C_s T_o^M + \Delta h^{\beta} + Y_o^M\left(\Delta h^{\alpha} - \Delta h^{\beta}\right) + \Delta C\left(Y_o^M\left(T^{\beta}_{m.p.} - T^{\alpha}_{m.p.}\right) + \left(T_o^M - T^{\beta}_{m.p.}\right)\right)\right]$
$h^{M}_{\alpha+L}$	$f_o\left[C_s T_o^M + \left(\frac{X_o^M}{X_o^{M\ell}}\right)\Delta h^{\alpha} + X_o^M\left(\Delta h^{\beta} - \Delta h^{\alpha}\right) + \Delta C\left(X_o^M\left(T^{\alpha}_{m.p.} - T^{\beta}_{m.p.}\right) + \left(\frac{X_o^M}{X_o^{M\ell}}\right)\left(T_o^M - T^{\alpha}_{m.p.}\right)\right)\right]$
$h^{M}_{\beta+L}$	$f_o\left[C_s T_o^M + \left(\frac{Y_o^M}{Y_o^{M\ell}}\right)\Delta h^{\beta} + Y_o^M\left(\Delta h^{\alpha} - \Delta h^{\beta}\right) + \Delta C\left(Y_o^M\left(T^{\beta}_{m.p.} - T^{\alpha}_{m.p.}\right) + \left(\frac{Y_o^M}{Y_o^{M\ell}}\right)\left(T_o^M - T^{\beta}_{m.p.}\right)\right)\right]$
$h^{M}_{\alpha+\beta}$	$f_o\left[C_s T_o^M\right]$
$h^{R}_{L\alpha}$	$(1 - f_o)\left[C_s T_o^R + \Delta h^{\alpha} + X_o^R\left(\Delta h^{\beta} - \Delta h^{\alpha}\right) + \Delta C\left(X_o^R\left(T^{\alpha}_{m.p.} - T^{\beta}_{m.p.}\right) + \left(T_o^R - T^{\alpha}_{m.p.}\right)\right)\right]$
$h^{R}_{L\beta}$	$(1 - f_o)\left[C_s T_o^R + \Delta h^{\beta} + Y_o^R\left(\Delta h^{\alpha} - \Delta h^{\beta}\right) + \Delta C\left(Y_o^R\left(T^{\beta}_{m.p.} - T^{\alpha}_{m.p.}\right) + \left(T_o^R - T^{\beta}_{m.p.}\right)\right)\right]$
$h^{R}_{\alpha+L}$	$(1\text{-}f_o)\left[C_s T_o^R + \left(\frac{X_o^R}{X_o^{R\ell}}\right)\Delta h^{\alpha} + X_o^R\left(\Delta h^{\beta} - \Delta h^{\alpha}\right) + \Delta C\left(X_o^R\left(T^{\alpha}_{m.p.} - T^{\beta}_{m.p.}\right) + \left(\frac{X_o^R}{X_o^{R\ell}}\right)\left(T_o^R - T^{\alpha}_{m.p.}\right)\right)\right]$
$h^{R}_{\beta+L}$	$(1\text{-}f_o)\left[C_s T_o^R + \left(\frac{Y_o^R}{Y_o^{R\ell}}\right)\Delta h^{\beta} + Y_o^R\left(\Delta h^{\alpha} - \Delta h^{\beta}\right) + \Delta C\left(Y_o^R\left(T^{\beta}_{m.p.} - T^{\alpha}_{m.p.}\right) + \left(\frac{Y_o^R}{Y_o^{R\ell}}\right)\left(T_o^R - T^{\beta}_{m.p.}\right)\right)\right]$
$h^{R}_{\alpha+\beta}$	$(1 - f_o)\left[C_s T_o^R\right]$

Table A1-4: Specific enthalpy boundary values separating phase assemblages

Specific Enthalpy	Fields Separated	Expressions for specific enthalpy for $X^H < X_e$ and $X^H > X_e$
h_{max}	L and α + L	$C_s\left(T_e - T^{\alpha}_{m.p.}\right)\left(\frac{X^H}{X_e}\right) + C_s T^{\alpha}_{m.p.} + \Delta h^{\alpha} + X^H\left(\Delta h^{\beta} - \Delta h^{\alpha}\right) + \Delta C\left(X^H\left(T^{\alpha}_{m.p.} - T^{\beta}_{m.p.}\right) + \left(\frac{X^H}{X_e}\right)\left(T_e - T^{\alpha}_{m.p.}\right)\right)$
	L and β + L	$C_s\left(T_e - T^{\beta}_{m.p.}\right)\left(\frac{Y^H}{Y_e}\right) + C_s T^{\beta}_{m.p.} + \Delta h^{\beta} + Y^H\left(\Delta h^{\alpha} - \Delta h^{\beta}\right) + \Delta C\left(Y^H\left(T^{\beta}_{m.p.} - T^{\alpha}_{m.p.}\right) + \left(\frac{Y^H}{Y_e}\right)\left(T_e - T^{\beta}_{m.p.}\right)\right)$
h_{mid}	α+L and L_e+α+β	$C_s T_e + \left(\frac{X^H}{X_e}\right)\Delta h^{\alpha} + X^H\left(\Delta h^{\beta} - \Delta h^{\alpha}\right) + \Delta C\left(X^H\left(T^{\alpha}_{m.p.} - T^{\beta}_{m.p.}\right) + \left(\frac{X^H}{X_e}\right)\left(T_e - T^{\alpha}_{m.p.}\right)\right)$
	β+L and L_e+α+β	$C_s T_e + \left(\frac{Y^H}{Y_e}\right)\Delta h^{\beta} + Y^H\left(\Delta h^{\alpha} - \Delta h^{\beta}\right) + \Delta C\left(Y^H\left(T^{\beta}_{m.p.} - T^{\alpha}_{m.p.}\right) + \left(\frac{Y^H}{Y_e}\right)\left(T_e - T^{\beta}_{m.p.}\right)\right)$
h_{min}	L_e+α+β and α+β	$C_s T_e$
Specific Enthalpy	**Fields Separated**	**Expressions for specific enthalpy for $X^H = X_e$**
h_{max}	L and α+β	$C_s T_e + \Delta h^{\alpha} + X_e\left(\Delta h^{\beta} - \Delta h^{\alpha}\right) + \Delta C\left(X_e\left(T^{\alpha}_{m.p.} - T^{\beta}_{m.p.}\right) + \left(T_e - T^{\alpha}_{m.p.}\right)\right)$

Table A1-5: Hybrid magma state for $X^H < X_e$

Specific enthalpy range and phase assemblage	Hybrid system state
$h^H > h_{max}$ L	$T^H = \frac{\Phi h_o - \Delta h^\alpha - X^H\left(\Delta h^\beta - \Delta h^\alpha\right) + \Delta C\left(T^\alpha_{m.p.} - X^H\left(T^\alpha_{m.p.} - T^\beta_{m.p.}\right)\right)}{C_s + \Delta C}$ $X^{H\ell} = X^H$
$h_{mid} < h^H < h_{max}$ $L + \alpha$	Simultaneous solution of the following two expressions give $X^{H\ell}$ and T^H: (1) $C_s T^H + \left(\frac{X^H}{X^{H\ell}}\right)\Delta h^\alpha + X^H\left(\Delta h^\beta - \Delta h^\alpha\right) + \Delta C\left(X^H\left(T^\alpha_{m.p.} - T^\beta_{m.p.}\right) + \left(\frac{X^H}{X^{H\ell}}\right)\left(T^H - T^\alpha_{m.p.}\right)\right) - \Phi h_o = 0$ (2) $T^H = \left(T_e - T^\alpha_{m.p.}\right)\left(\frac{X^{H\ell}}{X_e}\right) + T^\alpha_{m.p.}$ Mass fraction α crystals: $w^H_\alpha = 1 - \frac{X^H}{X^{H\ell}}$ Mass fraction melt: $w^H_\ell = \frac{X^H}{X^{H\ell}}$
$h_{min} < h^H < h_{mid}$ $L_e + \alpha + \beta$	$T^H = T_e$ $X^{H\ell} = X_e$ Mass fraction of liquid of eutectic composition: $w^H_\ell = \frac{\Phi h_o - C_s T_e}{\Delta h^\alpha + X_e\left(\Delta h^\beta - \Delta h^\alpha\right) + \Delta C\left(X_e\left(T^\alpha_{m.p.} - T^\beta_{m.p.}\right) + \left(T_e - T^\alpha_{m.p.}\right)\right)}$ Mass fraction β crystals: $w^H_\beta = X^H - w^H_\ell X_e$ Mass fraction α crystals: $w^H_\alpha = 1 - w^H_\beta - w^H_\ell$
$h^H < h_{min}$ $\alpha + \beta$	$T^H = \frac{\Phi h_o}{C_s}$ $w^H_\alpha = \left(1 - X^H\right)$ $w^H_\beta = X^H$

Table A1-6: Hybrid magma state for $X^H > X_e$

Specific enthalpy range and phase assemblage	Hybrid system state
$h^H > h_{max}$ L	$T^H = \frac{\Phi h_o - \Delta h^\beta - Y^H\left(\Delta h^\alpha - \Delta h^\beta\right) + \Delta C\left(T^\beta_{m.p.} - Y^H\left(T^\beta_{m.p.} - T^\alpha_{m.p.}\right)\right)}{C_s + \Delta C}$ $Y^{H\ell} = Y^H$
$h_{mid} < h^H < h_{max}$ L + β	Simultaneous solution of the following two expressions give $X^{H\ell}$ and T^H: (1) $C_s T^H + \left(\frac{Y^H}{Y^{H\ell}}\right)\Delta h^\beta + Y^H\left(\Delta h^\alpha - \Delta h^\beta\right) + \Delta C\left(Y^H\left(T^\beta_{m.p.} - T^\alpha_{m.p.}\right) + \left(\frac{Y^H}{Y^{H\ell}}\right)\left(T^H - T^\beta_{m.p.}\right)\right) - \Phi h_o = 0$ (2) $T^H = \left(T_e - T^\beta_{m.p.}\right)\left(\frac{Y^{H\ell}}{Y_e}\right) + T^\beta_{m.p.}$ Mass fraction β crystals: $w^H_\beta = 1 - \frac{Y^H}{Y^{H\ell}}$ Mass fraction melt: $w^H_\ell = \frac{Y^H}{Y^{H\ell}}$
$h_{min} < h^H < h_{mid}$ $L_e + \alpha + \beta$	$T^H = T_e$ $Y^{H\ell} = Y_e$ Mass fraction of liquid of eutectic composition: $w^H_\ell = \frac{\Phi h_o - C_s T_e}{\Delta h^\beta + Y_e\left(\Delta h^\alpha - \Delta h^\beta\right) + \Delta C\left(Y_e\left(T^\beta_{m.p.} - T^\alpha_{m.p.}\right) + \left(T_e - T^\beta_{m.p.}\right)\right)}$ Mass fraction α crystals: $w^H_\alpha = Y^H - w^H_\ell Y_e$ Mass fraction β crystals: $w^H_\beta = 1 - w^H_\alpha - w^H_\ell$
$h^H < h_{min}$ α + β	$T^H = \frac{\Phi h_o}{C_s}$ $w^H_\alpha = Y^H$ $w^H_\beta = \left(1 - Y^H\right)$

Table A1-7: Hybrid magma state for $X^H = X_e$

Specific enthalpy range and phase assemblage	Hybrid system state
$h^H > h_{max}$ L	$T^H = \frac{\Phi h_o - \Delta h^\alpha - X_e\left(\Delta h^\beta - \Delta h^\alpha\right) + \Delta C\left(T_e - T^\alpha_{m.p.} + X_e\left(T^\alpha_{m.p.} - T^\beta_{m.p.}\right)\right)}{C_s}$ $X^{H\ell} = X_e$
$h_{min} < h^H < h_{mid}$ $L_e + \alpha + \beta$	$T^H = T_e$ $X^{H\ell} = Y_e$ Mass fraction of liquid of eutectic composition: $w^H_\ell = \frac{\Phi h_o - C_s T_e}{\Delta h^\alpha + X_e\left(\Delta h^\beta - \Delta h^\alpha\right) + \Delta C\left(X_e\left(T^\alpha_{m.p.} - T^\beta_{m.p.}\right) + \left(T_e - T^\alpha_{m.p.}\right)\right)}$ Mass fraction α crystals: $w^H_\alpha = \left(1 - w^H_\ell\right)(1 - X_e)$ Mass fraction β crystals: $w^H_\beta = \left(1 - w^H_\ell\right)X_e$
$h^H < h_{min}$ $\alpha + \beta$	$T^H = \frac{\Phi h_o}{C_s}$ $w^H_\alpha = 1 - X_e$ $w^H_\beta = X_e$

Table A1-8: Thermodynamic parameters of toy model. Parameters closely follow those in system $CaMgSi_2O_6$-$CaAl_2Si_2O_8$ at 10^5 Pa.

Thermodynamic parameter	Symbol	Value	Units
Eutectic composition, mass fraction component B	X_e	0.42	
Eutectic temperature	T_e	1547	K
Melting point of α crystals	$T^{\alpha}_{m.p.}$	1665	K
Enthalpy of fusion of α crystals at $T^{\alpha}_{m.p.}$	Δh^{α}	636	kJ/kg
Melting point of β crystals	$T^{\beta}_{m.p.}$	1830	K
Enthalpy of fusion of β crystals at $T^{\beta}_{m.p.}$	Δh^{β}	478	kJ/kg
Crystal specific isobaric heat capacity	C_S	1400	J/kg K
Liquid specific isobaric heat capacity	C_L	1600	J/kg K

11. APPENDIX II - Trace Element Expressions and Partition Coefficients

Table A2-1: Concentration of trace element in **M**, **R** and **H** melt and coexisting crystalline phases α and β

Phase Assemblage	**M magma**	**R magma**	**H magma**
L	$C_\ell^M = C_o^M$	$C_\ell^R = C_o^R$	$C_\ell^H = C_o^H$
L + α	$C_\ell^M = \frac{C_o^M}{\left(w_\alpha^M\left(K^{\alpha\ell}-1\right)+1\right)}$	$C_\ell^R = \frac{C_o^R}{\left(w_\alpha^R\left(K^{\alpha\ell}-1\right)+1\right)}$	$C_\ell^H = \frac{C_o^H}{\left(w_\alpha^H\left(K^{\alpha\ell}-1\right)+1\right)}$
	$C_\alpha^M = C_\ell^M K^{\alpha\ell}$	$C_\alpha^R = C_\ell^R K^{\alpha\ell}$	$C_\alpha^H = C_\ell^H K^{\alpha\ell}$
L + β	$C_\ell^M = \frac{C_o^M}{\left(w_\beta^M\left(K^{\beta\ell}-1\right)+1\right)}$	$C_\ell^R = \frac{C_o^R}{\left(w_\beta^R\left(K^{\beta\ell}-1\right)+1\right)}$	$C_\ell^H = \frac{C_o^H}{\left(w_\beta^H\left(K^{\beta\ell}-1\right)+1\right)}$
	$C_\beta^M = C_\ell^M K^{\beta\ell}$	$C_\beta^R = C_\ell^R K^{\beta\ell}$	$C_\beta^H = C_\ell^H K^{\beta\ell}$
α + β	$C_\alpha^M = \frac{K^{\alpha\ell} C_o^M}{\left(K^{\beta\ell} + w_\alpha^M\left(K^{\alpha\ell}-K^{\beta\ell}\right)\right)}$	$C_\alpha^R = \frac{K^{\alpha\ell} C_o^R}{\left(K^{\beta\ell} + w_\alpha^R\left(K^{\alpha\ell}-K^{\beta\ell}\right)\right)}$	$C_\alpha^H = \frac{K^{\alpha\ell} C_o^H}{\left(K^{\beta\ell} + w_\alpha^H\left(K^{\alpha\ell}-K^{\beta\ell}\right)\right)}$
	$C_\beta^M = \left(\frac{K^{\beta\ell}}{K^{\alpha\ell}}\right) C_\alpha^M$	$C_\beta^R = \left(\frac{K^{\beta\ell}}{K^{\alpha\ell}}\right) C_\alpha^R$	$C_\beta^H = \left(\frac{K^{\beta\ell}}{K^{\alpha\ell}}\right) C_\alpha^H$
L_e + α + β	N/A	N/A	$C_\ell^H = \frac{C_o^H}{w_\ell^H\left(1+\left(K^{\alpha\ell}-K^{\beta\ell}\right)\right)+\left(1-w_\ell^H\right)K^{\beta\ell}}$
			$C_\alpha^H = C_\ell^H K^{\alpha\ell}$
			$C_\beta^H = C_\ell^H K^{\beta\ell}$

Table A2-2: Typical partition coefficients and bulk concentrations used in toy model computations. For 'basalt' toy system phase α is analogous to diopside and phase β is analogous to anorthite. TE_1-TE_5 are generalized trace element designations. Typical periodic table trace elements with respect to α and β [clinopyroxene (cpx) and plagioclase (plag)] are listed along with representative concentrations in basalts from various petrotectonic environments.

ELEMENT	K_α	K_β	Typical elements with ~K_α for cpx	Typical elements with ~K_β for plag	N-MORB conc. (ppm)	Oceanic flood basalt conc. (ppm)	OIB Mauna Loa shield conc. (ppm)	Island arc tholeiite conc. (ppm)****
TE_1	.01	2	U, Nb,Y	Sr	0.5, 2, 30, 100	0.1, 4, 23, 150	0.2, 8***, 20***, 250	0.3, 0.6, 14, 300
TE_2	.07	1.3	Sr, La, Ce	Sr	100, 3, 8, 100	150, 4, 11, 150	250, 10, 25, 250	300, 3, 7, 300
TE_3	0.7	0.7	Yb, Eu	La, Eu	3, 1, 2, 1	2, 1, 4, 1	2, 2, 10, 2	1, 0.7, 3, 0.7
TE_4	1.3	.07	Ni, V	Rb, Yb, Zr, Ti	150*, 250**, 0.6, 3, 75, 15000	100, 300, 1, 2, 70, 12000	125, 300, 4***, 2, 150, 20000	20, 250, 7, 1.3, 31, 6000
TE_5	2	.01	Cr	U, Y, Nb,	250**, 0.5, 30, 2	130, 0.1, 23, 4	260, 0.2, 20***, 8***	40, 0.3, 14, 0.6

The concentrations are for the elements listed in columns 3 and 4. *from Hoffman (1988), **from Gale et al. (2013), ***from Hoffman and Jochum (1996), **** from Singer et al. (2007). All other concentrations from Best and Christiansen (2001)

12. APPENDIX III – Mixing Hyperbolas

Because the toy model involves the thermodynamics of magma (**M** and **R**) or source (**DM** and **EM**) mixing, hybridization and crystallization or melting, it is useful to portray results in terms of classical mixing diagrams. Here a brief overview of the systematics of binary mixing diagrams is provided. The principles of simple mixing are well known: mixing diagrams have been used for many years to make geochemical interpretations (e.g., Steiger and Wasserburg 1966; Vollmer 1976; Langmuir et al. 1978; Juteau et al. 1986; Albarede 1995; Faure and Mensing 2005). The term simple mixing refers to the mixing of single-phase materials without any physical or chemical effects except mechanical mixing. In natural magmatic systems, the assumptions inherent to simple mixing are often difficult or impossible to verify. However, simple mixing can still be applied provided additional constraints imposed from phase equilibria considerations are imposed. What follows is first a brief synopsis of the mathematics of simple mixing followed by application of simple mixing to multiphase systems. In particular, the most concise way to examine a dataset in order to accept or reject the mixing hypothesis is presented. The thermodynamic meaning of 'component' is preserved in what follows; rather than refer to mixing 'components' we refer to binary mixing of end-members. The emphasis here is on the relationships between end-member bulk composition mixing hyperbolas depicted using either isotope ratio-ratio's or trace elements ratio-ratio's (for trace element pairs with identical or close to identical bulk phase partition coefficients) and mixing hyperbolas defined in terms of the phases present in pre mixing end-members or in hybridized magma or melt derived by partial melting of a mixed binary end-member source. Coexisting phase hyperbolas in hybrid magmas or melts resulting from partial melting of mixed end-member sources involve thermodynamic

constraints (energy and mass balance) based upon phase proportions and solid/liquid partition coefficients. End-member bulk compositions can be heterogeneous (phase mixtures of α+L, β+L, $\alpha+\beta+L_e$ or $\alpha+\beta$ in the toy model) or homogeneous (L only). When magma mixing is the process studied the end-members are labeled **M** for resident magma and **R** for recharge magma. When wholly crystalline sources are mixed and partially melted, the mixing end-members are labeled **DM** and **EM** for depleted mantle and enriched mantle. All results and depictions are presented in terms of the nomenclature of the toy model (see Table A1-1 for variable definitions). The particular emphasis is on ratio-ratio plots because these represent the most efficient means to establish or reject mixing as the petrogenetic process relating a suite of compositions and because ratio–ratio plots enable construction of coexisting phase hyperbolas that are related to classical end-member mixing hyperbolas via phase equilibria constrains.

Simple Mixing: Nomenclature

The simple case of mixing of two *homogeneous* end-members (e.g., two melts mixing to form a third homogeneous or hybrid melt) in which each end-member consists of i thermodynamic components (i = 1, 2, 3, ⋯, n) where n is the number of independent species needed to describe the composition of each end-member is well known. The chemical component can be a major element, generally taken as an oxide (e.g., FeO, MgO, SiO_2), a trace element (e.g., Ta, Li, La) or an isotope of a trace or major element (e.g., ^{87}Sr, ^{57}Fe). It is ergonomic and informative to form ratios, which can involve oxides (e.g., C_{SiO2}/C_{Al2O3} vs. C_{FeO}/C_{MgO}), trace elements (e.g., C_{Sr}/C_{Eu} vs C_Y/C_V) or isotopes (e.g., $^{87}Sr/^{86}Sr$ vs $^{143}Nd/^{144}Nd$). C represents the mass fraction of the subscripted component. For isotopes, we

use the traditional nomenclature to depict composition. For example, $^{87}Sr/^{86}Sr$ is the mass fraction ratio of ^{87}Sr to ^{86}Sr. In simple mixing, crystallization of phases from a melt or generation of partial or total melt from a mixed solid source are not considered. The simple mixing process produces mechanical mixtures of the two homogeneous end-member bulk compositions and avoids the complications of phase equilibria. Simple mixing is a convenient starting point because it is easily quantitatively handled and because, when the assumptions upon which it are based are not violated, can produce valuable insight into end-member (bulk) compositions. In what follows, compositions are defined in terms of the mass fraction of component i (indexed by a number or element such as C_1 or C_{Sr}) in the j^{th} mixing end-member (C_i^j). When an end-member or hybrid magma is heterogeneous, then phase identities are denoted by annotation following the reservoir identity. The same notation is used to differentiate between coexisting phases. For example, if recharge **R** magma is a mixture of β crystals and melt, the concentration of Sr in each would be denoted $C_{Sr}^{R\beta}$ and $C_{Sr}^{R\ell}$, respectively. If such a mixed source is partially melted, then the concentration (mass fraction) of Sr in the equilibrium melt is denoted $C_{Sr}^{H\ell}$ and if two solid phases coexisted with that liquid, they would be denoted $C_{Sr}^{H\alpha}$ and $C_{Sr}^{H\beta}$, respectively. All variable definitions used are given in Table A1-1.

Mixing Systematics: Bulk Composition Hyperbolas in ratio-concentration coordinates

For specificity we treat magma mixing rather than source mixing in this Appendix; simple substitution of reservoir identification (**DM** and **EM** for **M** and **R,** respectively) gives the source mixing case explicitly.

In this section, the ratio-concentration relationship for mixing of two end-member bulk compositions (**M** and **R** or **DM** and **EM**) is derived. First, note that for i = 1, 2, 3,⋯, n chemical components, a set of n expressions are derived using elementary mass conservation. The mass balance expressions are

$$C_i^H = C_i^M f + C_i^R(1-f),\ \ i = 1, 2, 3, \cdots, n \qquad \text{(A3-1)}$$

where f is the mass fraction contribution from end-member **M** mixed with fraction (1-f) from end-member **R** to form hybrid magma **H**. Now, for i = 1 to n Eq (A3-1) can be solved for the mass fraction f of **M** in the mixture, or hybrid composition (**H**). There are n expressions according to

$$f = \frac{C_1^H - C_1^R}{C_1^M - C_1^R} = \frac{C_2^H - C_2^R}{C_2^M - C_2^R} = \cdots = \frac{C_n^H - C_n^R}{C_n^M - C_n^R} \qquad \text{(A3-2)}$$

In the following, a particularly convenient relationship between the ratio of any two components and the concentration of one of these components is derived. This expression becomes the basis upon which mixing hyperbolas are defined. In particular, the ratio C_2^H/C_1^H can be written as a function of C_1^H and the concentration of components 1 and 2 in the mixing end-members **M** and **R**. Explicitly the identity

$$\frac{C_2^H}{C_1^H} = \frac{\left(C_2^M f + C_2^R(1-f)\right)}{C_1^H} \qquad \text{(A3-3)}$$

can be written

$$C_2^H/C_1^H = \left(C_2^M/C_1^M\right)\left(C_1^M/C_1^H\right)f + \left(C_2^R/C_1^R\right)\left(C_1^R/C_1^H\right)(1-f) \qquad \text{(A3-4)}$$

Upon further rearrangement grouping the terms involving the fraction f of **M** end-member, one arrives at the form

$$C_2^H/C_1^H = (C_2^R/C_1^R) + \left[\left(\frac{C_2^M}{C_1^M}\right) - \left(\frac{C_2^R}{C_1^R}\right)\right](C_1^M/C_1^H)f \qquad \text{(A3-5)}$$

In (A3-5) the term $\left(C_1^M/C_1^H\right)f$ is replaced using the first identity on the right hand side of Eq (A3-2);

$$(C_1^M/C_1^H)f = [C_1^M/(C_1^M - C_1^R)][1 - (C_1^R/C_1^H)] \qquad \text{(A3-6)}$$

Combination of Eqs (A3-5) and (A3-6) gives the form

$$C_2^H/C_1^H = (C_2^R/C_1^R) + \left[\left(\frac{C_2^M}{C_1^M}\right) - \left(\frac{C_2^R}{C_1^R}\right)\right]\left[\frac{C_1^M}{(C_1^M - C_1^R)}\right]\left(1 - \frac{C_1^R}{C_1^H}\right) \qquad \text{(A3-7)}$$

which is simplified to

$$\frac{C_2^H}{C_1^H} = A + \frac{B}{C_1^H} \qquad \text{(A3-8)}$$

with the constants given defined by:

$$A = (C_2^R/C_1^R) + \left[\left(\frac{C_2^M}{C_1^M}\right) - \left(\frac{C_2^R}{C_1^R}\right)\right]\left[\frac{C_1^M}{(C_1^M - C_1^R)}\right] \qquad \text{(A3-9a)}$$

and

$$B = -\left[\left(\frac{C_2^M}{C_1^M}\right) - \left(\frac{C_2^R}{C_1^R}\right)\right]\left[\frac{C_1^M C_1^R}{(C_1^M - C_1^R)}\right] \qquad \text{(A3-9b)}$$

Note that A and B are fixed once the concentrations of components 1 and 2 in mixing end-members **M** and **R** are given. For each pair of elements (e.g., elements 2 and 1 or 3 and 1, etc) there is a similar development of the general form $C_j^H/C_k^H = A_{jk}+\left(B_{jk}/C_k^H\right)$ between any two (distinct) components. A test of the hypothesis that a set of observed (measured) compositions *of a single phase material* represents mixing of varying proportions (distinct f's) of two end-members (e.g., **M** and **R** or **DM** and **EM**), therefore, is to plot the ratio of each component against a fixed (reference) component (say i = 1) against the reciprocal of the reference component. If each of the resulting n-1 plots are linear then the hypothesis of mixing is verified. For example, if one is testing the mixing hypothesis using data for 5 components (say 5 trace elements), then the necessary and sufficient condition for acceptance of the mixing hypothesis (i.e., samples that are related by mixing of end-member compositions **M** and **R**) is that the plots C_2/C_1 vs C_1^{-1}, C_3/C_1 vs C_1^{-1}, C_4/C_1 vs C_1^{-1}, and C_5/C_1 vs C_1^{-1} are linear. Furthermore, if the composition of one end-member composition was known (say **M**), then the composition of the second end-member (**R**) could be determined uniquely from simultaneous solution of Eqs (A3-9a) and (A3-9b) for each independent component.

Mixing Systematics: Bulk Composition Hyperbolas in ratio-ratio coordinates

As noted above, for n independent components, a test of mixing involves demonstration of the linearity of n-1 plots. In fact a more concise method to detect mixing of end-members in data is to utilize ratio-ratio plots. This theory is outlined below with the goal of providing a concise prescription for the detection of mixing from a dataset.

The starting point is Eq (A3-5) reproduced here for convenience

$$C_2^H/C_1^H = (C_2^R/C_1^R) + \left[\left(\frac{C_2^M}{C_1^M}\right) - \left(\frac{C_2^R}{C_1^R}\right)\right](C_1^M/C_1^H)f \qquad \text{(A3-5)}$$

which is rearranged using Eqs (A3-1) and (A3-2) to give

$$\left(\frac{(C_2^M/C_1^M) - (C_2^R/C_1^R)}{(C_2^H/C_1^H) - (C_2^R/C_1^R)}\right) - 1 = (C_1^R/C_1^M)\frac{(1-f)}{f} \qquad \text{(A3-10)}$$

Further reduction gives the final result

$$\left(\frac{(C_2^M/C_1^M) - (C_2^H/C_1^H)}{(C_2^H/C_1^H) - (C_2^R/C_1^R)}\right) = (C_1^R/C_1^M)\left(\frac{1-f}{f}\right) \qquad \text{(A3-11)}$$

Now, expressions analogous to (A3-11) can be written for every pair of distinct components. For example, for components 3, 4 and 5, 6:

$$\left(\frac{(C_4^M/C_3^M) - (C_4^H/C_3^H)}{(C_4^H/C_3^H) - (C_4^R/C_3^R)}\right) = (C_3^R/C_3^M)\left(\frac{1-f}{f}\right) \qquad \text{(A3-12a)}$$

$$\left(\frac{(C_6^M/C_5^M) - (C_6^H/C_5^H)}{(C_6^H/C_5^H) - (C_6^R/C_5^R)}\right) = (C_5^R/C_5^M)\left(\frac{1-f}{f}\right) \qquad \text{(A3-12b)}$$

For a system of n chemical components there are n/2 ratio pair expressions of the form expressed in Eq (A3-7) if n is even and (n/2 +1) if n is odd. In order to form a mixing hyperbola based on components 1, 2, 3 and 4, Eq (A3-12a) is divided by (A3-11) to give

$$\frac{(C_4^M/C_3^M) - (C_4^H/C_3^H)}{(C_4^H/C_3^H) - (C_4^R/C_3^R)} = \left(\frac{C_1^M/C_3^M}{C_1^R/C_3^R}\right)\left[\frac{(C_2^M/C_1^M) - (C_2^H/C_1^H)}{(C_2^H/C_1^H) - (C_2^R/C_1^R)}\right] \qquad \text{(A3-13)}$$

Now for algebraic transparency, let $y^H = C_4^H/C_3^H$, $x^H = C_2^H/C_1^H$, $y^R = C_4^R/C_3^R$, $x^R = C_2^R/C_1^R$, $y^M = C_4^M/C_3^M$, and $x^M = C_2^M/C_1^M$ and write Eq (A3-13) succinctly in the form

$$\frac{y^M - y^H}{y^H - y^R} = \mathcal{R}\frac{x^M - x^H}{x^H - x^R} \qquad \text{(A3-14)}$$

where $\mathcal{R} \equiv \left(\frac{C_1^M/C_3^M}{C_1^R/C_3^R}\right)$ is the ratio of the concentration values that appear in the denominators of the ratios y^M and x^M. Cross multiplication of Eq (A3-14) leads to the hyperbola

$$Ax^H + Bx^Hy^H + Cy^H + D = 0 \qquad \text{(A3-15)}$$

where $A = y^M - \mathcal{R}y^R$, $B = \mathcal{R} - 1$, $C = y^R - \mathcal{R}x^M$ and $D = \mathcal{R}x^My^R - x^Ry^M$. When the ratio $\mathcal{R}$ equals unity, the term involving x^Hy^H vanishes and the ratio-ratio plot is linear with the form

$$y^H = (-1/C)(D + Ax^H) \qquad \text{(A3-16)}$$

In general however, ratio-ratio plots will possess curvature, the extent of which is governed by the value of $\mathcal{R}$.